

UCSF

UC San Francisco Electronic Theses and Dissertations

Title

Self-organization of cell shape and movement

Permalink

<https://escholarship.org/uc/item/5wf4f3w1>

Author

Pipathsouk, Anne

Publication Date

2019

Peer reviewed|Thesis/dissertation

Self-organization of cell shape and movement

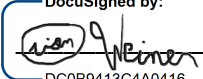
by
Anne Pipathsouk

DISSERTATION
Submitted in partial satisfaction of the requirements for degree of
DOCTOR OF PHILOSOPHY

in
Cell Biology

in the
GRADUATE DIVISION
of the
UNIVERSITY OF CALIFORNIA, SAN FRANCISCO

Approved:

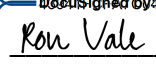
DocuSigned by:

DC0B9413C4A0416... Orion Weiner
Chair

DocuSigned by:

DC0B9413C4A0416... Sophie Dumont

DocuSigned by:

DC0B9413C4A0416... Wallace Marshall

DocuSigned by:

074A1FD9795B43D... Ron Vale

Committee Members

Copyright 2019

by

Anne Pipathsouk

For Ma and Ba,
thank you.

ACKNOWLEDGEMENTS

I am filled with incredible gratitude for having the privilege of learning from many people. They have shaped me into the scientist and person I am today; I am indebted.

I must thank Orion Weiner for being an extraordinary mentor, role model, and friend. His support is unparalleled and unwavering, his optimism and passion for science are boundless, and his creativity is something to truly admire. I thank him for helping me find how science comes alive for me.

I thank the many people in the Weiner lab, past (generation 1-2) and present (generation 3) for all the wonderful memories. I feel very lucky to have shared this experience with them: the postdocs Delquin, Oliver, Jared, Stephanie, Alba, Brian, Jeff, Suvrajit, Kirstin, and Ben; my fellow Tetrad students APTJ, Anna, Julie, Doug, Miriam, and Justin; the iPQB students Zairan, Rachel, Derek, Tamas, Jason, and Jack; and the lab managers Anna, Sana, Natasha, Lena, and Grace for keeping the lab running. In particular, I thank Stephanie, Miriam, Doug, and Jason for their kindness and encouragement that came in various forms. I especially want to thank Sana, Justin, and APTJ for their friendship.

My thesis committee Sophie Dumont, Wallace Marshall, and Ron Vale have inspired and influenced me in countless ways. Throughout the projects, they provided invaluable insights, clarity, and boosts of confidence. Beyond that, they all lead by example. Sophie, for asking the hard questions and finding the time and patience to be my go-to faculty.

Wallace, for being so genuine and sharing his curiosity and excitement with all of us. Ron, for his pragmatism and expanding the boundaries of the scientific field and education.

There are many other UCSF members who kept me afloat including: Zev Gartner, who somehow seemed to bump into me when I needed a cup of coffee; Mark von Zastrow, who was my qualifying exam chair; Keith Yamamoto, who was my MIND group's co-facilitator; and DeLaine Larsen, whose patience and help with all things microscopes made all the difference.

Graduate school would not have been nearly as fun without the incredible friendships that have sustained me. From not understanding genetics (team cell bio!), to providing a couch and too much food, to crying in the Parnassus cafeteria during quals, to volunteering with SEP, to adventuring locally and internationally, and to celebrating all the good and supporting each other through the lows, Han, Alex, and Jess have been my sincerest friends. LEEANNE, Frances, Susan, Dan, Liron, D'Juan, Delsy, Kevin, and Betsy, made the UCSF community the wonderful place that it is.

I would also like to acknowledge the Marine Biological Laboratory's Physiology course at Woods Hole, MA. My rotations with Jennifer Lippincott-Schwartz, Tim Mitchison (Christine Fields, Amy Gladfelter), Rob Phillips and Jane Kondev illuminated what science can mean for someone. The TAs Chris, Jonny, Tanner, James, and Lishi provided the support and encouragement that I did not realize was missing. And of course, my classmates,

especially Parijat, Christoph, Roderick, Fabio, Charlotte, Emily, and Rosalie for making that summer a beautiful one.

There is no doubt that I would have made it this far without everybody and the numerous formative experiences prior to graduate school. I would like to acknowledge the many teachers and mentors at the Illinois Mathematics and Science Academy who encouraged and fostered my curiosity early on, especially Don Dosch, Sue Styer, Max McGee, Ms. Cain, and Guoxing Zheng (UIC). From Stanford, I must thank Martha Cyert, who told me to apply to Tetrad; James Nelson and Russ Altman for being inspiring professors; and, of course, Phil Hanawalt for his mentorship and providing the research opportunity that solidified this trajectory.

I am grateful for many incredible human beings who continue to mean so much to me: Hannah, Stadnyk, Alyssa, Helena, Erin, Carissa, Dersu, Taurean, Martina, Kevin, Jenny, Tiff, Atira, Julian, Jesse, and Sammy. Thank you for keeping me sane and for reminding me of how weird I am.

I would be nowhere without my family. Their unconditional love and support give me the courage to do the best that I can. I thank my brother, Andrew, for undoubtedly paving the way forward for me and being nearby through thick and thin of grad school. I thank my sister, Sophia, for being my number one person as well as the funniest, most whimsical, creative, and fearless person ever. I am forever grateful for my parents, Bounsay and

Pealuan, for absolutely everything, especially for teaching us the value of an education, for fostering our independence, and for simply wanting us to be happy.

And Kamil, who has waited, by my side, near and far. Thank you for riding the waves of graduate school with me. Thank you for reminding me of what is actually important. Thank you for making sure I backed up all my data. It's time to start our lives now!

STATEMENT REGARDING AUTHOR CONTRIBUTIONS

Chapter 2 is a reprint of a *Molecular Biology of the Cell* article:

Julie Wu, Anne Pipathsouk, A. Keizer-Gunnink, F. Fusetti, W. Alkema, Shanshan Liu, Steven Altschuler, Lani Wu, Arjan Kortholt, Orion D Weiner. (2015). Homer3 regulates the establishment of neutrophil polarity. Volume 26 (9): 1629-39.

Julie Wu conceived, designed, and performed the experiments and drafted the manuscript under guidance of Orion Weiner. I performed the revision experiments under the guidance of Julie Wu and Orion Weiner. For the paper, I contributed Figures 1C and 5A. A. Keizer-Gunnink, F. Fusetti, W. Alkema and Arjan Kortholt performed the mass spectrometry and bioinformatics. Shanshan Liu performed the initial analysis for phalloidin staining.

Chapter 3 is a manuscript draft intended for publication:

Anne Pipathsouk, Rachel M. Brunetti, Jason P. Town, Artù Breuer, Patrina A. Pellett, Kyle Marchuk, Ngoc-Han T. Tran, Matthew F. Krummel, Dimitrios Stamou, Orion D. Weiner. WAVE complex self-organization templates lamellipodial formation. bioRxiv <https://doi.org/10.1101/836585>. (Manuscript under review.)

I conceived, designed, and performed the experiments and wrote the manuscript under the guidance of Orion Weiner. Rachel Brunetti assisted with initial super-resolution microscopy experiments, Jason Town performed image analysis and 3D imaging, Artù Breuer assisted with setting up the HUVEC TEMs system, Patrina Pellett assisted with OMX SIM imaging, Kyle Marchuk assisted with lattice light sheet imaging, and Han Tran assisted with electron microscopy experiments.

Chapter 4 is unpublished work using nanotopography to assay molecular curvature sensation. I conceived, designed, and performed the experiments described under the guidance of Orion Weiner. The nano-ridges were designed and fabricated by Jessica Marks, Charlotte Kaplan, Robert Cail, and David Drubin (University of California Berkeley). I provided some input on the design of the nano-Cs and nano-U's that were finalized and fabricated by Yongpeng Zeng and Wenting Zhao (Nanyang Technological University).

ABSTRACT

Self-organization of cell shape and movement

Anne Pipathsouk

This thesis presents work toward understanding the spatial organization of key molecules during cell migration and morphogenesis. Cell migration is essential for many processes including developmental morphogenesis, axon guidance, and immune responses. Chemotaxis, or directed migration guided by chemical cues, requires the spatial and temporal coordination of a multitude of molecules that pattern the force-generating actin cytoskeleton to build plasma membrane protrusions and power cell motility. This work focuses on identifying novel chemotaxis effectors, dissecting their molecular signaling logic, and exploring how key molecules spatially organize to enable the large-scale, self-organization of cell shape and movement.

In the first project, we identified and characterized a novel signaling effector of neutrophil chemotaxis (Chapter 2). From a mass spectrometry pulldown screen, we identified Homer3 as a Gai2 interacting protein. With biochemical and cell biology techniques, we report that Homer3 is necessary for efficient chemotaxis by regulating the polarized spatial organization, rather than the magnitude and kinetics, of key signaling molecules. Overall, our work characterized how Homer3 functions as a scaffold to spatially organize polarity signaling and actin assembly.

In the second project, we studied the spatial organization of the WAVE complex, which is a key effector of cell shape and migration across eukaryotes (Chapter 3). Using quantitative, live-cell super-resolution microscopy, we discovered how the WAVE complex spatially assembles into nanometer scale ring structures at sites of saddle membrane curvature in the absence of actin polymerization. This geometric association for the WAVE complex could explain emergent cell behaviors, such as expanding and self-straightening lamellipodia as well as the ability of endothelial cells to recognize and seal transcellular holes.

In the third project, I describe my pilot work using nanotopography to physically manipulate cell geometry to assay curvature sensation (Chapter 4). The interdisciplinary nature of this experiment, which spans nano-engineering, cell biology, and high-resolution microscopy, highlights a combination of expertise that will undoubtedly unveil exciting insights.

TABLE OF CONTENTS

CHAPTER 1 INTRODUCTION	1
CHAPTER 2 HOMER3 REGULATES THE ESTABLISHMENT OF NEUTROPHIL POLARITY	9
SUMMARY	10
INTRODUCTION	11
RESULTS.....	13
DISCUSSION	19
MATERIALS AND METHODS	23
ACKNOWLEDGEMENTS.....	35
REFERENCES	36
CHAPTER 3 WAVE COMPLEX SELF-ORGANIZATION TEMPLATES LAMELLIPODIAL FORMATION	57
SUMMARY	58
INTRODUCTION	59
RESULTS.....	62
DISCUSSION	71
MATERIALS AND METHODS	76
ACKNOWLEDGEMENTS.....	86
REFERENCES	87

CHAPTER 4 USING NANOTOPOGRAPHY TO ASSAY MOLECULAR

CURVATURE SENSATION	120
SUMMARY	121
INTRODUCTION	122
RESULTS	123
DISCUSSION	126
MATERIALS AND METHODS	128
ACKNOWLEDGEMENTS.....	131
REFERENCES	132

LIST OF FIGURES

CHAPTER 2

FIGURE 2.1.....	44
FIGURE 2.2.....	46
FIGURE 2.3.....	47
FIGURE 2.4.....	49
FIGURE 2.5.....	50
FIGURE S2.1.....	53
FIGURE S2.2.....	54
FIGURE S2.3.....	55
FIGURE S2.4.....	56

CHAPTER 3

FIGURE 3.1.....	97
FIGURE 3.2.....	98
FIGURE 3.3.....	100
FIGURE 3.4.....	102
FIGURE 3.5.....	104
FIGURE 3.6.....	106

FIGURE 3.7.....	109
FIGURE 3.8.....	111
FIGURE S3.1.....	112
FIGURE S3.2.....	113
FIGURE S3.3.....	114
FIGURE S3.4.....	116
FIGURE S3.5.....	118
FIGURE S3.6.....	119

CHAPTER 4

FIGURE 4.1.....	134
FIGURE 4.2.....	135
FIGURE 4.3.....	136
FIGURE 4.4.....	137

CHAPTER ONE

INTRODUCTION

“Are you here to make a discovery or here to understand how the world works?
Hopefully both. Be open to walking through the side door.”

- Tony Hyman

Rac has over 150 GEFs and GAPs.

“Is that a lot?”

- Ron Vale

“Guess which ABBA song is in my head.”

- Tim Mitchison

How do cells know where to go and how do they physically move? Cells do not have a brain or eyes, nor do they have legs or a car, yet cells migrate across a range of physiological processes. During embryonic development, cells move to form our limbs, guts, and heart. During wound healing, neighboring cells move to heal the injury. During metastasis, cancer cells move to invade other tissues. During infection, immune cells move to hunt and kill invading pathogens. While these are select examples of motility that occur in our bodies, cell movement is a broadly conserved property of biological systems spanning single cells to multicellular organisms (1).

One way that cells “know” where to go is by following external chemical cues – toward food and favorable environments and away from repellents. This process of migration guided by chemical gradients is termed chemotaxis (*chemo* – chemical and *taxis* – movement). Directed migration in eukaryotes involves temporal and spatial sensing of extracellular cues, interpreting and polarizing intracellular signaling molecules into a morphological and functional front and back, and coordinating the dynamic actin cytoskeletal rearrangements to power cell motility (2). Though we have identified many of the key molecules involved in this process, it is not clear how their nanoscale interactions spatially organize to orchestrate large-scale shape changes and complex behaviors. In other words, there exists a (partial) “parts” list, but what are the “rules” that the parts follow to ensure a functioning system?

What are the parts for cell shape and movement?

In this work, we study eukaryotic chemotaxis with human neutrophils, which are cells of our innate immune system that potently migrate to hunt and kill invading pathogens. When neutrophils bind a chemoattractant (i.e. a foreign peptide) via a G-protein coupled receptor, the heterotrimeric G-proteins, G α i and G $\beta\gamma$, dissociate and activate downstream signaling effectors including lipids, GTPases, kinases and phosphatases. These molecules function as a signal relay circuit where they polarize, amplify, and adapt to signals that eventually activates the WAVE complex, which patterns the actin polymerization machinery to build membrane protrusions and power migration. Many of the well-studied effectors in this signaling cascade, such as phosphatidylinositol 3,4,5-triphosphate (PIP₃) and Rac, are downstream of G $\beta\gamma$. In contrast, G α i effectors are much less studied. It was unclear whether G α i's role is to release G $\beta\gamma$ or whether G α i activates its own suite of chemotactic effectors. We sought to expand the parts list and identified and characterized Homer3, a novel G α i effector that spatially organizes key signaling molecules, such as PIP₃, Rac, and the WAVE complex (Chapter 2). We report that Homer3 is necessary for efficient chemotaxis by regulating the polarized spatial organization, rather than the magnitude and kinetics, of key signaling molecules.

How do local interactions produce large-scale order?

How do the individual parts self-organize to generate cell shape and movement? For example, actin, an evolutionarily conserved protein and one of the most abundant

proteins on earth, drives cell shape and movement. Similar to stacking and unstacking simple Lego blocks, actin monomers self-assemble into filaments that disassemble. In eukaryotes, there are over 100 proteins that regulate actin in time and space, such as building it into different shapes, preventing its growth, and taking it apart (3,4).

The rate-limiting step for building a new actin filament is the formation of a nucleus, which is accelerated by the Arp2/3 complex, which builds branched actin networks (3). The spatial and temporal dynamics of the Arp2/3 complex activation is controlled by nucleation-promoting factors (NPFs) Wiskott-Aldrich syndrome protein (WASP) and WASP-family verprolin-homologous protein (WAVE) (5,6). WASP and WAVE are nested in similar signaling topologies — both are stimulated by phosphoinositides, Rho GTPases, and curvature-sensitive Bin-amphiphysin-Rvs (BAR) domain proteins, both activate the Arp2/3 complex, both are recycled in an actin-dependent fashion, and both show evidence of oligomerization at the membrane (5,7–14). However, why the WAVE complex builds lamellipodia, the broad sheet-like protrusions that power cell migration, whereas WASP forms spiky finger-like actin networks of filopodia, invadopodia, and endocytosis is unknown.

Given that WASP and its cytoplasmic partners spatially organize as focal, biomolecular condensates expected for finger-like protrusions (15), we wanted to explore whether the WAVE complex organizes as a linear template expected for sheet-like protrusions (16). Using super-resolution microscopy, we found that the WAVE complex forms higher-order linear oligomers that curve into nanometer scale ring structures in the absence of actin polymer at sites of membrane saddle curvature (Chapter 3). To further explore saddle

geometry enrichment, we analyzed the WAVE complex's localization to transendothelial cell macroaperture (TEMs) tunnels, which are transcellular holes that leukocytes and various pathogens generate in endothelial cells to cross tissue barriers (17). To investigate the molecular mechanism of saddle curvature enrichment, we show that the WAVE complex and IRSp53, a membrane curvature-sensitive protein, collaborate to recognize saddle curvature that IRSp53 cannot sense alone.

Overall, our findings highlight how proteins can partner together to sense complex geometries and how the coupling of saddle curvature recognition (cell shape) and patterning actin polymerization (physical forces) could result in a number of emergent behaviors guiding cell morphogenesis and migration.

How do we manipulate cell shape to test how shape feeds back to signaling?

To test whether membrane curvature is an input that guides the WAVE complex, we designed experiments using nanopatterned substrates to deform plasma membrane geometry (Chapter 4). With further optimization, nanotopography will uncover powerful insights in this system.

REFERENCES

1. Stuelten CH, Parent CA, Montell DJ. Cell motility in cancer invasion and metastasis: Insights from simple model organisms. *Nat Rev Cancer* [Internet]. 2018;18(5):296–312. Available from: <http://dx.doi.org/10.1038/nrc.2018.15>
2. Swaney KF, Huang C-H, Devreotes PN. Eukaryotic Chemotaxis: A Network of Signaling Pathways Controls Motility, Directional Sensing, and Polarity. *Annu Rev Biophys*. 2010;39(1):265–89.
3. Pollard TD, Cooper JA. Actin, a central player in cell shape and movement. *Science* (80-). 2009;326(5957):1208–12.
4. Velle KB, Fritz-Laylin LK. Diversity and evolution of actin-dependent phenotypes. *Curr Opin Genet Dev* [Internet]. 2019;58–59:40–8. Available from: <https://doi.org/10.1016/j.gde.2019.07.016>
5. Takenawa T, Suetsugu S. The WASP-WAVE protein network: Connecting the membrane to the cytoskeleton. *Nat Rev Mol Cell Biol*. 2007;8(1):37–48.
6. Machesky LM, Insall RH. Scar1 and the related Wiskott-Aldrich syndrome protein, WASP, regulate the actin cytoskeleton through the Arp2/3 complex. *Curr Biol*. 1998;8(25):1347–56.
7. Rohatgi R, Ma L, Miki H, Lopez M, Kirchhausen T, Takenawa T, et al. N-WASP activates the Arp2/3 complex and links Cdc42 and phosphoinositide signals to actin assembly. *Mol Biol Cell*. 1999;10(S):122A.
8. Oikawa T, Yamaguchi H, Itoh T, Kato M, Ijuin T, Yamazaki D, et al. PtdIns(3,4,5)P₃ binding is necessary for WAVE2-induced formation of lamellipodia. *Nat Cell*

- Biol. 2004;6(5):420–6.
9. Weiner OD, Marganski WA, Wu LF, Altschuler SJ, Kirschner MW. An actin-based wave generator organizes cell motility. *PLoS Biol.* 2007;5(9):2053–63.
 10. Pollard TD, Borisy GG. Cellular Motility Driven by Assembly and Disassembly of Actin Filaments. *Cell.* 2003;112(4):453–65.
 11. Ho H-Y, Ma L, Li JX, Rohatgi R, Lebensohn A, Ma J Le, et al. Toca-1 mediates Cdc42-dependent actin nucleation by activating the N-WASP-WIP complex. *Cell.* 2004;118(2):203–16.
 12. Koronakis V, Hume PJ, Humphreys D, Liu T, Hørning O, Jensen ON, et al. WAVE regulatory complex activation by cooperating GTPases Arf and Rac1. *Proc Natl Acad Sci U S A.* 2011;108(35):14449–54.
 13. Suetsugu S, Kurisu S, Oikawa T, Yamazaki D, Oda A, Takenawa T. Optimization of WAVE2 complex-induced actin polymerization by membrane-bound IRSp53, PIP3, and Rac. *J Cell Biol.* 2006;173(4):571–85.
 14. Abou-Kheir W, Isaac B, Yamaguchi H, Cox D. Membrane targeting of WAVE2 is not sufficient for WAVE2-dependent actin polymerization: A role for IRSp53 in mediating the interaction between Rac and WAVE2. *J Cell Sci.* 2008;121(3):379–90.
 15. Banjade S, Rosen MK. Phase transitions of multivalent proteins can promote clustering of membrane receptors. *Elife.* 2014;3:1–24.
 16. Lillian K Fritz-Laylin, Megan Riel-Mehan, Bi-Chang Chen, Samuel J Lord, Thomas D Goddard, Thomas E Ferrin SMN-D, Henry Higgs, Graham T Johnson, Eric

Betzig RDM. Actin-based protrusions of migrating neutrophils are intrinsically lamellar and facilitate direction changes. *Elife*. 2017;6(e26990).

17. Carman C V., Springer TA. Trans-cellular migration: cell-cell contacts get intimate. *Curr Opin Cell Biol*. 2008;20(5):533–40.

CHAPTER TWO

HOMER3 REGULATES THE ESTABLISHMENT OF NEUTROPHIL POLARITY

“Those spots could be from gamma rays.”
- Orion Weiner

SUMMARY

Most chemoattractants rely on activation of the heterotrimeric G-protein Gai to regulate directional cell migration, but few links from Gai to chemotactic effectors are known. Through affinity chromatography using primary neutrophil lysate, we identify Homer3 as a novel Gai2-binding protein. RNA interference-mediated knockdown of Homer3 in neutrophil-like HL-60 cells impairs chemotaxis and the establishment of polarity of phosphatidylinositol 3,4,5-triphosphate (PIP₃) and the actin cytoskeleton, as well as the persistence of the WAVE2 complex. Most previously characterized proteins that are required for cell polarity are needed for actin assembly or activation of core chemotactic effectors such as the Rac GTPase. In contrast, Homer3-knockdown cells show normal magnitude and kinetics of chemoattractant-induced activation of phosphoinositide 3-kinase and Rac effectors. Chemoattractant-stimulated Homer3-knockdown cells also exhibit a normal initial magnitude of actin polymerization but fail to polarize actin assembly and intracellular PIP₃ and are defective in the initiation of cell polarity and motility. Our data suggest that Homer3 acts as a scaffold that spatially organizes actin assembly to support neutrophil polarity and motility downstream of GPCR activation.

INTRODUCTION

Directed cell migration plays a central role in many physiological and pathological processes from development to homing of immune cells such as neutrophils, to cancer metastasis. Most chemoattractant receptors mediate activation of motility effectors through Gai-family heterotrimeric G-proteins (1,2). Genetic ablation of Gai2 or pharmacological inhibition of Gai signaling blocks chemotaxis toward most agonists for neutrophils (3,4) and other cells (5).

On binding chemoattractant, G-protein-coupled receptors (GPCRs) trigger GDP to be exchanged for GTP on Gai2, thereby inducing Gai to dissociate from G β γ . Both Gai2-GTP and G β γ interact with downstream signaling partners (6). Many potential links from G β γ to downstream chemotactic effectors are known, including phosphatidylinositol 3-kinase (PI3K)- γ (which stimulates production of phosphatidylinositol 3,4,5-triphosphate [PIP₃]; (7)), P-Rex1 and Dock2 (activators of Rac1 and Rac2 GTPases; (8–10)), and phospholipase β (which hydrolyzes phosphatidylinositol 4,5-bisphosphate into diacylglycerol and inositol trisphosphate; (11)).

Chemoattractant stimulation generates several intracellular signaling asymmetries that organize filamentous actin (F-actin) at the leading edge and actomyosin at the trailing edge (12,13). For example, activation of the small GTPase Rac is localized to the leading edge and is necessary and sufficient for actin assembly and migration in neutrophils (14–17) and other cells (18–21). Rac activates the WAVE2 complex, which promotes actin polymerization through the Arp2/3 complex (22–25). The phospholipid PIP₃ also

accumulates at the leading edge (26) and plays a role in neutrophil migration in vivo (17). How these molecules achieve their polarized distribution during chemotaxis is not known.

Whether Gai2 has its own suite of distinct chemotactic effectors or whether it is simply a handle to release G $\beta\gamma$ is only beginning to be understood. Recent studies have begun to identify Gai2-specific effectors in chemotaxis, such as mInsc, which indirectly binds Gai2-GDP at the leading edge to direct neutrophil migration through the recruitment of polarity effectors (27). In addition, Dock180, a Rac activator homologous to Dock2, has also been shown to be a potential Gai2 effector (28).

Here we identify Homer3 as a novel Gai2-interacting protein that regulates actin organization in neutrophils. Homer3, a member of the Homer family of scaffold proteins, has been shown to play a role in actin dynamics after stimulation in neurons and T-cells (29–31), but its role in chemotaxis is unknown. Here we show that Homer3 spatially organizes actin assembly to support efficient polarity and motility in neutrophils.

RESULTS

We previously used affinity chromatography to identify novel Gα effectors in *Dictyostelium* (32) and sought to use a similar approach to identify Gai effectors in neutrophils. Glutathione S-transferase (GST)-tagged Gai2 was purified and incubated with neutrophil lysate harvested from cavitated pig leukocytes. The GST-Gai2 and associated proteins were then isolated and separated by SDS-PAGE. The protein bands were analyzed by mass spectrometry. A total of four independent pull-down screens (two GST-Gai2-GDP, one GST-Gai2-Gpp(NH)p, and one GST-Gai2-GDP-AlF₄) identified several known Gai-interacting proteins, including RASA3, TNFAIP8, Gβγ, RGS3, and RIC8A (Figure 1A; (1,32–35)). We identified new potential targets as well. From this list of Gai2-interacting proteins, we were most interested in proteins that have functional domains predicted to regulate the cytoskeleton or for which genetic evidence exists in other systems implicating them in actin assembly or cell motility. From this prioritized list of Gai2 interactors, we tested each candidate for a role in directed cell migration with a follow-up short hairpin RNA (shRNA)-based chemotaxis screen in neutrophil-like HL-60 cells (Supplemental Figure S1).

Homer3, a novel Gai interactor, was identified in both the Gai2 interaction screen and the follow-up genetic screen. Homer3 is part of a family of scaffolds that binds a variety of proteins relevant to chemotaxis signaling, including actin and Rac1 (30,31,36). Homer proteins have been primarily studied in neurons, where they localize to the synapse and participate in calcium signaling, axon guidance, and dendritic spine morphology (37–40). In our affinity chromatography experiments, Homer3 bound to GDP-loaded GST-Gai2

and GST-Gai2 loaded with GTP analogues GDP-AlF₄ and Gpp(NH)p with relatively similar peptide counts (Supplemental Figure S1 and Supplemental Tables S1–S4). The interaction between Homer3 and Gai2 was confirmed via GST pull-down assays in neutrophil lysate (Figure 1B). The binding between Gai2 and Homer3 is direct, as shown with GST pull-down assays using proteins purified from bacteria, and independent of whether Gai2 is loaded with GDP or Gpp(NH)p (Figure 1C).

Since we were most interested in novel Gai2 interactors relevant to chemotactic signaling, we assayed whether Homer3 was necessary for neutrophil chemotaxis. Using the neutrophil-like differentiated HL-60 cell line, we knocked down the expression of Homer3 with lentiviral shRNAs (Figure 2A and Supplemental Figure S2; (41)). Differentiated HL-60s infected with nonsense (control) or Homer3 shRNA were assessed with a Transwell chemotaxis assay in which cells migrate through a microporous filter toward a source of chemoattractant. When presented with a gradient of the Gai-coupled GPCR ligand formyl-methionyl-leucyl-phenylalanine (fMLP), Homer3-knockdown cells exhibited a sixfold decrease in migration (Figure 2B). The chemotaxis defect was observed in two independent lines, each expressing a different shRNA against Homer3. The magnitude of the defect scaled with the degree of Homer3 knockdown as measured by real-time PCR (Figure 2A). We chose the line with the higher knockdown efficiency (shRNA 1) for all of our subsequent experiments.

Although Transwell assays can uncover a defect in chemotaxis, this device does not allow for direct visualization of cells during their migration. This makes it difficult to determine

whether the chemotaxis defect represents an impairment in speed, directionality, or persistence. To address this question, we used time-lapse microscopy to visualize Homer3-knockdown cells during random cell migration after stimulation with uniform chemoattractant. We used a “chimney assay” (42) in which cells are resuspended into a small volume of liquid sandwiched between two coverslips. In this context, migration is not dependent on cellular adhesion, enabling us to screen for cells whose lack of movement is not a consequence of a failure to adhere to the substrate. A substantial fraction of the Homer3-knockdown cells fail to move in this context (Figure 3A and Supplemental Movies S1–S3). These nonmotile cells either extended short protrusions that were quickly retracted or completely failed to protrude.

Homer3-knockdown cells not only exhibited a significant increase in the proportion of nonmotile cells, but they also exhibited subtle defects in the motile population of cells. The Homer3-knockdown cells showed a significant increase in the length of pauses between migratory events (Figure 3B and Supplemental Movie S4), consistent with a general defect in initiation of migration. However, Homer3-knockdown cells have a normal overall persistence and speed of cell movement (Figure 3, C and D). Therefore Homer3 appears to play a prominent role in initiation of migration but does not seem to affect the maintenance of migration.

Does the motility defect for Homer3-knockdown cells represent a general lack of activation of heterotrimeric G-protein effectors, as observed for the Ric8 protein in *Dictyostelium* (32)? To investigate whether there is a general defect in signaling, we assayed calcium release from Homer3-knockdown cells after stimulation. Calcium

release was assessed by loading cells with the cell-permeable calcium indicator dye fluo-4 AM and measuring fluorescence intensity in individual cells before and after stimulation with fMLP (43). A similar proportion of cells responded in both the control (407 of 451 cells, 90%) and Homer3-knockdown cells (465 of 546 cells, 85%; Supplemental Figure S3A). Since undifferentiated HL-60s do not express the fMLP receptor, this suggests that Homer3 knockdown does not block cell differentiation. To confirm cell differentiation in Homer3-knockdown cells, we used a phycoerythrin (PE)-conjugated antibody for Cd11b, a receptor expressed exclusively on differentiated cells, and measured fluorescence via fluorescence-activated cell sorting (FACS). Nonsense shRNA cells are $97 \pm 2\%$ differentiated after dimethyl sulfoxide (DMSO) addition, and Homer3 shRNA cells are $92 \pm 5\%$ differentiated (average \pm SD of four measurements; Supplemental Figure S3B). Homer3 knockdown did not affect cell growth or viability through 10 consecutive cell passages (Supplemental Figure S3, C and D). Thus Homer3 knockdown does not prevent cell signaling in response to chemoattractant, nor does it affect differentiation or viability.

To determine whether other GPCR effectors are activated normally in Homer3-knockdown cells, we next assayed the downstream heterotrimeric G-protein effectors Rac and PI3K, both of which contribute to regulation of neutrophil chemotaxis (15,17). We used phosphorylation of p21-activated kinase (Pak) as a downstream readout for Rac activation (44,45). We used phosphorylation of Akt to read out signaling through the PI3K cascade (46–48). Homer3 cells have normal stimulation kinetics and general magnitude of Akt and Pak phosphorylation (Figure 4). This is in contrast to the Transwell migration assay, in which the majority of Homer3-knockdown cells failed to migrate (Figure 2B).

Because Homer proteins have been associated with regulation of the actin cytoskeleton via their N-terminal enabled/vasodilator-stimulated phosphoprotein homology 1 (EVH1)-like domain (29,31), we investigated whether Homer3 plays a similar role in neutrophils. Using purified proteins in an actin cosedimentation assay, we showed that Homer3's N-terminus is necessary and sufficient to bind to actin filaments (Figure 5A). This supports a role for Homer3 in regulating actin in cells, which we explored by analyzing how Homer3 knockdown affects actin polymerization. Exposure to fMLP induces transient global F-actin accumulation, which peaks around 1 min and later organizes into a polarized pseudopod at later time points. In control cells, 80% of the stimulated cells have an organized F-actin pseudopod at 7 min, compared with 50% of Homer3 cells (Figure 5, B and C). In contrast to the significant polarity defect, Homer3-knockdown cells show normal kinetics and overall magnitude of actin assembly (Figure 5D). This suggests that although Homer3- knockdown cells retain their ability to polymerize actin in response to stimulus, they lack the ability to organize the actin into a polarized distribution.

To follow the spatial and temporal dynamics of actin nucleation in live cells, we visualized Hem1-yellow fluorescent protein (YFP), an immune cell-specific subunit of the WAVE2 complex (22,49). Hem1-YFP shows strong leading-edge localization in neutrophils and serves as a dynamic marker of actin polymerization in these cells (22,50). Hem1-YFP persistently localized to the leading edge of control and motile Homer3-knockdown cells (Figure 5, E and F, and Supplemental Movie S5). In nonmotile Homer3-knockdown cells, Hem1-YFP exhibited transient flashes that wandered throughout the cell, indicating a

requirement for Homer3 to sustain persistent polarized actin assembly (Figure 5, E and F, and Supplemental Movie S6).

Similarly, Homer3-knockdown cells failed to generate a polarized PIP₃ response to a chemoattractant gradient set up by a micropipette (Figure 5G). We measured the membrane localization of PH-Akt-Citrine, which binds PIP₃, in response to a micropipette containing chemoattractant. Whereas control cells displayed an asymmetric accumulation of PH-Akt-Citrine toward chemoattractant, immotile Homer3 knockdown cells showed no preferential accumulation. As a control, we measured PH-Akt-Citrine depletion from the cytoplasm and recruitment to the membrane in response to uniform chemoattractant. The initial response in control and Homer3-knockdown cells was the same (Figure 5, G and H), consistent with our previous phospho-Akt assays (Figure 4). In immotile Homer3-knockdown cells, PH-Akt-Citrine returns to the cytoplasm more quickly after stimulation. Homer3 knockdown may affect the persistence of PIP₃ on the membrane, in addition to PIP₃ polarization. This suggests that Homer3 knockdown interferes with the spatial organization of key regulators of actin organization. This result is consistent with the actin assembly polarization defect with Homer3 knockdown (Figure 5, E and F) and suggests that Homer3 functions with Gai2 to spatially regulate the downstream cytoskeletal polarization necessary for efficient neutrophil chemotaxis.

DISCUSSION

Most chemoattractants act through Gai heterotrimeric proteins to mediate directional movement, but only a few chemotaxis-relevant effectors of Gai are known. Recent work from other groups has identified two such effectors, mInsc and the Dock180/Elmo1 complex. mInsc indirectly binds Gai2-GDP via LGN/AGS3 and helps maintain directionality in neutrophils. The Dock180/Elmo1 complex, a Rac GEF, associates with Gai2 upon stimulation of breast cancer cells (27,28) and may organize Rac activity downstream of GPCR activation. Our work adds to this suite of effectors with the identification of Homer3 as a Gai2-binding protein that is essential for efficient cell polarity and motility in neutrophils. Homer3 does not act upstream of Gai2, since the magnitude of Gai effectors (calcium influx, Rac activity, PIP₃ production, bulk actin assembly) are unaffected after Homer3 knockdown. This distinguishes Homer3 from Gai2-interacting proteins that control chemotaxis by regulating the magnitude of Gai activity, such as the G α GEF Ric8A (32).

Our work shows that Homer3 is necessary for the organization of polarity but does not significantly affect overall magnitude of chemotactic effector stimulation. Importantly, the effect of Homer3 knockdown is different from that of most chemotaxis mutants, the bulk of which affect the magnitude of activation of core chemotactic effectors (22). Deletion of components at all levels of the cascade—Gai2, G $\beta\gamma$, Rac, and WAVE—affects both the magnitude and spatial localization of signals such as Rac activation and actin polymerization (1,3,22,51,52). Deletion of downstream effectors of G $\beta\gamma$, such as Rac

GEFs P-Rex1 and Dock2, also significantly inhibit the magnitude of Rac activation and cell migration (10,53).

The shRNA phenotypes suggest a role for Homer3 in organizing polarized, persistent actin assembly. A large fraction of Homer3-knockdown cells form either transient protrusions or no protrusions in uniform chemoattractant. In addition, the motile Homer3-knockdown cells pause longer, supporting a role for initiation of protrusions. This behavior is in contrast to that in wild-type cells, which form persistent pseudopodia in uniform chemoattractant. Because chemoattractant-stimulated neutrophils can polarize in suspension but Homer3-knockdown cells exhibit a significant defect in this context, this defect is not due to misregulation of substrate adhesion. If the actin nucleation machinery does not localize in one spot long enough to organize a pseudopod, this could explain the transient or absent protrusions in Homer3-knockdown cells.

How might Homer3 organize cell polarity? Consistent with previous studies (36), we show that Homer3 directly binds F-actin. Furthermore, previous studies showed that Homer3 binds directly to active Rac1-GTP and not inactive Rac1-GDP (36). We also find that Rac2 interacts with Gai2 in our pull-down screen, possibly through association with Homer3. Thus it is possible that Homer3 could integrate signals from actin, Rac-GTP, and Gai2 to enable neutrophils to organize a persistent leading edge.

We find that Homer3 binds Gai2-GTP and Gai2-GDP with similar affinity. However, this in vitro association is likely to be dependent on chemoattractant-induced dissociation of

Gai and G $\beta\gamma$ in vivo. G $\beta\gamma$ sequesters nonsignaling Gai2-GDP within cells, interrupting the interaction of Gai2-GDP with binding partners. Of note, mlncsc, another recently discovered Gai2 effector, does not show a preference for Gai2-GTP (27) but still plays a role in organizing cell polarity and colocalizes with free Gai2 at the leading edge. However, although both mlncsc and Homer3 interact with Gai2 and are required for efficient chemotaxis, our biochemical and genetic data suggest that they act in different pathways. We observe a very different migration phenotype with Homer3 knockdown than what was observed with mlncsc knockout. Whereas Homer3 knockdown produces rounded, immotile cells, mlncsc knockout produces multiple pseudopodia and lack of persistence (27). Moreover, we do not find mlncsc in our mass spectrometry data. Taken together, these data suggest that Homer3 and mlncsc represent separate pathways from Gai2 to the cell migration machinery.

In summary, we found that Homer3 associates with Gai2 and is necessary for the initiation of cell migration. Whereas nonmotile Homer3-knockdown cells can form transient protrusions, they cannot sustain a leading edge and are unable to generate morphological polarity or polarized F-actin accumulation. Similarly, Gai2-knockout macrophages fail to polarize in chemoattractant (3). Homer3 may enhance the initiation of migration by scaffolding signaling proteins such as active Rac and actin that regulate early steps in leading-edge organization. From our study, we find that the overall magnitude of actin accumulation and its upstream regulators (Rac, PI3K) is not dependent on Homer3. However, persistent and polarized PIP₃ accumulation and actin assembly depend on Homer3. Our previous work (54) demonstrated that there may be distinct control of the

intensity versus polarity of the actin cytoskeleton, and our present work on Homer3 provides the first insight into the pathways that specifically control actin polarity. By characterizing Homer3's role in chemotaxis and linking it to Gai2 and actin polymer, this study enhances our understanding of how Gai2 contributes to cell migration and actin organization.

MATERIALS AND METHODS

Cell lines and culture

HL-60 cells were cultured as described previously (43). Briefly, cells were grown at 37°C/5% CO₂, in RPMI 1640 medium containing l-glutamine, 25 mM 4-(2-hydroxyethyl)-1-piperazineethanesulfonic acid (HEPES;10-041-CM; Mediatech, Manassas, VA), and 10% heat-inactivated fetal bovine serum (FBS). Cell differentiation was initiated by adding 1.5% DMSO (endotoxin-free, hybridoma-tested; D2650; Sigma-Aldrich, St. Louis, MO) to cells in growth media. Cells were used at 2–4 d after differentiation. Differentiation was confirmed with PE-conjugated anti-CD11b antibody (BD Biosciences, Franklin Lakes, NJ).

Cell differentiation

Two hundred thousand cells were pelleted and incubated in 7 µl of CD11b/MAC-1 R-PE–conjugated fluorescence antibody (BD PharMingen, San Diego, CA) on ice for 30 min, washed with ice-cold modified Hank's buffered saline solution (mHBSS) with 2% BSA, and resuspended in the same buffer at 10⁶ cells/ml for analysis. mHBSS with 2% BSA was used to establish background signal with unstained cells and undifferentiated cells. Cells with fluorescent signal above background were considered differentiated.

Imaging and analysis

Total internal reflection fluorescence (TIRF) images were acquired on a Nikon Ti Eclipse inverted microscope with a 60× Apo TIRF 1.49 numerical aperture (NA) objective and an electron-multiplying charge-coupled device (EM-CCD) camera (Evolve; Photometrics, Tucson, AZ) controlled by NIS-Elements (Nikon, Melville, NY). Sample drift was minimized using an autofocus system (Perfect Focus; Nikon). Laser lines (514, 561 nm; all 200 mW) were supplied from a Spectral Applied Research LMM5 Laser Merge Module (Richmond Hill, Canada). This laser launch uses acousto-optic tunable filters (AOTFs) to control laser output to a single-mode TIRF fiber for imaging. TIRF imaging was performed with ≤ 50 mW laser power, achieved through AOTF and neutral density–based laser attenuation.

Confocal images were acquired in a custom-built environmental chamber with temperature and CO₂ control (In Vivo Scientific, St. Louis, MO) on a Nikon Ti Eclipse inverted microscope equipped with a Yokogawa CSU-X1 spinning disk confocal, a 60x Apo TIRF 1.49 NA objective, and a Clara interline CCD (Andor, Belfast, Ireland). The 405-nm, 488-nm, and 561-nm laser wavelengths (MLC400B; Agilent, Santa Clara, CA) were used for excitation.

Calcium assays and time-lapse migration assays were imaged using a CCD camera (Cool Snap HQ; Photometrics) and a Nikon TE-2000 inverted microscope with a 20× PlanFluor 0.5 NA objective in an In Vivo Scientific microscope incubator to create a 37°C climate.

NIS-Elements was used for image acquisition, and NIS-Elements, ImageJ (National Institutes of Health), and Excel (Microsoft, Redmond, WA) were used for data analysis.

Graphing and statistical analyses were performed using Prism 6 (GraphPad, San Diego, CA). All *p* values were calculated using *t* test (populations were of equal variance) or, where indicated, *F* test, paired *t* test, or Mann–Whitney test.

Micropipette experiments

Glass capillaries were pulled as described (43). Needles were backfilled with a solution containing 1 μ M fMLP (F3506; Sigma-Aldrich) and 100 nM Alexa 430 succinimidyl ester (A-10169; Invitrogen, Carlsbad, CA) and held by a micromanipulator (MM-89; Narishige, East Meadow, NY). Agonist flow rate from the pipette was controlled as described (43). Cells were labeled with CellMask Orange (Life Technologies, Carlsbad, CA) according to manufacturer's instructions.

Knockdown-line generation

Lentiviral Homer3 and nonsense shRNA control in pLKO.1 were purchased from Sigma-Aldrich. Sequences used in this study were as follows: Homer3 shRNA 1, 5'-CGGCTAAAGAAGATGTTGTCT-3'; Homer3 shRNA 2, 5'-GAACAGCATCTGACACAGTTT-3'; and control shRNA, 5'-GCGCGATAGCGCTAATAATTT-3'. HEK293T cells were grown to 70% confluency in a six-well plate for each lentiviral target and transfected using 0.5 μ g of Homer3 or nonsense shRNA, 50 ng of vesicular stomatitis virus-G, and 0.5 μ g of cytomegalovirus 8.91 with TransIT-293T (Mirus Bio, Madison, WI) according to the manufacturer's instructions. Medium was changed at 18 h after transfection, and viral supernatant was collected at 42 and 66 h posttransfection. A 4-ml amount of combined viral supernatant

was used to infect 10^6 undifferentiated HL-60 cells by spinfection in the presence of 8 $\mu\text{g}/\text{ml}$ polybrene. Stable cell lines were generated with 1 $\mu\text{g}/\text{ml}$ puromycin selection for 2 wk.

Quantitative real-time PCR

Total RNA was extracted from differentiated HL-60 cells using RNEasy (Qiagen, Mississauga, Canada) according to the manufacturer's instructions. Next 1 μg of total RNA was reverse transcribed with the QuantiTect reverse transcription kit (Qiagen). An equal amount of cDNA from each cell line was amplified by real-time PCR (RT-PCR) using SYBR Green QPCR Master Mix (Applied Biosystems, Foster City, CA). Homer3 RT-PCR primers were 5'-CAGGGAGCAGCCAATCTTCA-3' (forward) and 5'-GGGAGTGACAGTGCTGTTGA-3' (reverse). Expression levels were normalized to a housekeeping gene (glyceraldehyde-3-phosphate dehydrogenase [GAPDH]), and the relative expression value between the samples was calculated based on the threshold cycle (*CT*) value using the standard curve method.

Transwell chemotaxis assay

Transwell chemotaxis assays were performed using 24-well Fluoroblok Transwell chambers (pore size, 3.0 μm ; Corning, Tewksbury, MA) as previously described (55). Briefly, cells were stained with the membrane dye DiD (V-22887; Life Technologies), and 300,000 cells in mHBSS with 0.2% BSA were loaded to each top well. Cells were allowed to migrate toward the bottom well containing 10 nM fMLP for 2 h at 37°C. The migrated cells were measured by fluorescence from the bottom of the insert, and the opaque filter

prevented excitation of cells on top of the filter. Analysis was performed with a FlexStation 3 Microplate Reader (Molecular Devices, Sunnyvale, CA). The percentage of migrating neutrophils was calculated by dividing the fluorescence reading from each well by the fluorescence reading of the total input cells.

Preparation of high-speed cytosol from pig leukocytes

Pig leukocyte cytosol was prepared essentially as described previously (22). Pig blood was obtained from Rancho Veal (Petaluma, CA). A 40-l amount of blood was collected into five polypropylene jugs containing a total of 9 l of 1× sterile acid–citrate–dextrose anticoagulant (80 mM sodium citrate, 15 mM NaH₂PO₄, 160 mM glucose, 17 mM citric acid, and 2 mM adenine). Blood was transported to the laboratory at room temperature. At the laboratory, 250 ml of 154 mM NaCl/3% polyvinylpyrrolidone (molecular weight, 360,000) was added per liter of blood plus anticoagulant, mixed thoroughly, poured into 2-l of polypropylene containers, and allowed to settle into two phases for 30–45 min. The upper phase (containing leukocytes and contaminating red blood cells) was decanted and pelleted at 1500 × g for 15 min at room temperature in an IEC swingout bucket rotor. The supernatant was poured off, and the pellets were resuspended in calcium-free mHBSS containing 0.2% BSA. Cells were pelleted at 1500 × g for 15 min. Cells were resuspended in a minimum volume of mHBSS, and then 10× volume of double-distilled H₂O was added for 20 s to lyse contaminating red blood cells. Then 1.1× volume of 10× mHBSS was added to regain an isotonic solution. Cells were pelleted, washed, and then resuspended in freshly prepared 3 mM diisopropylfluorophosphate in mHBSS to inactivate serine proteases, then allowed to sit for 20 min on ice. Cells were pelleted and resuspended in

cavitation buffer (50 mM NaCl, 50 mM Tris, pH 7.5, at 4°C, 5 mM MgCl₂, 5 mM dithiothreitol [DTT], 1× EDTA-free protease inhibitor tablets [Roche, Basel, Switzerland] per 50 ml of solution). Cells were cavitated in a nitrogen Parr bomb (350 psi, 20 min) into a collection vessel containing ethylene glycol tetraacetic acid (EGTA) for a final concentration of 2 mM EGTA. Disrupted cells were spun at 1500 × g for 15 min to remove nuclei and unbroken cells and then 96,000 × g for 60 min to remove membranes. High-speed supernatant was carefully removed without disturbing the pellet.

Affinity-based chromatography

Rat Gai2, bacterially expressed as a GST-fusion protein, was purified with glutathione-Sepharose FF (GE Healthcare, Little Chalfont, UK) as previously described (56). GST-Gai2 was loaded with GDP or the nonhydrolyzable GTP analogue Gpp(NH)p using the alkaline phosphatase protocol (32). Nucleotide loading was assessed with high-performance liquid chromatography (HPLC). For GDP-AIF₄ loading, 50 μM AlCl₃ and 30 mM NaF were added to GST-Gai2 and incubated at 30°C for 30 min. For the mass spectrometry screen, 3–5 mg of GST or GST-Gai2 bound to glutathione-Sepharose FF in pull-down buffer (50 mM NaCl, 50 mM Tris, pH 7.5, at 4°C, 5 mM MgCl₂, 5 mM DTT) was incubated with 50 ml of 3 mg/ml leukocyte lysate overnight with recirculation. The column was washed with three column volumes of pull-down buffer, and bait and bound proteins were eluted with 20 mM glutathione. Peak protein fractions were pooled and concentrated before running an SDS-PAGE gel and cutting bands for mass spectrometry.

For preparation of FLAG–Homer3, HEK293T cells were transfected with this expression construct. At 48 h posttransfection, the culture medium was removed, and the cells were washed once with phosphate-buffered saline and lysed with 0.4% NP-40 in pull-down buffer. The 293T lysate was clarified by centrifugation and combined with leukocyte lysate prepared as described. GST-Gai2 bound to glutathione-Sepharose FF was incubated with FLAG-Homer3 and leukocyte lysate overnight. Proteins were eluted with glutathione and subjected to SDS–PAGE, followed by staining with Coomassie brilliant blue (CBB) or processing for Western blot with 1:1000 anti-FLAG antibody overnight (F1804; Sigma-Aldrich).

For preparation of purified Homer3, bacterially expressed GST-Homer3 was purified and cleaved using thrombin as described previously (31). One milligram of GST-Gai2 or GST was bound to glutathione-Sepharose FF beads and then loaded with GDP or Gpp(NH)p using the alkaline phosphatase protocol (57). Each condition was incubated with 500 μ g of Homer3 overnight in pull-down buffer (with 0.1 mM of either GDP or Gpp(NH)p). Beads were washed in pull-down buffer and analyzed with SDS–PAGE and CBB staining. A *t* test was used to compare the Homer3 fraction in GDP and Gpp(NH)p conditions. Molecular weights were calculated by fitting to a standard curve generated using Precision Plus Protein All Blue Standards (161-0373; Bio-Rad, Hercules, CA).

Protein identification by mass spectrometry

Protein samples were concentrated and separated by one-dimensional SDS–PAGE. After Coomassie staining, each lane was cut into 24 slices and subjected to in-gel digestion with 100 ng of trypsin (Trypsin Gold; Promega, Madison, WI) before reduction

with 10 mM DTT and alkylation with 55 mM iodoacetamide. Peptide mixtures were trapped on a C18 reversed-phase EASY-Column and separated on a 100-mm C18 reversed-phase column (75 μm \times 100 mm, 3- μm particle size; Thermo Scientific, Waltham, MA) using a linear gradient from 0 to 35% (vol/vol) acetonitrile in 0.1% formic acid over 70 min at a constant flow rate of 300 nl/min. Nanoflow liquid chromatography–tandem mass spectrometry (LC-MS/MS) was performed on an EASYII LC system (Thermo Scientific) coupled to an LTQ-Orbitrap XL mass spectrometer (Thermo Scientific) operating in positive mode. MS scans were acquired in the Orbitrap in the range from 350 to 1800 m/z , with a resolution of 60,000 (full-width at half-maximum). The seven most intense ions per scan were submitted to MS/MS fragmentation (35% Normalized Collision Energy) and detected in the linear ion trap. Peak lists were obtained from raw data files using the Proteome Discoverer, version 1.3, software. Mascot (version 2.1; MatrixScience, Boston, MA) was used for searching against a sequence database obtained by combining the *Escherichia coli* with the *Homo sapiens* proteome sequences. The peptide tolerance was set to 40 ppm and the fragment ion tolerance to 2.0 Da, using semitrypsin as protease specificity and allowing for up to two missed cleavages. Oxidation of methionine residues, deamidation of asparagine and glutamine, and carboamidomethylation of cysteines were specified as variable modifications. Peptide and protein identifications were further validated with the program Scaffold (version 3.2; Proteome Software, Portland, OR). Protein identifications based on at least two unique peptides identified by MS/MS, each with a confidence of identification probability >95%, were accepted.

Mass spectrometry data analysis

The spectral counts as obtained from the proteomics analysis were used for further data analysis. For each sample, the counts were standardized by calculating the standardized score (Z_P) for each protein–bait combination according to $Z_P = \frac{X_P - \mu}{\sigma}$ where X_P is the spectral count for protein P , μ is the average count in the sample of the specific bait, and σ is the SD of the counts in the sample. Both the Z_P score and the counts were used to estimate the strength of the connection between the protein and the bait. Ranked lists of proteins for a specific bait were constructed by ordering the proteins on the basis of the ratio between the spectral counts in the sample with the bait compared with the control sample. To establish a lower level of the threshold for the counts, the counts of a set of scrambled protein sequences were used. This scrambled set had a median count of 1 and a maximum count of 5. Based on this, all proteins with a count <6 were regarded as false positives and not included in the ranked protein lists. Gene annotations for the Swiss-Prot accession numbers were obtained from the HGNC database (www.genenames.org). Data analysis and graph drawing were done with the statistical package R (www.r-project.org).

Calcium assay

Cells were incubated in medium containing 1 μM fluo-4 AM (F14201; Invitrogen) for 30 min at 37°C. Cells were plated on fibronectin and stimulated by gently adding 100 nM fMLP. Neutral density filters were used to attenuate the intensity of the fluorescence excitation light to prevent spontaneous calcium release. Positive calcium release was scored for cells exhibiting at least a threefold increase in fluorescence intensity.

Phospho-Pak and phospho-Akt assay

Cells were resuspended to a concentration of 2 million/ml in RPMI with 0.2% FBS. We stimulated cells with 10 nM fMLP and quenched the reaction at the indicated time points by adding aliquots of the cell mixture to ice-cold 20% trichloroacetic acid (TCA) containing the phosphatase inhibitors 40 mM NaF and 20 mM β -glycerol phosphate (50020; Fluka, St. Gallen, Switzerland). The samples were spun at 20,000 \times g for 15 min to pellet. The sample pellets were washed with 0.5% TCA and resuspended in Laemmli protein sample buffer (161-0737; Bio-Rad) containing 5% β -mercaptoethanol. Protein bands were separated by SDS-PAGE gel electrophoresis, transferred to nitrocellulose, blocked with Odyssey block, and incubated at 4°C overnight with 1:1000 dilutions of anti-phospho-PAK (2605S; Cell Signaling, Danvers, MA) and anti-Pak2 (4825S; Cell Signaling) or anti-phospho-Akt (4060S; Cell Signaling) and anti-Akt (40D4; Cell Signaling). The blot was developed with the fluorescent secondary antibodies, and protein bands were imaged using an Odyssey Infrared Imaging System (LI-COR Biosciences, Lincoln, NE).

Time-lapse migration assays

Three hundred thousand cells were centrifuged at 400 \times g for 2 min, resuspended in 12.5 μ l of mHBSS containing 2% BSA and 10 nM fMLP, and plated on 5 μ g/ml fibronectin-coated coverslips previously blocked with BSA. A coverslip was placed over the cell suspension, and the edges were sealed with a melted mixture of Vaseline, lanolin, and paraffin, forming a squeeze chamber. Starting 10 min after plating, cells were imaged by phase contrast every 10 s for 1 h on a Nikon TE-2000 with a 20 \times /0.5 numerical aperture objective. The cells were kept at 37°C using a thermostatic chamber.

Cell tracking was performed manually using the MTrackJ plug-in of ImageJ. Cells were scored as “motile” if the maximum displacement from the origin was $\geq 5 \mu\text{m}$ (approximately one-half a cell radius) over a given time frame. Error associated with manual rendering of images can result in low speeds in otherwise stationary cells, as well as in fluctuation in instantaneous velocity from any given frame. To determine pauses, a moving average of the instantaneous velocity from the current frame and three previous frames was calculated for each frame of each track. If the moving average fell one SD below the mean velocity, the cell was scored as paused.

Actin cosedimentation

Actin cosedimentation was carried out as described previously (36) with slight modifications. For preparation of purified Homer proteins, bacterially expressed GST proteins were purified with 1 ml of GSTrap FF (GE Healthcare) and precleared by centrifugation for 1 h at room temperature (TLA100 rotor, 80,000 rpm). Purified monomeric rabbit skeletal muscle actin was provided by the Mullins lab (University of California, San Francisco, San Francisco, CA). To obtain F-actin, 10 μM of monomeric actin was polymerized for at least 1 h at room temperature in polymerization buffer (10 mM Tris-HCl, pH 7.0, 100 mM KCl, 1 mM MgCl_2 , and 1 mM ATP). F-actin and 10 μM purified protein were incubated together for 45 min at room temperature before centrifugation for 1 h at room temperature (TLA100 rotor, 80,000 rpm). The pellets were then resuspended to the initial assay volume. Equal amounts of supernatant and resuspended pellet were analyzed by SDS-PAGE and Coomassie brilliant blue stain.

F-actin staining and live-cell imaging

Cells were resuspended in mHBSS with 0.2% BSA. Cells were stimulated with addition of 10 nM fMLP, fixed with 3.7% paraformaldehyde in intracellular buffer (140 mM KCl, 1 mM MgCl₂, 2 mM EGTA, 320 mM sucrose, 20 mM HEPES, pH 7.5), and incubated on ice for 20 min. After centrifugation at 400 × *g* for 2 min, the cell pellet was resuspended in intracellular buffer containing 0.2% Triton X-100 and 1:500 rhodamine-phalloidin and stained for 20 min. The cells were centrifuged, resuspended in mHBSS, and analyzed on a FACSAria (BD Biosciences). Size correction for fluorescence intensity was derived from the ratio of background fluorescence from unstained control and Homer3-knockdown cells. Data analysis was performed on FlowJo (TreeStar, Ashland, OR).

Hem1-YFP-expressing HL-60s with nonsense shRNA or Homer3 shRNA were plated using squeeze chambers in RPMI containing 10% FBS and uniform 100 nM fMLP. Cells were imaged with TIRF and analyzed with ImageJ. The polarization of Hem1 localization was calculated by finding the vector between the cell center of mass and the center of mass of the Hem1 signal. A moving average of the angle of polarization was calculated from the current frame and two previous frames. If the moving average was different from the current angle of polarization by <0.3 rad, that frame was considered to have persistent polarization.

ACKNOWLEDGEMENTS

We thank Leo Meyerovich for coding assistance for calculating moving averages, Elizabeth Zhang for assistance with initial image data analysis, Johnny Rodriguez and the Mullins lab for purified actin, and Marilyn Farquhar, Delquin Gong, and Doug Tischer for constructs. We also thank Grace Peng and members of the Weiner lab for helpful discussion and critical reading of the manuscript. This work was supported by National Institutes of Health Grant R01-GM084040 to O.D.W. and an American Heart Association Predoctoral Fellowship to J.T.W.

REFERENCES

1. Neptune ER, Bourne HR. Receptors induce chemotaxis by releasing the $\beta\gamma$ subunit of G(i), not by activating G(q) or G(s). *Proc Natl Acad Sci U S A*. 1997;94(26):14489–94.
2. Rickert P, Weiner OD, Wang F, Bourne HR, Servant G. Leukocytes navigate by compass: Roles of PI3K γ and its lipid products. *Trends Cell Biol*. 2000;10(11):466–73.
3. Wiege K, Le DD, Syed SN, Ali SR, Novakovic A, Beer-Hammer S, et al. Defective Macrophage Migration in $G\alpha i2$ - but Not $G\alpha i3$ -Deficient Mice . *J Immunol*. 2012;189(2):980–7.
4. Spangrude GJ, Heimfeld S, Weissman IL. Hematopoietic Stem. *Science* (80-). 1988;58–62.
5. Kumagai A, Hadwiger JA, Pupillo M, Firtel RA. Molecular genetic analysis of two G?? protein subunits in Dictyostelium. *J Biol Chem*. 1991;266(2):1220–8.
6. Oldham WM, Hamm HE. Heterotrimeric G protein activation by G-protein-coupled receptors. *Nat Rev Mol Cell Biol*. 2008;9(1):60–71.
7. Stephens L, Milne L, Hawkins P. Moving towards a Better Understanding of Chemotaxis. *Curr Biol*. 2008;18(11):485–94.
8. Welch HCE, Coadwell WJ, Ellson CD, Ferguson GJ, Andrews SR, Erdjument-Bromage H, et al. P-Rex1, a PtdIns(3,4,5)P₃- and $g\beta\gamma$ -regulated guanine-nucleotide exchange factor for Rac. *Cell*. 2002;108(6):809–21.
9. Dong X, Mo Z, Bokoch G, Guo C, Li Z, Wu D. P-Rex1 is a primary Rac2 guanine nucleotide exchange factor in mouse neutrophils. *Curr Biol*. 2005;15(20):1874–9.

10. Kunisaki Y, Nishikimi A, Tanaka Y, Takii R, Noda M, Inayoshi A, et al. DOCK2 is a Rac activator that regulates motility and polarity during neutrophil chemotaxis. *J Cell Biol.* 2006;174(5):647–52.
11. Tang W, Zhang Y, Xu W, Harden TK, Sondek J, Sun L, et al. A PLC β /PI3K γ -GSK3 Signaling Pathway Regulates Cofilin Phosphatase Slingshot2 and Neutrophil Polarization and Chemotaxis. *Dev Cell [Internet].* 2011;21(6):1038–50. Available from: <http://dx.doi.org/10.1016/j.devcel.2011.10.023>
12. Wang F. The signaling mechanisms underlying cell polarity and chemotaxis. *Cold Spring Harb Perspect Biol.* 2009;1(4):1–17.
13. Berzat A, Hall A. Cellular responses to extracellular guidance cues. *EMBO J [Internet].* 2010;29(16):2734–45. Available from: <http://dx.doi.org/10.1038/emboj.2010.170>
14. Gardiner EM, Pestonjamas KN, Bohl BP, Chamberlain C, Hahn KM, Bokoch GM. Spatial and temporal analysis of Rac activation during live neutrophil chemotaxis. *Curr Biol.* 2002;12(23):2029–34.
15. Sun CX, Downey GP, Zhu F, Koh ALY, Thang H, Glogauer M. Rac1 is the small GTPase responsible for regulating the neutrophil chemotaxis compass. *Blood.* 2004;104(12):3758–65.
16. Zhang H, Sun C, Glogauer M, Bokoch GM. Human Neutrophils Coordinate Chemotaxis by Differential Activation of Rac1 and Rac2. *J Immunol.* 2009;183(4):2718–28.
17. Yoo SK, Deng Q, Cavnar PJ, Wu YI, Hahn KM, Huttenlocher A. Differential Regulation of Protrusion and Polarity by PI(3)K during Neutrophil Motility in Live

- Zebrafish. *Dev Cell*. 2010;18(2):226–36.
18. Allen WE, Zicha D, Ridley AJ, Jones GE. A role for Cdc42 in macrophage chemotaxis. *J Cell Biol*. 1998;141(5):1147–57.
 19. Chung CY, Lee S, Briscoe C, Ellsworth C, Firtel RA. Role of Rac in controlling the actin cytoskeleton and chemotaxis in motile cells. *Proc Natl Acad Sci U S A*. 2000;97(10):5225–30.
 20. Levskaya A, Weiner OD, Lim WA, Voigt CA. Spatiotemporal control of cell signalling using a light-switchable protein interaction. *Nature*. 2009;461(7266):997–1001.
 21. Wu YI, Frey D, Lungu OI, Jaehrig A, Schlichting I, Kuhlman B, et al. A genetically encoded photoactivatable Rac controls the motility of living cells. *Nature*. 2009;461(7260):104–8.
 22. Weiner OD, Rentel MC, Ott A, Brown GE, Jedrychowski M, Yaffe MB, et al. Hem-1 complexes are essential for Rac activation, actin polymerization, and myosin regulation during neutrophil chemotaxis. *PLoS Biol*. 2006;4(2):186–99.
 23. Lebensohn AM, Kirschner MW. Activation of the WAVE Complex by Coincident Signals Controls Actin Assembly. *Mol Cell* [Internet]. 2009;36(3):512–24. Available from: <http://dx.doi.org/10.1016/j.molcel.2009.10.024>
 24. Chen Z, Borek D, Padrick SB, Gomez TS, Metlagel Z, Ismail AM, et al. Structure and control of the actin regulatory WAVE complex. *Nature*. 2010;468(7323):533–8.
 25. Koronakis V, Hume PJ, Humphreys D, Liu T, Hørning O, Jensen ON, et al. WAVE regulatory complex activation by cooperating GTPases Arf and Rac1. *Proc Natl*

- Acad Sci U S A. 2011;108(35):14449–54.
26. Servant G, Weiner OD, Herzmark P, Balla T, Sedat JW, Bourne HR. Polarization of chemoattractant receptor signaling during neutrophil chemotaxis. *Science* (80-). 2000;287(5455):1037–40.
 27. Kamakura S, Nomura M, Hayase J, Iwakiri Y, Nishikimi A, Takayanagi R, et al. The cell polarity protein minsc regulates neutrophil chemotaxis via a noncanonical G protein signaling pathway. *Dev Cell* [Internet]. 2013;26(3):292–302. Available from: <http://dx.doi.org/10.1016/j.devcel.2013.06.008>
 28. Li H, Yang L, Fu H, Yan J, Wang Y, Guo H, et al. Association between Gai2 and ELMO1/Dock180 connects chemokine signalling with Rac activation and metastasis. *Nat Commun*. 2013;4.
 29. Ishiguro K, Xavier R. Homer-3 regulates activation of serum response element in T cells via its EVH1 domain. *Blood*. 2004;103(6):2248–56.
 30. Shiraishi-Yamaguchi Y, Furuichi T. The Homer family proteins. *Genome Biol*. 2007;8(2):1–12.
 31. Shiraishi-Yamaguchi Y, Sato Y, Sakai R, Mizutani A, Knöpfel T, Mori N, et al. Interaction of Cupidin/Homer2 with two actin cytoskeletal regulators, Cdc42 small GTPase and Drebrin, in dendritic spines. *BMC Neurosci*. 2009;10:1–14.
 32. Kataria R, Xu X, Fusetti F, Keizer-Gunnink I, Jin T, Van Haastert PJM, et al. Dictyostelium Ric8 is a nonreceptor guanine exchange factor for heterotrimeric G proteins and is important for development and chemotaxis. *Proc Natl Acad Sci U S A*. 2013;110(16):6424–9.
 33. Anger T, Klintworth N, Stumpf C, Daniel WG, Mende U, Garlich CD. RGS protein

- specificity towards Gq- and Gi/o-mediated ERK 1/2 and Akt activation, in vitro. *J Biochem Mol Biol*. 2007;40(6):899–910.
34. Nafisi H, Banihashemi B, Daigle M, Albert PR. GAP1(IP4BP)/RASA3 mediates G α i-induced inhibition of mitogen-activated protein kinase. *J Biol Chem*. 2008;283(51):35908–17.
 35. Laliberté B, Wilson AM, Nafisi H, Mao H, Zhou YY, Daigle M, et al. TNFAIP8: A new effector for G α (i) coupling to reduce cell death and induce cell transformation. *J Cell Physiol*. 2010;225(3):865–74.
 36. Shiraishi Y, Mizutani A, Bito H, Fujisawa K, Narumiya S, Mikoshiba K, et al. Cupidin, an isoform of Homer/Vesl, interacts with the actin cytoskeleton and activated Rho family small GTPases and is expressed in developing mouse cerebellar granule cells. *J Neurosci*. 1999;19(19):8389–400.
 37. Foa L, Rajan I, Haas K, Wu GY, Brakeman P, Worley P, et al. The scaffold protein, Homer1b/c, regulates axon pathfinding in the central nervous system in vivo. *Nat Neurosci*. 2001;4(5):499–506.
 38. Fagni L, Worley PF, Ango F. Homer as both a scaffold and transduction molecule. *Sci STKE*. 2002;2002(137):1–8.
 39. Hwang SY, Wei J, Westhoff JH, Duncan RS, Ozawa F, Volpe P, et al. Differential functional interaction of two Vesl/Homer protein isoforms with ryanodine receptor type 1: A novel mechanism for control of intracellular calcium signaling. *Cell Calcium*. 2003;34(2):177–84.
 40. Moutin E, Raynaud F, Roger J, Pellegrino E, Homburger V, Bertaso F, et al. Dynamic remodeling of scaffold interactions in dendritic spines controls synaptic

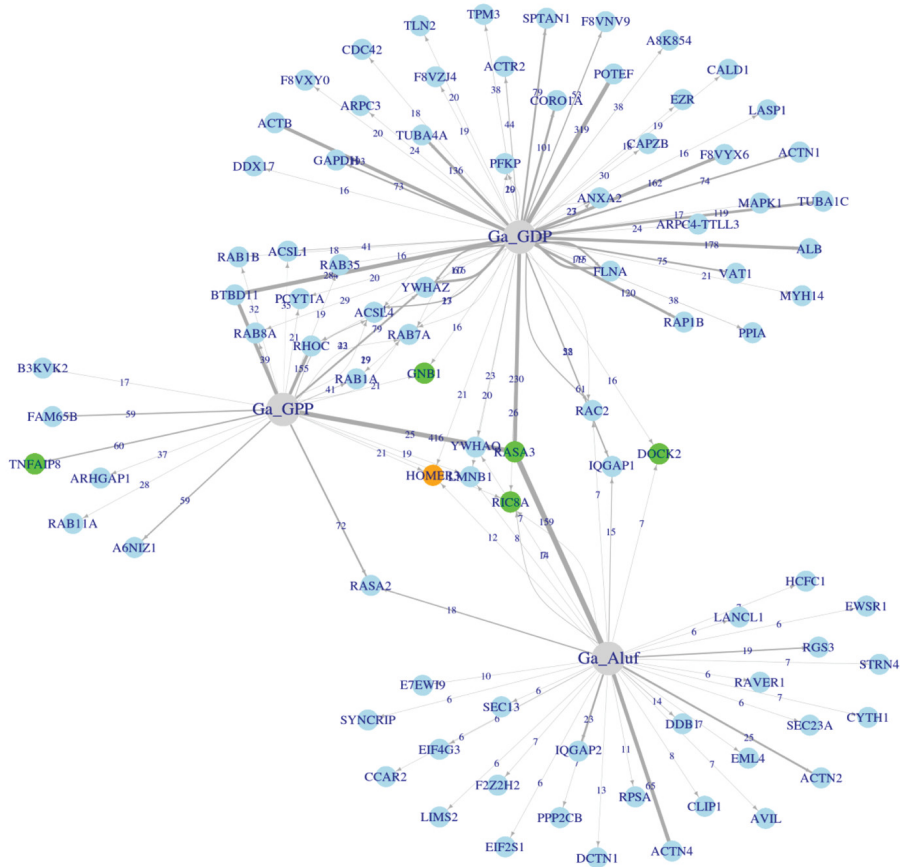
- excitability. *J Cell Biol.* 2012;198(2):251–63.
41. Hauert AB, Martinelli S, Marone C, Niggli V. Differentiated HL-60 cells are a valid model system for the analysis of human neutrophil migration and chemotaxis. *Int J Biochem Cell Biol.* 2002;34(7):838–54.
 42. Malawista SE, De Boisfleury Chevance A. Random locomotion and chemotaxis of human blood polymorphonuclear leukocytes (PMN) in the presence of EDTA: PMN in close quarters require neither leukocyte integrins nor external divalent cations. *Proc Natl Acad Sci U S A.* 1997;94(21):11577–82.
 43. Dandekar SN, Park JS, Peng GE, Onuffer JJ, Lim WA, Weiner OD. Actin dynamics rapidly reset chemoattractant receptor sensitivity following adaptation in neutrophils. *Philos Trans R Soc B Biol Sci.* 2013;368(1629):1–11.
 44. Weiss-Haljiti C, Pasquali C, Ji H, Gillieron C, Chabert C, Curchod ML, et al. Involvement of phosphoinositide 3-kinase γ , Rac, and PAK signaling in chemokine-induced macrophage migration. *J Biol Chem.* 2004;279(41):43273–84.
 45. Knaus UG, Morris S, Dong H, Chernoff J, Bokoch GM. Regulation of human leukocyte p21-activated kinases through G protein-coupled receptors. *Science* (80-). 1995;269:221–3.
 46. Franke TF, Yang S II, Chan TO, Datta K, Kazlauskas A, Morrison DK, et al. The protein kinase encoded by the Akt proto-oncogene is a target of the PDGF-activated phosphatidylinositol 3-kinase. *Cell.* 1995;81(5):727–36.
 47. Stokoe D, Stephens LR, Copeland T, Gaffney PRJ, Reese CB, Painter GF, et al. Dual role of phosphatidylinositol-3,4,5-trisphosphate in the activation of protein

- kinase B. *Science* (80-). 1997;277(5325):567–70.
48. Burgering BMT, Coffert PJ. Protein kinase B (c-Akt) in phosphatidylinositol-3-OH kinase signal transduction. *Nature*. 1995;(3):599–602.
 49. Hromas R, Collins S, Raskind W, Deaven L, Kaushansky K. Hem-1, a potential membrane protein, with expression restricted to blood cells. *Biochem Biophys Acta*. 1991;1090:241–4.
 50. Weiner OD, Marganski WA, Wu LF, Altschuler SJ, Kirschner MW. An actin-based wave generator organizes cell motility. *PLoS Biol*. 2007;5(9):2053–63.
 51. Glogauer M, Marchal CC, Zhu F, Worku A, Clausen BE, Foerster I, et al. Rac1 Deletion in Mouse Neutrophils Has Selective Effects on Neutrophil Functions. *J Immunol*. 2003;170(11):5652–7.
 52. Yan J, Mihaylov V, Xu X, Brzostowski JA, Li H, Liu L, et al. A G β γ Effector, ElmoE, Transduces GPCR Signaling to the Actin Network during Chemotaxis. *Dev Cell* [Internet]. 2012;22(1):92–103. Available from: <http://dx.doi.org/10.1016/j.devcel.2011.11.007>
 53. Lawson CD, Donald S, Anderson KE, Patton DT, Welch HCE. P-Rex1 and Vav1 Cooperate in the Regulation of Formyl-Methionyl-Leucyl-Phenylalanine–Dependent Neutrophil Responses. *J Immunol*. 2011;186(3):1467–76.
 54. Ku CJ, Wang Y, Weiner OD, Altschuler SJ, Wu LF. Network crosstalk dynamically changes during neutrophil polarization. *Cell* [Internet]. 2012;149(5):1073–83. Available from: <http://dx.doi.org/10.1016/j.cell.2012.03.044>
 55. Park JS, Rhau B, Hermann A, McNally KA, Zhou C, Gong D, et al. Synthetic control of mammalian-cell motility by engineering chemotaxis to an orthogonal

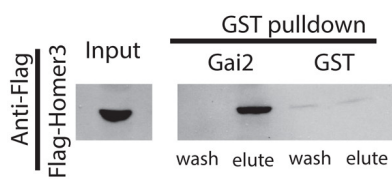
- bioinert chemical signal. *Proc Natl Acad Sci U S A*. 2014;111(16):5896–901.
56. Ghosh P, Garcia-Marcos M, Bornheimer SJ, Farquhar MG. Activation of Gα_{i3} triggers cell migration via regulation of GIV. *J Cell Biol*. 2008;182(2):381–93.
57. Smith SJM, Rittinger K. Preparation of GTPases for Structural and Biophysical Analysis. In: Manser E, Leung T, editors. *GTPase Protocols: The Ras Superfamily* [Internet]. Totowa, NJ: Springer New York; 2002. p. 13–24. Available from: <https://doi.org/10.1385/1-59259-281-3:013>

FIGURE 2.1

A



B



C

	beads				Homer3	Homer3			
	GST		Gai2			GST		Gai2	
GDP	+	-	+	-	-	+	-	+	-
Gpp(NH)p	-	+	-	+	-	-	+	-	+
Homer3	-	-	-	-	+	+	+	+	+

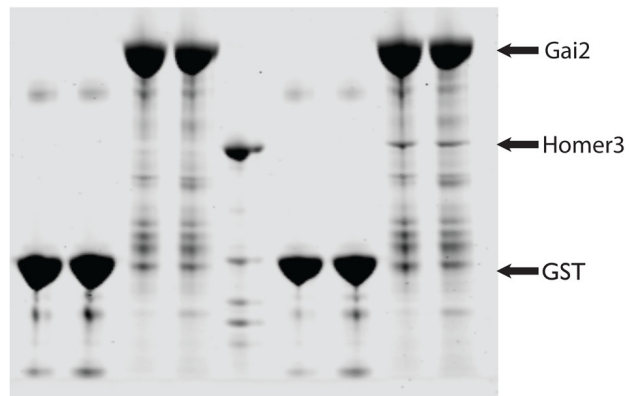


Figure 2.1. Identification of Homer3 as a neutrophil protein that binds Gai2.

(A) Network analysis of the proteins captured by one or more Gai2 baits after affinity chromatography in pig leukocyte lysates. The baits are shown in gray, and the proteins are shown in blue. For each protein–bait combination, the numbers at the arrows show the counts, and the width of the lines represents the Z_P score.

(B) Affinity chromatography with GST-Gai2 or GST alone for neutrophil lysate containing FLAG-Homer3. Eluted GST-tagged bait plus associated proteins and final wash fraction were subjected to SDS–PAGE and analyzed by immunoblot with anti-FLAG antibody.

(C) Affinity chromatography–based test for direct interaction between purified, bacterially expressed Homer3 (prey) and GST-Gai2 or GST alone (baits). Homer3 directly binds to both GST-Gai2-GDP and GST-Gai2-Gpp(NH)p with similar affinity ($n = 5$; not significantly different). “Beads” refer to baits without Homer3 (prey). Samples were analyzed with SDS–PAGE and stained with CBB. Arrows indicate GST-Gai2 (66 kDa), Homer3 (47 kDa), and GST (26 kDa).

FIGURE 2.2

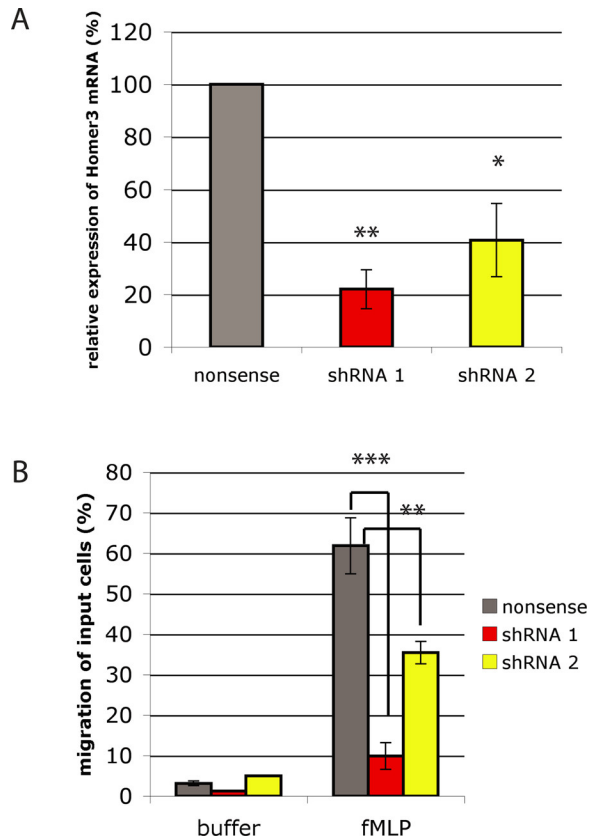


Figure 2.2 Homer3 knockdown impairs HL-60 chemotaxis.

(A) RNA was isolated from control cells (nonsense shRNA) and HL-60 cell lines expressing one of two different Homer3 shRNAs (shRNA 1 and shRNA 2). Relative expression of Homer3 was quantified by quantitative real-time PCR using GAPDH as a reference gene. Results represent the mean with SD of three replicates.

(B) Migration of control or Homer3-knockdown differentiated HL-60 cells in response to 10 nM fMLP measured via Transwell chemotaxis chambers after 2 h. Results are a representative example of five independent experiments. * $p < 0.05$, ** $p < 0.005$, *** $p < 0.0005$ by unpaired t test.

FIGURE 2.3

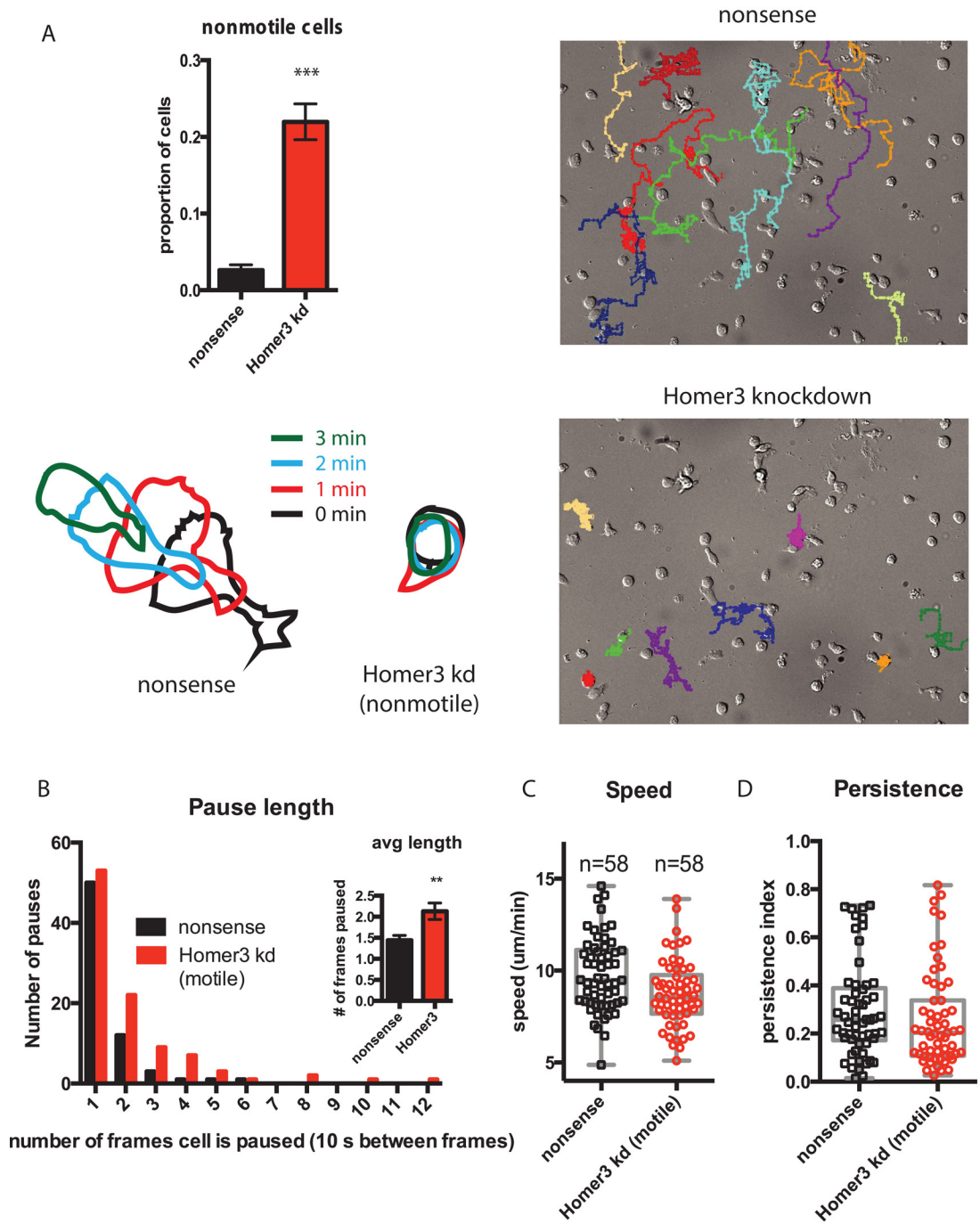


FIGURE 2.3 Homer3 knockdown impairs the initiation of HL-60 migration.

(A) Percentage of nonmotile cells in time-lapse migration assays in uniform 10 nM fMLP, expressed as mean with SE. Results are from three independent experiments with two replicates each. $***p < 0.0005$ by unpaired t test. Corresponds to Supplemental Movies S1 and S2. Representative cell tracks of nonsense and Homer3-knockdown cells. Corresponds to Supplemental Movie S3.

(B) Length of pauses in migration tracks, as defined in *Materials and Methods*. $**p < 0.005$ by Mann–Whitney test. Corresponds to Supplemental Movie S4.

(C) Speed of control (nonsense shRNA) and motile Homer3-knockdown cells was assayed via time-lapse microscopy. Dot plot shows the overall population distribution; box and whiskers plots show quartiles.

(D) Persistence index, defined as (final distance from start)/(total distanced traveled).

FIGURE 2.4

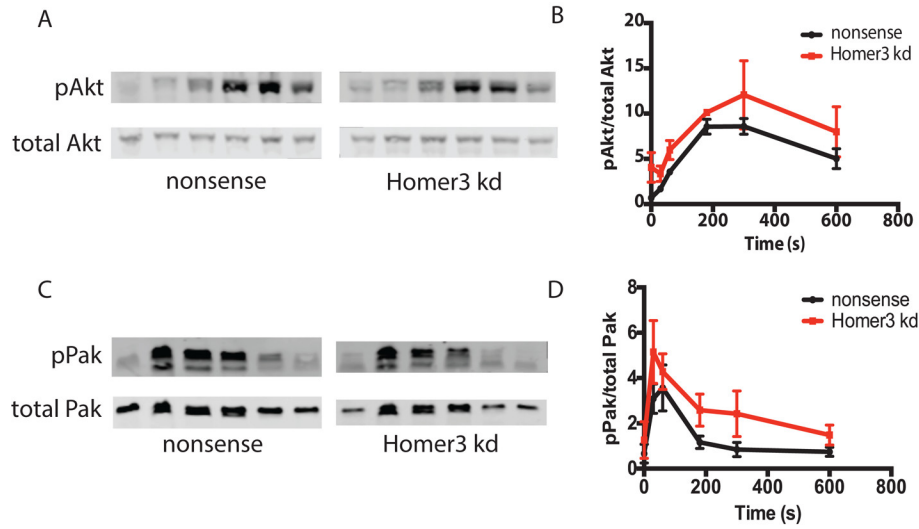


FIGURE 2.4 Homer3 depletion does not affect levels of Pak phosphorylation (a readout of Rac activation) or Akt phosphorylation (a readout of PIP₃ generation).

(A, C) Time course of Akt **(A)** or Pak **(C)** phosphorylation, measured by Western blot, after uniform 10 nM fMLP stimulation. Total Akt **(A)** or total Pak **(C)** was used as loading control.

(B, D) Quantification of phosphorylated Akt **(B)** or Pak **(D)** for three independent runs of the experiment shown in A and C, respectively. Phosphorylated Akt **(B)** or Pak **(D)** was normalized to total Akt **(B)** or Pak **(D)**.

FIGURE 2.5

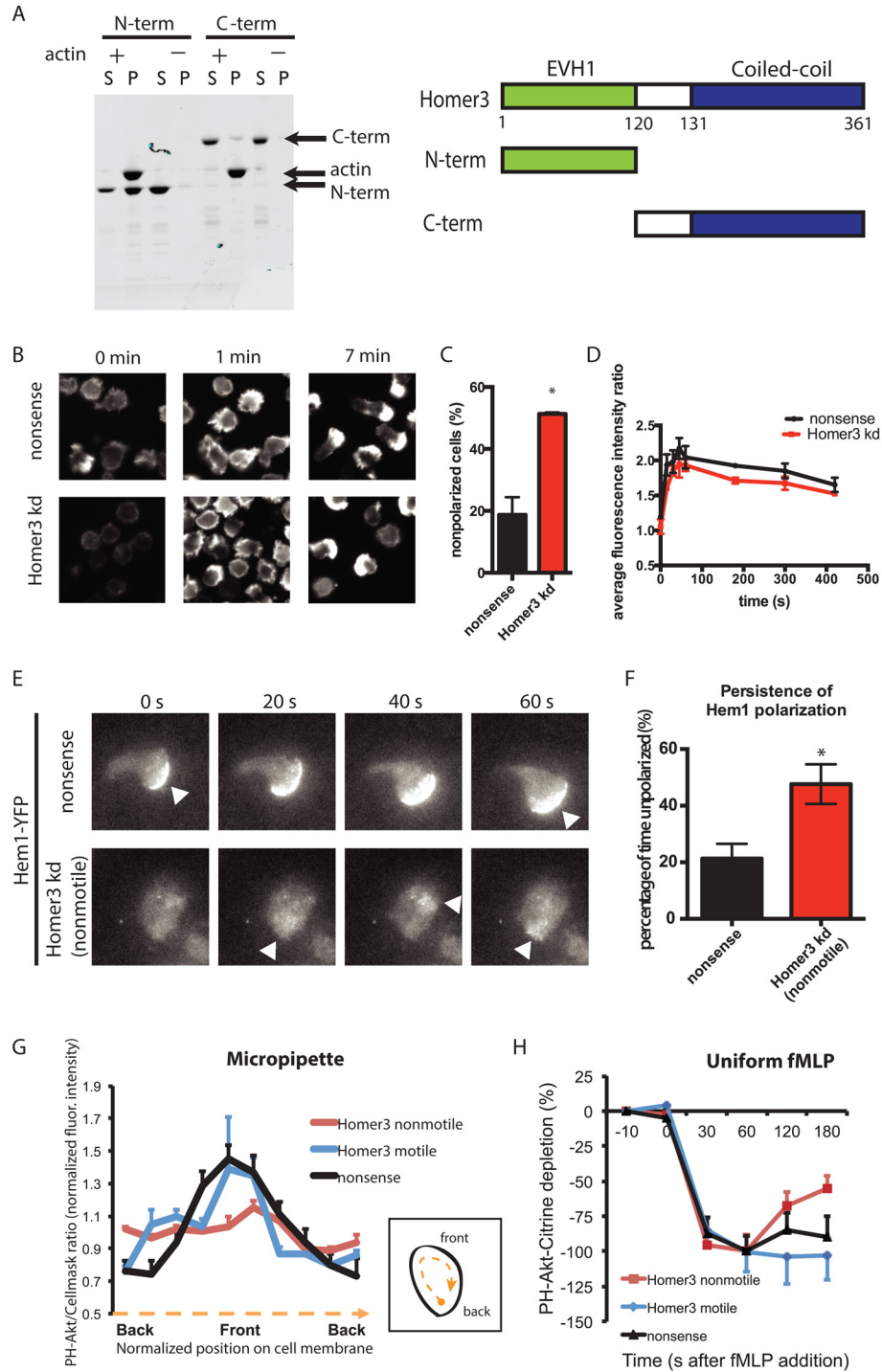


FIGURE 2.5 Homer3 is an actin-binding protein necessary for persistent actin and PIP₃ polarization.

(A) A cosedimentation assay reveals that the N-terminal portion of Homer3 is necessary and sufficient to directly bind F-actin. Purified, bacterially expressed GST–N-terminal (N-term) and GST–C-terminal (C-term) fragments of Homer3 were incubated with (+) and without (–) F-actin and then centrifuged. Equal amounts of the supernatant (S) and pellet (P) fractions were separated by SDS–PAGE and stained with CBB. Arrows indicate C-term (53 kDa), actin (42 kDa), and N-term (40 kDa). Schematic of Homer3 and the truncated proteins. (B–D) Differentiated control (nonsense shRNA) or Homer3-knockdown HL-60 cells were stimulated in suspension with 10 nM fMLP. At the time points indicated, cells were fixed and stained with rhodamine-phalloidin to visualize F-actin.

(B) Representative epifluorescence images before stimulation (0 min), at peak response (1 min), and after polarization (7 min).

(C) Quantification of proportion of polarized cells at the 7-min time point for control ($n = 577$) and Homer3-knockdown ($n = 754$) cells. Results are the mean and SE of three independent experiments. Asterisk represents $p < 0.05$ by unpaired t test.

(D) Average fluorescence intensity of the whole-cell population, as quantified by FACS, was measured and normalized to the unstimulated control population to correct for FACS and staining variation between experiments. Results are the mean and SE of three independent experiments.

(E) Polarization of actin nucleation was assessed by TIRF imaging of a fluorescent component of the WAVE complex (Hem1-YFP) for cells exposed to uniform 100 nM fMLP in a squeeze chamber. Images are representative of at least 10 cells. Arrowheads indicate regions of increased Hem1 intensity. Corresponds to Supplemental Movies S4 and S5.

(F) Persistence of Hem1-YFP polarization was quantified as described in Materials and Methods for nonsense ($n = 5$) and Homer3-knockdown ($n = 6$) cells. $*p < 0.05$ by unpaired t test.

(G) Line-scan analysis of the ratio images shown in Supplemental Figure S4. Differentiated HL-60 cells (nonsense shRNA or Homer3 shRNA) expressing PH-Akt-Citrine and labeled with CellMask Orange were stimulated with fMLP released from a micropipette. The normalized ratio values between PH-Akt-Citrine and CellMask Orange within the cell periphery were calculated, with each cell normalized such that the average of all ratios along each cell edge is 1. The cell edge of each cell was divided into 10 angular sectors, and values were averaged within each angular sector. Internalized CellMask Orange vesicles were excluded from analysis. Error bars are SE ($n = 5$ for each line). The difference between nonsense and Homer3 knockdown (motile) is not significant by F test, whereas the difference between nonsense and Homer3 knockdown (nonmotile) is significant ($p < 0.005$) by F test.

(H) Cytoplasmic depletion of PH-Akt-Citrine after addition of 100 nM fMLP. Normalized average fluorescence in a cytoplasmic region was measured at the time points indicated (100% is the maximum depletion in the control line). Error bars are SE ($n = 10$ for each line). No significant differences by t test.

FIGURE S2.1

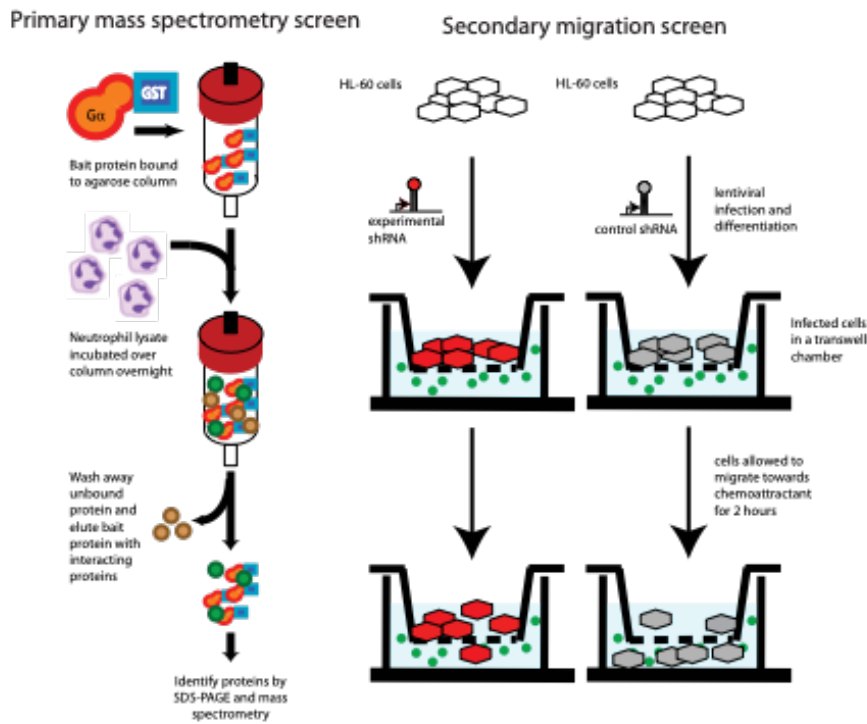


FIGURE S2.1 Schematics for biochemical and genetic screens

Affinity chromatography/mass spec was used to identify Gai-binding proteins from neutrophil lysate (left), and transwell migration assays (right) was used to test the involvement of potential Gai effectors in neutrophil chemotaxis.

FIGURE S2.2

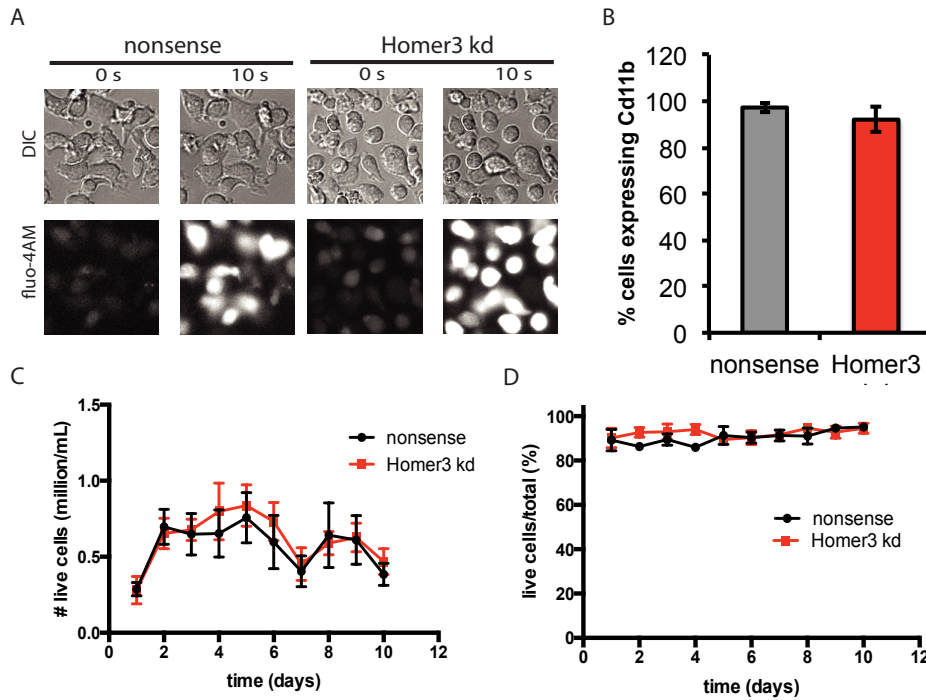


FIGURE S2.2 Homer3 knockdown does not affect calcium signaling, differentiation, or cell viability

(A) Both control (407 of 451 cells, 90%) and Homer3 knockdown (465 of 546 cells, 85%) cells release calcium in response to stimulation with 100 nM fMLP, as assayed by the calcium indicator fluo-4 AM. Representative transmitted light and epifluorescence images of control and Homer3 knockdown cells before and after fMLP stimulation.

(B) Differentiated control and Homer3 knockdown cells were stained with PE-conjugated antibody for Cd11b and measured for fluorescence via FACS. Threshold for differentiation determined by unstained and undifferentiated controls.

(C) and **(D)** HL-60 cell lines expressing either Homer3 shRNA or nonsense (control) shRNA were grown as described in *Materials and Methods*. Cells were counted daily using the Countess automated cell counter (Life Technologies) **(C)**, and viability was assessed with trypan blue **(D)**. Cells were then split to a density of 0.3 million/mL each day for ten days. Results represent the mean with standard deviation of three replicates.

FIGURE S2.3

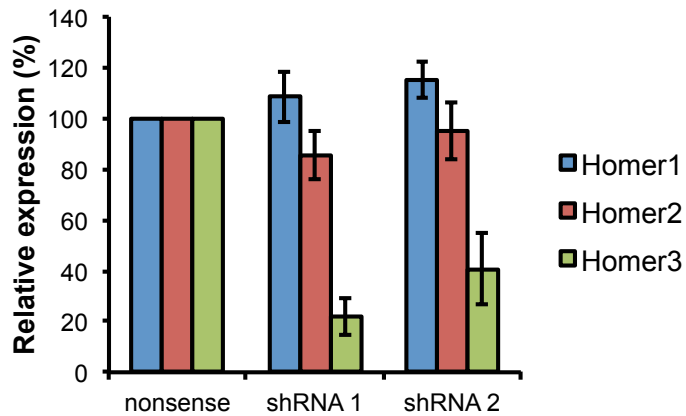


FIGURE S2.3 Homer3 knockdown does not affect Homer1 or Homer2 expression

RNA was isolated from control cells (nonsense shRNA) and HL-60 cell lines expressing one of two different Homer3 shRNAs (shRNA 1 and shRNA 2). Relative expression of Homer1, 2, and 3 was quantified by qRT-PCR using GAPDH as a reference gene. Results represent the mean with standard deviation of three replicates.

FIGURE S2.4

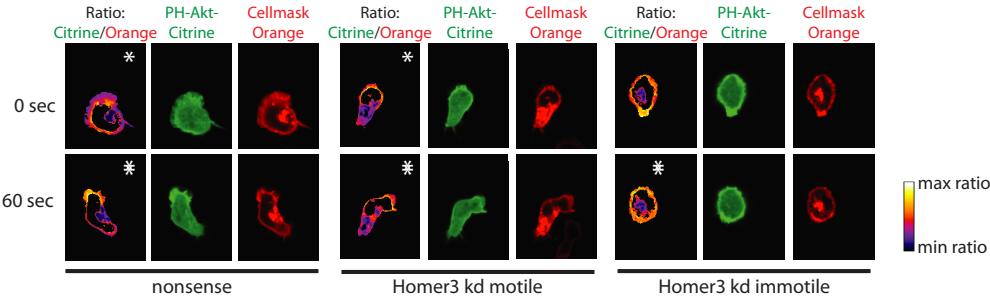


FIGURE S2.4 Homer3 depletion impairs polarized PIP3 accumulation in response to directional chemoattractant cues

Differentiated HL-60 cells (nonsense shRNA or Homer3 shRNA) expressing PH-Akt-Citrine (green) and labeled with CellMask Orange (red) were stimulated with fMLP released from a micropipette. Ratiometric images (PH- Akt-Citrine versus CellMask Orange) are also shown. Asterisk represents the source of the fMLP.

CHAPTER THREE

WAVE COMPLEX SELF-ORGANIZATION TEMPLATES

LAMELLIPODIAL FORMATION

“What is safe? Doing what everybody wants you to do may not be safe.”
- Wallace Marshall

SUMMARY

How local interactions of actin regulators yield large-scale organization of cell shape and movement is not well understood. For example, why does the WAVE complex build lamellipodia, the broad sheet-like protrusions that power cell migration, whereas the homologous actin regulator N-WASP forms spiky finger-like actin networks? N-WASP is known to oligomerize into focal condensates that generate an actin finger. In contrast, the WAVE complex exhibits the linear distribution needed to generate an actin sheet. This linear organization of the WAVE complex could either arise from interactions with the actin cytoskeleton or could represent an ability of the complex to self-organize into a linear template. Using super-resolution microscopy, we find that the WAVE complex forms higher-order linear oligomers that curve into 270 nanometer-wide ring structures in the absence of actin polymer. These rings localize to the necks of membrane invaginations, which display saddle point geometries with positive curvature in one axis and negative curvature in the orthogonal axis. To investigate the molecular mechanism of saddle curvature enrichment, we show that the WAVE complex and IRSp53, a membrane curvature-sensitive protein, collaborate to recognize saddle curvature that IRSp53 cannot sense alone. This saddle preference for the WAVE complex could explain emergent cell behaviors, such as expanding and self-straightening lamellipodia as well as the ability of endothelial cells to recognize and seal transcellular holes. Our work highlights how partnering protein interactions enable complex shape sensing and how feedback between cell shape and actin regulators yields self-organized cell morphogenesis.

INTRODUCTION

Cells manipulate the shape of their plasma membranes to execute a range of physiological functions from building the protrusions that drive cell motility to coordinating the membrane deformations that enable endocytosis. Actin polymerization plays a major role in coordinating these processes, but how cells specify the proper pattern of actin assembly to achieve these distinct shapes is unclear. Cells use nucleation-promoting factors (NPFs) to spatially and temporally control their patterns of actin polymerization (1,2). For example, neural Wiskott-Aldrich syndrome protein (N-WASP) and WASP-family verprolin homologous protein (WAVE) activate the actin-related protein 2/3 (Arp2/3) complex to seed actin nucleation (3,4). N-WASP and WAVE are nested in similar signaling topologies — both are stimulated by phosphoinositides, Rho GTPases, and curvature-sensitive Bin-amphiphysin-Rvs (BAR) domain proteins, both activate the Arp2/3 complex, both are recycled in an actin-dependent fashion, and both show evidence of oligomerization at the membrane (1,4–11) (**Fig 1A**). Despite these similarities, the structures they build are distinct: N-WASP participates in spiky filopodial protrusions, invadopodia, and endocytic vesicles (1,12–20), whereas WAVE participates in broad, sheet-like lamellipodial protrusions (21–24). The basis for this difference in NPF-induced cell morphology is not understood.

Biochemical reconstitutions have provided insights into how different patterns of actin nucleation lead to different morphological structures. Spatially unconstrained activation of the Arp2/3 complex produces filopodial-like structures on giant unilamellar vesicles (25). In contrast, spatially organizing Arp2/3 complex activation in a linear geometry (via

glass rods (26) or UV micropatterned surfaces (27)) produces lamellipodial-like structures. These data suggest that while spiky, finger-like actin structures are the default morphology for the Arp2/3 complex activation on membranes, lamellipodium formation requires a linear structural template (28). What forms the basis of the linear template for lamellipodia in living cells is not known.

In cells, N-WASP forms the focal structure expected for finger-like protrusions (17,18,29), and the WAVE complex propagates as linear waves at the edges of lamellipodia (7,30). In the case of N-WASP, biochemical reconstitutions recapitulate its *in vivo* distribution: N-WASP and its multivalent binding partners generate biomolecular condensates (29,31). In the presence of the Arp2/3 complex and actin, these puncta-shaped condensates promote focal bursts of F-actin that produce spiky protrusions (31). In contrast, we do not know the basis of WAVE's linear organization in cells (**Fig 1B**).

The WAVE complex is required for proper cell migration and shape maintenance across eukaryotes including mammals, amoeba, and plants (4,7,23,30,32–34). As a pentameric heterocomplex, the WAVE complex contains the subunits WAVE, Abi, HSPC300, Sra1/Cyfp1, and Nap1/Hem1 (22,35,36). In neutrophils and other motile cells, the dynamics of the WAVE complex closely corresponds to the leading edge's morphology and pattern of advance (7). The WAVE complex is required for the formation of lamellipodia and efficient chemotaxis (directed cell migration); previous work found that siRNA knockdown and CRISPR-Cas9 gene inactivation of the WAVE complex in

neutrophil-like differentiated HL60 cells (dHL60s) and other immune cells results in defective chemotaxis and lamellipodia formation (22–24,37–39).

Here, we investigate how the WAVE complex achieves the linear distribution essential for lamellipodial actin organization. We found that, in the absence of actin polymer, the WAVE complex forms nanoscale oligomeric ring structures that associate with regions of membrane that have saddle point curvature. To further explore saddle curvature enrichment, we analyzed the WAVE complex's localization to transendothelial cell macroaperture (TEMs) tunnels, which are transcellular holes that leukocytes and various pathogens generate in endothelial cells to cross tissue barriers (40). As the endothelial cell seals the hole, the TEM displays persistent saddle curvature (41). We found that the WAVE complex enriches to closing TEMs, which suggests it may have a role in linking the recognition to the sealing of TEMs. To identify a potential mechanism of membrane curvature recognition, we explored the WAVE complex's partnering interactions with IRSp53, an inverse BAR domain protein, and found that their collaboration is required for IRSp53 to recognize lamellipodial and saddle curvature geometries. We propose that the WAVE complex's nanoscale, oligomeric assembly could explain emergent, self-organizing behaviors of cell morphogenesis including expanding and self-straightening lamellipodia and the recognition and closure of transcellular holes.

RESULTS

In neutrophil-like dHL60 cells and a range of other motile cells, the WAVE complex can be seen propagating as a linear “wave” structure at the edges of membrane ruffles and lamellipodia (**Fig 1C**). The WAVE complex’s propagating dynamics are thought to account for many behaviors of motile cells, such as continuous extending fronts and the ability to migrate around barriers (7). This dynamic propagation arises from an excitable feedback network with positive feedback (WAVE recruits more WAVE) and negative feedback loops (WAVE stimulates actin polymerization, which inhibits WAVE association with the membrane) (7,42). One source of negative feedback appears to be the force of actin polymerization that strips WAVE off the plasma membrane (42). In contrast, the mechanism and spatial organization of positive feedback, i.e. WAVE self-association, are not well understood. We were particularly interested in understanding whether the linear patterns of the WAVE complex in lamellipodia are dependent on an interaction between these positive and negative feedback loops, as is the case for other excitable networks (43), or whether the WAVE complex’s self-association has a specific geometric organization (**Fig 2A**). We can use inhibitors of actin polymerization to deplete F-actin to distinguish the two models and assay whether the WAVE complex maintains a stereotyped linear structure independently of F-actin.

When we previously visualized the pattern of the WAVE complex organization (via fluorescently-tagged hematopoietic protein 1 [Hem1], a subunit of the WAVE complex) in the absence of the actin cytoskeleton, standard total internal reflection fluorescence (TIRF) microscopy showed amorphous punctate structures of the WAVE complex (7). For

our current study, we revisited this experiment with super-resolution microscopy, which enables us to investigate any previously diffraction-limited organization of the WAVE complex. We leveraged TIRF-structured illumination microscopy (TIRF-SIM), a super-resolution technique that enables a 2-fold increase in resolution in the TIRF plane. When the F-actin inhibitor latrunculin A was acutely added to dHL60 cells to deplete F-actin, TIRF-SIM imaging of Hem1-eGFP revealed that the WAVE complex organizes into highly stereotyped 270nm-wide ring structures (**Fig 2B-D**). Importantly, super-resolution microscopy was required to resolve the nanometer-scale ring structures because they otherwise appear as amorphous blob-like structures by conventional TIRF (**Fig 2C**).

We observed two modes of ring generation: either *de novo* formation by recruitment of new WAVE complex to the plasma membrane following actin depolymerization or redistribution of membrane-bound WAVE complex from lamellipodia that locally “collapsed” into rings (**S1 Fig**). The WAVE complex rings were observed across a range of F-actin inhibitors and concentrations (**S2 Fig**), super-resolution modalities (**S3A Fig**), tagged fluorescent proteins (**S3B Fig**), cell types, and specific WAVE complex subunits (**S3C Fig**). Since latrunculin treatment results in lowered plasma membrane tension (44), the rings may represent the favored oligomeric organization of the WAVE complex when freed from the constraints of the cytoskeleton and tension in the plasma membrane. These experiments suggest that the WAVE complex’s positive feedback forms nanoscale, oligomeric rings.

Next, we wondered how these rings are organized relative to the morphology of the membrane. During cell migration, the WAVE complex is closely associated with the propagating edge of lamellipodial protrusions (**Fig 1C**). When imaging the WAVE complex and the plasma membrane in the absence of F-actin, we found that the WAVE complex rings localized to the boundary where coverslip-opposed membrane leaves the TIRF field (**Fig 3A**). This membrane distribution suggests an association to the necks of membrane invaginations (**Fig 3B**), and electron microscopy experiments are consistent with this membrane geometry (**S4 Fig**).

WAVE complex's propensity to enrich around the necks of membrane invaginations may give insight into the WAVE complex's membrane geometry preferences. The geometry of the necks of membrane invaginations from the cytosolic/WAVE complex's perspective consists of saddle points, defined by principal curvatures that are positive in one axis (the curve around the invagination neck) and negative in the other axis (the curve perpendicular to the invagination neck) (**Fig 3C**). Saddle geometries are not only present at membrane invaginations but also at areas of the protruding lamellipodium that transiently fall behind or "lag" (**Fig 3D**). As the membrane extends, it is laterally non-uniform and displays positive and negative curvatures (**Fig 3D left**) while it maintains an axial, sheet-like negative curvature (**Fig 3D right**). In order to maintain a coherent protruding lamellipodium, the lagging portion, which exhibits positive curvature, must become less positively curved, i.e. straighten, and accelerate to "catch up" (**Fig 3E**). This acceleration could be mediated by a localized increase in F-actin polymerization, via WAVE complex NPF activity, to push and straighten the lagging regions of the

lamellipodium. The result of these interactions would be a homeostatic self-straightening mechanism for a saddle-enriching WAVE complex.

To further explore the role that saddle curvature recognition may have in the emergent control of cell shape, we took advantage of transendothelial cell macroaperture (TEM) tunnel physiology. As leukocytes undergo diapedesis out of the blood vessel, they can migrate either in between endothelial cells or they can generate a TEM, a transcellular hole, to migrate through an endothelial cell (40). The hole is formed from fusing the apical and basal plasma membrane of the endothelial cell (45). To heal the transcellular hole and prevent pathogen dissemination, the affected endothelial cell has mechanisms to seal the TEM (46–48). The sealing process requires the recognition of TEMs, which exhibit saddle curvature, and subsequent closure of the hole (**Fig 4A-B**) (46). TEM closure is mediated by actin and the Arp2/3 complex dependent mechanisms (**S5 Fig**), but the relevant Arp2/3 complex activator has not been identified (46,49). Closure has been characterized as lamellipodial-like (47), where the height of the TEM edge is ~100nm by atomic force microscopy measurements (46). As TEMs close, the negative curvature of the lamellipodia-like extension remains constant while the positive curvature around the TEM increases (fractions of microns⁻¹ to microns⁻¹) (46,50). To generate TEMs, we inhibited actomyosin contractility, which is also the mechanism that some pathogens use to generate TEMs (40,46,47,49). For this purpose, we studied HUVECs (human umbilical vein endothelial cells) treated with ROCK inhibitor Y27632. In this experimental setup, we imaged the WAVE complex (via fluorescently-tagged Nap1, a homologue of Hem1) and found that it also enriched to TEMs (**Fig 4C**). In addition to

localizing to the necks of membrane invaginations in F-actin inhibited dHL60 cells, the WAVE complex's TEM association represents another example of saddle enrichment (**Fig 4D**).

Next, we sought to understand how the WAVE complex recognizes saddle geometries. As saddles have both negative and positive curvatures, there may be two domains that sense the different curvatures. Though the WAVE complex has membrane-binding motifs (6), it lacks any well-characterized curvature sensing motifs. However, the WAVE complex does directly interact with IRSp53 (insulin receptor tyrosine kinase substrate protein of 53 kDa; human ortholog is BAIAP2 [brain-specific angiogenesis inhibitor 1-associated protein 2]), a member of the inverse BAR (I-BAR) domain family of curvature-sensitive proteins (10,11,51). I-BAR domains dimerize into a convex geometry that binds phosphoinositide-rich membranes and are the canonical negative curvature sensing motif that associates with lamellipodia and filopodia (52–55). IRSp53 has an I-BAR domain at its N-terminus and a number of protein-protein interaction domains including a Src homology 3 (SH3) domain that binds to the WAVE complex's proline-rich domain (10,51,56) (**Fig 5A**).

To explore the range of geometries sensed by IRSp53, we imaged IRSp53-eGFP in dHL60 cells. Full-length IRSp53 localized to multiple areas of negative curvature: lamellipodia (10,11,51,57,58), filopodia-like tubules (57–60), and rings (**Fig 5B-C**). Importantly, high expression of IRSp53 is sufficient to form ring structures even without F-actin inhibition. When cells were treated with a F-actin inhibitor, IRSp53 also localized

to ring structures (**Fig 5D**). IRSp53 rings formed with or without F-actin present had comparable diameters to the WAVE complex rings formed without F-actin present (**Fig 5E**). This characteristic size suggests a preferred geometry for IRSp53 and the WAVE complex's membrane recruitment in cells.

To probe whether the WAVE complex follows IRSp53 to sites of negative curvature, we imaged IRSp53 and the WAVE complex in the same cell (via IRSp53-eGFP and Hem1-mCherry). IRSp53 and the WAVE complex only co-localized at protruding lamellipodia during cell migration (**Fig 5F-G**). In addition to lamellipodial enrichment, IRSp53 also localized to filopodia-like tubules, whereas the WAVE complex was restricted to the lamellipodium. These data suggest that the WAVE complex does not follow IRSp53 to all sites of negative curvature. When cells were treated with a F-actin inhibitor, both the WAVE complex and IRSp53 co-localized to ring structures (**Fig 5F-G**), consistent with both proteins showing saddle curvature enrichment. While IRSp53 localized to multiple sites displaying negative curvature, the WAVE complex was specifically enriched to lamellipodia and regions of saddle curvature.

Since the WAVE complex and IRSp53 colocalize in a subset of cell structures, we wondered whether IRSp53's localization pattern is partially dependent on its interactions with the WAVE complex. IRSp53 consists of several functional domains that could contribute to its localization, in particular an I-BAR domain that senses negative curvature and an SH3 domain that interacts with the WAVE complex. To investigate how these domains contribute to the overall pattern of IRSp53 enrichment, we generated two

structure-function constructs tagged with eGFP at the C-terminus: an “I-BAR” only domain that consisted of IRSp53’s first 250 amino acids and a “C-term” only construct that lacks the I-BAR domain but contains the region that interacts with the WAVE complex (**Fig 6A**). While full-length IRSp53 enriched to both lamellipodia and filopodia-like structures, the I-BAR domain preferentially enriched to filopodia-like structures, and the C-term domain remained cytosolic (**Fig 6B**). In latrunculin-treated cells, full-length IRSp53 formed rings while the I-BAR and C-term constructs failed to enrich as ring structures (**Fig 6C**). These data suggest that IRSp53 requires both its I-BAR domain and its C-terminal portion, containing its SH3-WAVE complex interacting domain, to properly enrich to lamellipodia and saddle points.

Since IRSp53’s SH3 domain interacts with other actin regulators besides the WAVE complex, such as Mena (59), Eps8 (61), and mDia1 (56), we tested whether IRSp53’s localization patterns are dependent on the WAVE complex by imaging full-length IRSp53-eGFP in WAVE complex depleted cells. The WAVE complex was depleted via CRISPR-Cas9-mediated knock out of Hem1, which resulted in the depletion of the other subunits (23,24,62). Upon F-actin inhibition, full-length IRSp53 failed to robustly form rings in the WAVE complex depleted cells (**Fig 6D**). These data suggest that while IRSp53’s I-BAR domain is sufficient to enrich to filopodia-like structures, IRSp53 requires its I-BAR domain and its interactions with the WAVE complex to localize to lamellipodia and saddle geometries (**Fig 6G**). Our data highlight how proteins can partner together to sense complex geometries.

To probe the generality of IRSp53 requiring both its I-BAR domain and its ability to bind to the WAVE complex to sense saddle curvature, we again used the HUVEC TEMs system, which has the advantage of providing a persistent saddle morphology. A previous study found that IRSp53's isolated I-BAR domain fails to recognize TEMs (46), and we confirmed these results in our hands (**Fig 6E-F**). This is consistent with our observation that the isolated I-BAR construct failed to enrich to ring structures around saddle-shaped membrane invaginations in dHL60s (**Fig 6C**). Additionally, because full-length IRSp53 recognized saddle curvature in dHL60 cells (**Fig 5**), we expected that full-length IRSp53 would also recognize TEMs, and our observations are consistent with this hypothesis (**Fig 6E-F**). These data further support our finding that IRSp53 depends on its ability to interact with the WAVE complex to localize to saddle geometries (**Fig 6G**).

Though membrane invaginations during F-actin inhibition and TEMs both display saddle curvature, they sometimes differ in scale: invaginations have diameters on the nanometer scale whereas TEMs have diameters ranging from microns to fractions of a micron. Based on the characteristic size of the WAVE complex rings in the absence of actin polymer in dHL60 cells and the rings formed by IRSp53 in the presence and absence of actin polymer (**Fig 5E**), we hypothesized that this represents the optimal membrane geometry for the WAVE complex enrichment, suggesting a preference for saddles with a negative curvature of lamellipodia-size, $\kappa \sim 1/65 \text{ nm}^{-1}$, and positive curvature, $\kappa \sim 1/135 \text{ nm}^{-1}$. An advantage of the TEMs saddle system is that it maintains a fixed lamellipodial-like negative curvature in the z-plane while it scans a range of positive curvatures throughout its closure. Therefore, we can use this range of hole sizes to evaluate the curvature

preference for the WAVE complex. Depending on the type of curvature sensor, the possible behaviors of a molecule's local concentration (signal per unit length) during TEM closure would be that it: increases, remains constant, or decreases (**Fig 7A**). A saddle geometry sensor presented with fixed negative curvature in one axis and a range of positive curvatures in the other axis would increase its local concentration until the TEM closure reaches the sensor's preferential positive curvature. From analyzing the WAVE complex signal throughout TEM closure, its local concentration per unit TEM perimeter increases at a rate significantly different from that of the membrane (**Fig. 7B-C**). As the imaging was performed with confocal microscopy, we are unable to resolve TEM diameters below the diffraction limit. However, the WAVE complex's progressive enrichment to smaller and smaller TEMs toward the diffraction limit is consistent with our initial finding that the WAVE complex spontaneously forms sub-diffraction ring structures (**Fig 2B-D**). These data suggest that the WAVE complex prefers nanoscale saddle geometry in a range of cellular and physiological contexts.

DISCUSSION

The WAVE complex assembles into a linear, curved oligomer at sites of saddle membrane curvature.

In this work, we investigated how the WAVE complex achieves the linear spatial organization that is essential for lamellipodial formation. We found that the WAVE complex assembles into highly ordered, linear oligomers in the form of nanoscale rings (**Fig 2**). These rings are formed in the absence of actin polymer and associate with regions of membrane saddle curvature (**Fig 2-3**). The WAVE complex's enrichment to membrane saddles is also apparent in the presence of actin polymer as it localizes to closing TEMs (**Fig 4, Fig 7**). IRSp53 requires its interactions with the WAVE complex to localize to lamellipodia, membrane invaginations, and TEMs (**Fig 5-6**). This finding highlights how proteins can partner together to sense complex geometries. The WAVE complex's association with saddle-shaped membrane coupled with its regulation of actin polymerization likely forms the basis for emergent self-organizing behaviors like cell morphogenesis during migration and closure of transcellular holes.

How the WAVE complex achieves its oligomeric association into stereotyped 270nm rings is unknown. There is no evidence that the WAVE complex oligomerizes on its own (63). It is likely that the WAVE complex requires its interacting partners to form higher-order oligomers; this is true for N-WASP (29,31). It is possible that the same proteins that activate the nucleation ability of the WAVE complex, such as phosphoinositides, Rac, and Arf (9), are also needed to activate its oligomerization. Furthermore, our observation that

the WAVE complex and IRSp53 collaborate to sense and form rings (**Fig 5-6**) suggest that IRSp53 may be a constituent of the rings.

Parallels with septin biology for oligomeric rings as curvature sensors.

The WAVE complex's oligomerization into rings may contribute to how it recognizes sites of membrane saddle geometry. Ring formation has been observed for other proteins capable of sensing membrane curvature. Septins form rings upon treatment of actin destabilizing drugs *in vivo* and purified septins form similarly-sized rings *in vitro* (64). The radius of curvature of septin rings reflects septins' intrinsic curvature preference both *in vitro* and *in vivo* (64,65). Like septins, the WAVE complex also forms ring structures upon actin depolymerization, and these rings associate with curved membranes (in the case of the WAVE complex sites of saddle curvature with a radius of positive curvature of 135nm). Thus, the geometry of the WAVE complex's nanoscale rings may predict the WAVE complex's preferred geometry. Consistent with this idea, the WAVE complex prefers membrane saddles with near-diffraction-limited curvature in the positive axis for closing transendothelial cell macroaperture tunnels (**Fig 7B-C**) and overexpression of IRSp53 generates similarly sized rings even in the presence of an intact actin cytoskeleton (**Fig 5C-E**).

What is the dimension of the WAVE complex rings in the negative curvature axis? Although we cannot visualize this directly in our TIRF-SIM images of F-actin inhibited cells (negative curvature axis is in the z plane where TIRF provides no information), our electron microscopy imaging of membrane invaginations gives a height estimate of

~130nm, which is consistent with the negative curvature of the edge of lamellipodia in our work (**S4D Fig**) and others' work (66–68), and consistent with the ~100nm resolution of TIRF-SIM imaging of propagating WAVE complex waves in non-latrunculin treated cells. The presence of IRSp53 in the rings and its partnering interactions with the WAVE complex would suggest the negative curvature axis is set by IRSp53, which has an intrinsic curvature of around 20nm in the negative axis and curvature sensing up to around 100nm (69). If protein oligomerization is setting the positive axis of curvature sensing, this could account for why the WAVE complex can tolerate a range of positive curvatures: from no curvature/flat (some portions of lamellipodia) across many microns (in large TEMs) up to the preferred curvature of diffraction-limited TEMs and nanoscale membrane invaginations (**Fig 2, 7**).

IRSp53 partners with the WAVE complex to recognize saddle geometry.

How does the WAVE complex recognize saddles? Saddle enrichment could be accomplished with one protein sensing the positive curvature and another sensing the negative curvature. The WAVE complex is not known to sense curvature on its own, but it interacts with IRSp53, a member of the nanoscale negative curvature sensing BAR domain family. By comparing full-length IRSp53 to its I-BAR only domain in dHL60s, HUVECs, and in WAVE complex depleted dHL60s, we clarified how IRSp53's localization is guided by its partnering interactions with the WAVE complex to enrich to lamellipodia and sites of saddle curvature (**Fig 6**). Others have also observed differences between full-length IRSp53 and its I-BAR only domain with super-resolution imaging. For example, with STORM imaging of filopodia in mouse neuroblastoma cells, IRSp53 localizes to the

lateral edges of filopodia, whereas its isolated I-BAR domain is uniformly distributed in filopodia (60). Our work highlights how proteins partner together for complex, saddle shape sensing. What about the WAVE complex and IRSp53 interaction enables IRSp53 to localize to lamellipodia and rings? The oligomeric arrangement of IRSp53 on its own may be different than that seen in conjunction with the WAVE complex. This merits future investigation.

Saddle curvature recognition of the WAVE complex may result in emergent behaviors, such as self-straightening lamellipodia and sealing of transcellular holes.

How are the WAVE complex's nanoscale rings related to its excitable dynamics during neutrophil migration? We interpret the WAVE complex rings that associate with saddle curvature to represent its preferred geometry of oligomerization, with a 135nm radius of curvature in the positive axis and around 65nm radius of curvature in the negative axis.

The coupling of saddle curvature recognition (cell shape) and patterning F-actin polymerization (physical forces) could result in a number of emergent behaviors. For example, if the WAVE complex both recognizes and generates sites of membrane saddle curvature, this could form a feedback loop that organizes the expansion and self-straightening of lamellipodia. Near the initiation of a lamellipodium, a small sheet-like membrane deformation has saddle curvature at its lateral edges (**Fig 8**). WAVE complex association with these saddles would result in a laterally expanding zone of actin nucleation, where the wave would grow at the sides but be confined to a small region at the tip of the lamellipodium based on the negative curvature sensing. This spatial

constraint on the positive feedback arm of the excitable actin nucleation circuit could explain why the domain of activation for this circuit is much thinner than other excitable circuits, such as cortical excitability in *Xenopus* (70) and Min protein oscillations for bacterial cell division (71).

Saddle enrichment would also enable maintenance of a uniform leading edge advancement — any regions of the lamellipodia that lag behind also display saddle curvature, resulting in flattening of the front (**Fig 3D-E, Fig 8**). If the lamellipodium requires a negatively curved edge, the flattening of this structure as it contacts a barrier could provide a geometric mechanism of barrier avoidance; the WAVE complex is known to extinguish at mechanical barriers (7). Finally, saddle recruitment of the WAVE complex could enable the recognition and actin-based sealing of transient endothelial macroapertures (46). Simple local rules of protein association could generate a number of the emergent features of cell shape and movement.

MATERIALS AND METHODS

Cell culture

All cells were cultured in a 37°C/5% CO₂ incubator.

HL60s - HL60 cells were cultured in RPMI-1640 with 25mM HEPES (Corning) with 10% (vol/vol) heat-inactivated fetal bovine serum (FBS; Gibco) and maintained at 0.2-1.0 x 10⁶ cells/mL. Cells were differentiated with 1.5% DMSO (Sigma-Aldrich) in growth media for 4-5 days prior to experiments. All imaging was done with differentiated HL60s (dHL60s) unless otherwise stated. Hem1-depleted HL60 cells were from (24).

HEK-293Ts - HEK-293T cells were used to generate lentivirus. 293Ts were cultured in DMEM (Gibco) with 10% FBS. Cells were cultured up to 80% confluency.

HUVECs – HUVEC cells were a kind gift from the MS Conte lab (University of California, San Francisco [UCSF]). HUVECs were cultured in HyClone M-199 media (GE Healthcare) with 1% antibiotics-antimicrobial (Gibco), 15.3 units of heparin (Sigma), 1 vial of endothelial cell growth supplement (EMD Millipore), and 10% FBS. Cells were cultured up to 80% confluency and growth media was replaced every other day. Experiments used cells with fewer than 10 passages.

B16F10 - B16F10 cells were cultured in DMEM (Gibco) with 10% FBS, 1% penicillin-streptomycin (Gibco), and 1% GlutaMax (Life Technologies). Cells were cultured up to 80% confluency.

U2OS - U2OS cells were a kind gift from the M von Zastrow lab (UCSF). U2OS cells were cultured in McCoy's 5A media (Gibco) with 10% FBS. Cells were cultured up to 80% confluency.

Plasmids

For stable expression, all constructs were cloned into the pHR lentiviral backbone (provided by the RD Vale lab, UCSF) with a SFFV promoter via standard Gibson assembly. The other WAVE complex subunit constructs (eGFP-Abi1, eGFP-Abi2, eGFP-Sra1, eGFP-Nap1, and eGFP-WAVE2) were a kind gift from the G Scita lab (European Institute of Oncology). IRSp53 was from the DNASU Plasmid Repository (pENTR223) and subsequently subcloned into a pHR vector. IRSp53¹⁻²⁵⁰ was "I-BAR," the N-terminal 250 amino acids, and IRSp53²⁵¹⁻⁵¹² was "C-term," the C-terminal 262 amino acids beyond the I-BAR domain. For all IRSp53 constructs, the eGFP was C-terminally tagged.

Cell line generation

Lentivirus

All HL60s and some HUVEC lines were stably expressing the constructs of interest. HEK-293Ts were plated in 6-well plates (Corning) until 70-80% confluency. Cells were transfected with 1.5µg of the pHR plasmid along with two plasmids containing the lentiviral packaging proteins (0.167µg of pMD2.G and 1.3µg of p8.91) with TransIT-293 (Mirus Bio). After 2-3 days of transfection, lentivirus-containing supernatant was collected, filtered with a 0.45µm filter (EMD Millipore), and concentrated 20x with Lenti-X

Concentrator (Takara). Lentivirus was used immediately or kept at -80°C. For HL60 transduction, 3.2×10^5 cells, 4µg/mL polybrene, and ~130µL of concentrated virus were incubated overnight. Cells were FACS sorted (BD Aria2). For eGFP-tagged IRSp53 structure-function constructs, cells were sorted for comparable fluorescence expression levels (**S6 Fig**). For HUVEC transduction, a 50% confluent 6-well was incubated with 4µg/mL polybrene, and ~130µL of 1x virus overnight.

Electroporation

For transient expression of plasmids in HUVEC cells, electroporation was used. For each electroporation condition, 50,000 cells were resuspended in 10µL of Buffer R (Thermo Scientific) with 500ng of DNA. Electroporations were performed with the Neon Transfection System (ThermoFisher) with 10µL tips at 1350V for 30ms for 1 pulse. Cells recovered in 500µL of culture media and imaged the next day.

Lipofectamine

For B16F10 and U2OS cell lines, plasmids were transiently expressed with Lipofectamine 2000 or 3000 (Invitrogen) per manufacturer's instructions.

Imaging

Cell preparation

HL60s

For imaging, differentiated cells were resuspended in imaging media (either Leibovitz's L-15 [Gibco] with 0.5% FBS or mHBSS [10x stock consists of 1500mM NaCl, 40mM KCl,

10mM MgCl₂, 12mM CaCl₂, 100mM glucose, 200mM HEPES, pH 7.2]). Cells were plated onto fibronectin coated wells (100 µg/mL for 1hr at room temperature) and incubated (37°C/5% CO₂) for at least 7 minutes before 2-3 washes with imaging media. For chemoattractant stimulation, a 2x stock of 20nM fMLP (Sigma) was added. For additional chemoattractant stimulation, a 2x stock of 200nM fMLP was added. For F-actin inhibition, a 2x stock of 1µM latrunculin B (EMD Millipore and Sigma) with 200nM phorbol 12-myristate 13-acetate (PMA; Sigma; for persistent Hem1 activation) was used, unless noted otherwise. Other F-actin inhibition drugs were latrunculin A (EMD Millipore) and cytochalasin B (Sigma). All initial stocks were dissolved in 100% dry DMSO and freshly diluted in imaging media before experiments.

HUVECs

To induce TEM formation, HUVECs were incubated in 50µM Y27632 (Tocris and Sigma) for at least 4 hours before imaging. Y27632 was present throughout imaging.

Membrane labeling

For membrane labeling, Vybrant DiD (Invitrogen) or CellMask Deep Red (Invitrogen) was freshly diluted (0.5-1X) in imaging media. HL60s were labeled in suspension for 30sec at 37°C and washed 2-3 times with imaging media. Adherent cell lines were labeled for 5min at 37°C and washed 3-5 times with phosphate buffered saline (PBS).

Fixation

Cells were plated in #1.5, 8-well Lab-Tek II chambers (Thermo Fisher Scientific). To fix cells, media was aspirated while simultaneously adding 200 μ L of 2% glutaraldehyde (Sigma-Aldrich) for 10min and washed with PBS for 30sec and 60sec. Aldehydes were quenched with 0.1% sodium borohydride (Sigma-Aldrich) for 7min and followed by 2-3 10min PBS washes. Samples were imaged immediately or stored at 4°C. All dilutions were prepared fresh in cytoskeleton buffer with sucrose (CBS), a TJ Mitchison lab (Harvard Medical School) recipe: 10mM MES pH 6.1, 138mM KCl, 3mM MgCl, 2mM EGTA, with 0.32M sucrose added fresh before use. HUVECs were fixed with 4% PFA in PBS, pH 7.4 instead of with 2% glutaraldehyde. All materials were warmed to 37°C.

Microscopes

TIRF-SIM

TIRF-SIM imaging was performed on DeltaVision OMX SR (GE Healthcare) with a 60x/1.42 numerical aperture (NA) oil Plan Apo objective (Olympus) with 1.516 or 1.518 refractive index oil (Cargille). HL60 experiments were performed at room temperature while adherent cells were performed at 37°C/5% CO₂. Images were processed with softWoRx (OMX SI Reconstruction with the default parameters including Wiener filter: 0.001; OMX Align Images with the Legacy Image Registration method). Display of TIRF-SIM membrane images were smoothed in Fiji.

Spinning disk confocal

Images were acquired on a Nikon Eclipse Ti microscope with a 60x/1.40 NA Plan Apo objective (Nikon), Yokogawa CSU-X1 spinning disk confocal, and a Prime 95B cMOS camera (Photometrics). 405, 488, 561, 640nm laser lines (Agilent Technologies) and environmental control (37°C/5% CO₂; Okolab) was used. Software was controlled with Nikon Elements.

Lattice light sheet and processing

Lattice-light sheet imaging was performed in a manner previously described (72) and followed an established protocol (73). Briefly, 5mm round coverslips (Warner Instruments) were cleaned by plasma cleaning and coated with fibronectin (100 µg/mL for 1hr). Cells were plated as described above. The coverslip sample was then loaded into a sample holder and placed into the previously conditioned microscope sample bath (with 25nM chemoattractant) and secured. Imaging was performed with a 488nm laser (MPBC). Camera exposure was 10ms per frame leading to a temporal resolution of 2.25 sec in single color mode.

Raw image files were deconvolved using the iterative Richardson-Lucy algorithm with the known point spread function for each channel, which were collected prior to each day of imaging (72). The code for this process was provided by the E Betzig lab (Janelia Research Campus) originally written in Matlab (The Mathworks) and ported into CUDA (Nvidia) for parallel processing on the graphics processing unit (GPU, Nvidia GeForce GTX Titan X). Each sample area underwent 15 iterations of deconvolution.

Regions of interest within the sampling were cropped down to size and compressed from 32-bit TIFFs to 16-bit TIFFs using in-house Matlab code to allow immigration into the 3D visualization software ChimeraX (UCSF Resource for Biocomputing, Visualization, and Informatics (74)). To highlight intensity ranges, additional channels were created by thresholding.

Transmission electron microscopy

Cells were prepared for convention EM in two ways: cells were either plated on fibronectin-coated ACLAR discs (TedPella), fixed with glutaraldehyde as described above and dehydrated or cells were plated on sapphire disks and fixed via high pressure freezing/freeze-substitution. For the glutaraldehyde fixation method, cells were treated with 100nM chemoattractant or 500nM latrunculin B for 5min, fixed, stained with uranyl acetate and OsO₄, dehydrated with cold ethanol, and embedded with Epon 812 resin. For the high pressure freezing/freeze-substitution method, cells were plated onto 3mm diameter sapphire disks and treated with 100nM chemoattractant or 500nM latrunculin B for 5min prior to freezing. The sapphire disk was then placed, cells toward the inside of a 100µm well specimen carriers (Type A, Technotrade International Inc) containing 20% (bovine serum albumin) BSA in growth media. The sandwiched cells were frozen using a BalTec HPM 01 high pressure freezer (BalTec). Freeze-substitution in 1% OsO₄, 0.1% uranyl acetate, 1% methanol in acetone, containing 3% water (75,76) was carried out with a Leica AFS2 unit. Following substitution, samples were rinsed in acetone, infiltrated and then polymerized in Eponate 12 resin (Ted Pella). For conventional electron microscopy,

serial 50nm sections were cut with a Leica UCT ultramicrotome using a Diatome diamond knife, picked up on Pioloform coated slot grids and stained with uranyl acetate and Sato's lead (77). Sections were imaged with a FEI Tecnai T12 TEM at 120 kV using a Gatan 2k x 2k camera. For EM tomography, 200nm sections were cut, mounted on grids and stained as above for serial thin sections. Tomograms were acquired using an FEI T20 TEM at 200 kV, and tomograms reconstructed using eTomo/IMOD (78,79).

Image analysis and statistics

All image analysis was performed in Fiji and/or Python. Data handling and statistical tests were performed with Python and Prism 8 (GraphPad).

Diameter calculation

After background subtraction (rolling ball), segmentation was performed with Trainable Weka Segmentation (80) machine learning algorithm to identify ring structures. The diameter of a perfect circle with the same perimeter of the ring particle was calculated (diameter = C/π ; C=circumference).

Membrane curvature and velocity

Fluorescence images were segmented using a 3-step process consisting of Gaussian smoothing, intensity-based thresholding, and binary erosion. The threshold and degree of erosion were chosen manually to align the boundary of the binary image with the apparent edge of the cell membrane. To facilitate temporal analysis of edge properties, these boundaries were then fit using a spline interpolation consisting of 1,000 points.

Edge velocity at a particular point, P, at time, t, was estimated by calculating the average of the distance transforms of the binary images at times t-1 and t+1 and interpolating the value of this function at the coordinates of P. The radius of curvature at a point, P, was calculated by approximating the radius of the osculating circle, C, along the boundary at the coordinates of P. To approximate this osculating circle, we chose a scale parameter, S, then collected the coordinates of the two points at indices S units away from P. Given these three points, a unique equation of a circle passing through them was calculated. A sign was assigned by comparing the vector between P and the center of circle C and the normal vector of the boundary.

EM curvature

After identifying the plasma membrane, a perfect circle was fitted to both sides of the neck of an invagination and at the tip of a protrusion. Curvature, κ , was defined as $\kappa = 1/R$ (R = radius).

IRSp53 and Hem1 colocalization

Images were background subtracted (rolling ball) and Fiji's coloc2 function was applied with the segmented images and an ROI of the combined masks.

IRSp53 lamellipodia/filopodia enrichment

After background subtraction (rolling ball), two masks were generated: a lamellipodia mask was created from Hem1 signal and a filopodia mask was created from the eroded regions of a cell mask. After subtracting the cytosolic background from each segment

(cytosolic intensity per unit area multiplied by the segment's area), the intensity per unit area of each segment was calculated, i.e. lamellipodia signal/lamellipodia area. The ratio of the lamellipodia to the filopodia intensities per unit areas was graphed.

IRSp53 structure function ring enrichment

After background subtraction (rolling ball), a ring mask was generated from segmenting Hem1 signal and a background mask was generated by dilating the ring mask. IRSp53 signal was measured from both masks. After background correction (subtracting the background intensity per unit area multiplied by the ring mask area), the enrichment factor was calculated as the ratio of the ring to the background intensities per unit areas. Enrichment of all rings within a cell was averaged and treated as an individual data point.

TEMs enrichment

TEMs were identified by segmenting the membrane channel (TEM mask). The signal mask was generated by dilating the TEM mask by 2-3 pixels and the background mask was generated by dilating the signal mask by 2-3 pixels. A doughnut-shaped signal segment was calculated by subtracting the TEM mask from the signal mask and a doughnut-shaped background segment was calculated by subtracting the signal mask from the background mask. The doughnut-shaped signal segment was background corrected (subtracting the background intensity per unit area multiplied by the signal mask area). The enrichment factor was measured as the ratio of the signal to background intensities per unit areas. The intensity per unit perimeter was calculated as the background-corrected signal intensity divided by the signal perimeter.

ACKNOWLEDGEMENTS

We thank the members of the Weiner lab for many conversations and support throughout the project. We want to acknowledge Wallace Marshall, Sophie Dumont, Ron Vale, Adam Frost, and Nir Gov for their helpful discussions. We thank Jessica Sherry, Kirstin Meyer, and Brian Graziano for critical reading of the manuscript. We thank DeLaine Larsen and Kari Herrington of the UCSF Imaging Core as well as Chris Rieken, Galo Garcia, David Castaneda-Castellanos, and Yina Wang for their microscopy expertise. We also thank Richard Fetter and the staff at the University of California Berkeley Electron Microscope Laboratory for advice and assistance in electron microscopy sample preparation and data collection. This work was supported by an AHA Predoctoral Fellowship (AP), NIH F31 HL143882 (RMB), NSF Predoctoral Fellowships (JPT, NTT), NIH GM118167 (ODW), the NSF Center for Cellular Construction (DBI-1548297), and a Novo Nordisk Foundation grant for the Center for Geometrically Engineered Cellular Systems (NNF17OC0028176). The UCSF Imaging Core was supported by the Research Evaluation and Allocation Committee (REAC), the Gross Fund, and the Heart Anonymous Fund. The FACS work was supported in part by the HDFCCC Laboratory for Cell Analysis Shared Resource Facility through a grant from the NIH (P30CA082103).

REFERENCES

1. Takenawa T, Suetsugu S. The WASP-WAVE protein network: Connecting the membrane to the cytoskeleton. *Nat Rev Mol Cell Biol.* 2007;8(1):37–48.
2. Chesarone MA, Goode BL. Actin nucleation and elongation factors: mechanisms and interplay. *Curr Opin Cell Biol.* 2009;21(1):28–37.
3. Machesky LM, Insall RH. Scar1 and the related Wiskott-Aldrich syndrome protein, WASP, regulate the actin cytoskeleton through the Arp2/3 complex. *Curr Biol.* 1998;8(25):1347–56.
4. Pollard TD, Borisy GG. Cellular Motility Driven by Assembly and Disassembly of Actin Filaments. *Cell.* 2003;112(4):453–65.
5. Rohatgi R, Ma L, Miki H, Lopez M, Kirchhausen T, Takenawa T, et al. N-WASP activates the Arp2/3 complex and links Cdc42 and phosphoinositide signals to actin assembly. *Mol Biol Cell.* 1999;10(S):122A.
6. Oikawa T, Yamaguchi H, Itoh T, Kato M, Ijuin T, Yamazaki D, et al. PtdIns(3,4,5)P₃ binding is necessary for WAVE2-induced formation of lamellipodia. *Nat Cell Biol.* 2004;6(5):420–6.
7. Weiner OD, Marganski WA, Wu LF, Altschuler SJ, Kirschner MW. An actin-based wave generator organizes cell motility. *PLoS Biol.* 2007;5(9):2053–63.
8. Ho H-Y, Ma L, Li JX, Rohatgi R, Lebensohn A, Ma J Le, et al. Toca-1 mediates Cdc42-dependent actin nucleation by activating the N-WASP-WIP complex. *Cell.* 2004;118(2):203–16.
9. Koronakis V, Hume PJ, Humphreys D, Liu T, Hørning O, Jensen ON, et al. WAVE regulatory complex activation by cooperating GTPases Arf and Rac1. *Proc Natl*

- Acad Sci U S A. 2011;108(35):14449–54.
10. Suetsugu S, Kurisu S, Oikawa T, Yamazaki D, Oda A, Takenawa T. Optimization of WAVE2 complex-induced actin polymerization by membrane-bound IRSp53, PIP3, and Rac. *J Cell Biol.* 2006;173(4):571–85.
 11. Abou-Kheir W, Isaac B, Yamaguchi H, Cox D. Membrane targeting of WAVE2 is not sufficient for WAVE2-dependent actin polymerization: A role for IRSp53 in mediating the interaction between Rac and WAVE2. *J Cell Sci.* 2008;121(3):379–90.
 12. Miki H, Sasaki T, Takai Y, Takenawa T. Induction of filopodium formation by a WASP-related actin- depolymerizing protein N-WASP. *Nature.* 1998;391(6662):93–6.
 13. Bu W, Chou AM, Lim KB, Sudhaharan T, Ahmed S. The Toca-1-N-WASP complex links filopodial formation to endocytosis. *J Biol Chem.* 2009;284(17):11622–36.
 14. Naqvi SN, Zahn R, Mitchell DA, Stevenson BJ, Munn AL. The WASp homologue Las17p functions with the WIP homologue End5p / verprolin and is essential for endocytosis in yeast. *Curr Biol.* 1998;8:959–62.
 15. Yamaguchi H, Lorenz M, Kempiak S, Sarmiento C, Coniglio S, Symons M, et al. Molecular mechanisms of invadopodium formation: The role of the N-WASP-Arp2/3 complex pathway and cofilin. *J Cell Biol.* 2005;168(3):441–52.
 16. Yu X, Machesky LM. Cells assemble invadopodia-like structures and invade into matrigel in a matrix metalloprotease dependent manner in the circular invasion assay. *PLoS One.* 2012;7(2).

17. Yu X, Zech T, McDonald L, Gonzalez EG, Li A, Macpherson I, et al. N-WASP coordinates the delivery and F-actin-mediated capture of MT1-MMP at invasive pseudopods. *J Cell Biol.* 2012;199(3):527–44.
18. Benesch S, Polo S, Lai FP, Anderson KI, Stradal TEB, Wehland J, et al. N-WASP deficiency impairs EGF internalization and actin assembly at clathrin-coated pits. *J Cell Sci.* 2005;118(14):3103–15.
19. Taylor MJ, Perrais D, Merrifield CJ. A high precision survey of the molecular dynamics of mammalian clathrin-mediated endocytosis. *PLoS Biol.* 2011;9(3).
20. Veltman DM, King JS, Machesky LM, Insall RH. SCAR knockouts in *Dictyostelium*: WASP assumes SCAR's position and upstream regulators in pseudopods. *J Cell Biol.* 2012;198(4):501–8.
21. Hall A. Rho GTPases and the actin cytoskeleton. *Science* (80-). 1998;279(5350):509–14.
22. Weiner OD, Rentel MC, Ott A, Brown GE, Jedrychowski M, Yaffe MB, et al. Hem-1 complexes are essential for Rac activation, actin polymerization, and myosin regulation during neutrophil chemotaxis. *PLoS Biol.* 2006;4(2):186–99.
23. Leithner A, Eichner A, Müller J, Reversat A, Brown M, Schwarz J, et al. Diversified actin protrusions promote environmental exploration but are dispensable for locomotion of leukocytes. *Nat Cell Biol.* 2016;18(11):1253–9.
24. Graziano BR, Town JP, Nagy TL, Fošnarič M, Penič S, Igljič A, et al. Cell confinement reveals a branched-actin independent circuit for neutrophil polarity. *PLoS Biology.* 2019. e3000457 p.
25. Liu AP, Richmond DL, Maibaum L, Pronk S, Geissler PL, Fletcher DA.

- Membrane-induced bundling of actinfilaments. *Nat Phys.* 2008;4(10):789–93.
26. Carlier MF, Le Clainche C, Wiesner S, Pantaloni D. Actin-based motility: From molecules to movement. *BioEssays.* 2003;25(4):336–45.
 27. Boujemaa-Paterski R, Suarez C, Klar T, Zhu J, Guérin C, Mogilner A, et al. Network heterogeneity regulates steering in actin-based motility. *Nat Commun.* 2017;8(1):1–12.
 28. Lillian K Fritz-Laylin, Megan Riel-Mehan, Bi-Chang Chen, Samuel J Lord, Thomas D Goddard, Thomas E Ferrin SMN-D, Henry Higgs, Graham T Johnson, Eric Betzig RDM. Actin-based protrusions of migrating neutrophils are intrinsically lamellar and facilitate direction changes. *Elife.* 2017;6(e26990).
 29. Case LB, Zhang X, Ditlev JA, Rosen MK. Stoichiometry controls activity of phase-separated clusters of actin signaling proteins. *Science (80-).* 2019;363(6431):1093–7.
 30. Fritz-Laylin LK, Lord SJ, Mullins RD. WASP and SCAR are evolutionarily conserved in actin-filled pseudopod-based motility. *J Cell Biol.* 2017;216(6):1673–88.
 31. Banjade S, Rosen MK. Phase transitions of multivalent proteins can promote clustering of membrane receptors. *Elife.* 2014;3:1–24.
 32. Ibarra N, Blagg SL, Vazquez F, Insall RH. Nap1 Regulates Dictyostelium Cell Motility and Adhesion through SCAR-Dependent and -Independent Pathways. *Curr Biol.* 2006;16(7):717–22.
 33. Szymanski DB. Breaking the WAVE complex: The point of Arabidopsis trichomes. *Curr Opin Plant Biol.* 2005;8(1):103–12.

34. Rakeman AS, Anderson K V. Axis specification and morphogenesis in the mouse embryo require Nap1, a regulator of WAVE-mediated actin branching. *Development*. 2006;133(16):3075–83.
35. Eden S, Rohatgi R, Podtelejnikov A V., Mann M, Kirschner MW. Mechanism of regulation of WAVE1-induced actin nucleation by Rac1 and Nck. *Nature*. 2002;418(6899):790–3.
36. Innocenti M, Zucconi A, Disanza A, Frittoli E, Areces LB, Steffen A, et al. Abi1 is essential for the formation and activation of a WAVE2 signalling complex. *Nat Cell Biol*. 2004;6(4):319–27.
37. Park H, Staehling-Hampton K, Appleby MW, Brunkow ME, Habib T, Zhang Y, et al. A point mutation in the murine Heml gene reveals an essential role for Hematopoietic Protein 1 in lymphopoiesis and innate immunity. *J Exp Med*. 2008;205(12):2899–913.
38. Evans IR, Ghai PA, Urbančič V, Tan KL, Wood W. SCAR/WAVE-mediated processing of engulfed apoptotic corpses is essential for effective macrophage migration in *Drosophila*. *Cell Death Differ*. 2013;20(5):709–20.
39. Kheir WA, Gevrey JC, Yamaguchi H, Isaac B, Cox D. A WAVE2-Abi1 complex mediates CSF-1-induced F-actin-rich membrane protrusions and migration in macrophages. *J Cell Sci*. 2005;118(22):5369–79.
40. Carman C V., Springer TA. Trans-cellular migration: cell-cell contacts get intimate. *Curr Opin Cell Biol*. 2008;20(5):533–40.
41. Simunovic M, Voth GA, Callan-Jones A, Bassereau P. When Physics Takes Over: BAR Proteins and Membrane Curvature. *Trends Cell Biol* [Internet].

- 2015;25(12):780–92. Available from: <http://dx.doi.org/10.1016/j.tcb.2015.09.005>
42. Millius A, Watanabe N, Weiner OD. Diffusion, capture and recycling of SCAR/WAVE and Arp2/3 complexes observed in cells by singlemolecule imaging. *J Cell Sci.* 2012;125(5):1165–76.
 43. Allard J, Mogilner A. Traveling waves in actin dynamics and cell motility. *Curr Opin Cell Biol.* 2013;25(1):107–15.
 44. Diz-Muñoz A, Thurley K, Chintamen S, Altschuler SJ, Wu LF, Fletcher DA, et al. Membrane Tension Acts Through PLD2 and mTORC2 to Limit Actin Network Assembly During Neutrophil Migration. *PLoS Biol.* 2016;14(6):1–30.
 45. Carman C V., Sage PT, Sciuto TE, de la Fuente MA, Geha RS, Ochs HDD, et al. Transcellular Diapedesis Is Initiated by Invasive Podosomes. *Immunity.* 2007;26(6):784–97.
 46. Maddugoda MP, Stefani C, Gonzalez-Rodriguez D, Saarikangas J, Torrino S, Janel S, et al. CAMP signaling by Anthrax edema toxin induces transendothelial cell tunnels, which Are resealed by MIM via Arp2/3-Driven actin polymerization. *Cell Host Microbe.* 2011;10(5):464–74.
 47. Boyer L, Doye A, Rolando M, Flatau G, Munro P, Gounon P, et al. Induction of transient macroapertures in endothelial cells through RhoA inhibition by *Staphylococcus aureus* factors. *J Cell Biol.* 2006;173(5):809–19.
 48. Lemichez E, Lecuit M, Nassif X, Bourdoulous S. Breaking the wall: Targeting of the endothelium by pathogenic bacteria. *Nat Rev Microbiol.* 2010;8(2):93–104.
 49. Ng WP, Webster KD, Stefani C, Schmid EM, Lemichez E, Bassereau P, et al. Force-induced transcellular tunnel formation in endothelial cells. *Mol Biol Cell.*

- 2017;28(20):2650–60.
50. Stefani C, Gonzalez-Rodriguez D, Senju Y, Doye A, Efimova N, Janel S, et al. Ezrin enhances line tension along transcellular tunnel edges via NMIIa driven actomyosin cable formation. *Nat Commun.* 2017;8.
 51. Miki H, Yamaguchi H, Suetsugu S, Takenawa T. IRSp53 is an essential intermediate between Rac and WAVE in the regulation of membrane ruffling. *Nature.* 2000;408(6813):732–5.
 52. Scita G, Confalonieri S, Lappalainen P, Suetsugu S. IRSp53: crossing the road of membrane and actin dynamics in the formation of membrane protrusions. *Trends Cell Biol.* 2008;18(2):52–60.
 53. Frost A, Unger VM, De Camilli P. The BAR Domain Superfamily: Membrane-Molding Macromolecules. *Cell.* 2009;137(2):191–6.
 54. Zhao H, Pykäläinen A, Lappalainen P. I-BAR domain proteins: Linking actin and plasma membrane dynamics. *Curr Opin Cell Biol.* 2011;23(1):14–21.
 55. Mattila PK, Pykäläinen A, Saarikangas J, Paavilainen VO, Vihinen H, Jokitalo E, et al. Missing-in-metastasis and IRSp53 deform PI(4,5)P₂-rich membranes by an inverse BAR domain-like mechanism. *J Cell Biol.* 2007;176(7):953–64.
 56. Goh WI, Lim KB, Sudhaharan T, Sem KP, Bu W, Chou AM, et al. mDia1 and WAVE2 proteins interact directly with IRSp53 in filopodia and are involved in filopodium formation. *J Biol Chem.* 2012;287(7):4702–14.
 57. Nakagawa H, Miki H, Nozumi M, Takenawa T, Miyamoto S, Wehland J, et al. IRSp53 is colocalised with WAVE2 at the tips of protruding lamellipodia and filopodia independently of Mena. *J Cell Sci.* 2003;116(12):2577–83.

58. Robens JM, Yeow-Fong L, Ng E, Hall C, Manser E. Regulation of IRSp53-Dependent Filopodial Dynamics by Antagonism between 14-3-3 Binding and SH3-Mediated Localization. *Mol Cell Biol.* 2010;30(3):829–44.
59. Krugmann S, Jordens I, Gevaert K, Driessens M, Vandekerckhove J, Hall A. Cdc42 induces filopodia by promoting the formation of an IRSp53:Mena complex. *Curr Biol.* 2001;11(21):1645–55.
60. Sudhaharan T, Hariharan S, Lim JSY, Liu JZ, Koon YL, Wright GD, et al. Superresolution microscopy reveals distinct localisation of full length IRSp53 and its I-BAR domain protein within filopodia. *Sci Rep.* 2019;9(1):1–17.
61. Disanza A, Mantoani S, Hertzog M, Gerboth S, Frittoli E, Steffen A, et al. Regulation of cell shape by Cdc42 is mediated by the synergic actin-bundling activity of the Eps8 – IRSp53 complex. 2006;8(12).
62. Litschko C, Linkner J, Brühmann S, Stradal TEB, Reinl T, Jänsch L, et al. Differential functions of WAVE regulatory complex subunits in the regulation of actin-driven processes. *Eur J Cell Biol.* 2017;96(8):715–27.
63. Chen Z, Borek D, Padrick SB, Gomez TS, Metlagel Z, Ismail AM, et al. Structure and control of the actin regulatory WAVE complex. *Nature.* 2010;468(7323):533–8.
64. Kinoshita M, Field CM, Coughlin ML, Straight AF, Mitchison TJ. Self- and actin-templated assembly of mammalian septins. *Dev Cell.* 2002;3(6):791–802.
65. Bridges AA, Jentsch MS, Oakes PW, Occhipinti P, Gladfelter AS. Micron-scale plasma membrane curvature is recognized by the septin cytoskeleton. *J Cell Biol.* 2016;213(1):23–32.

66. Abercrombie M, Heaysman JEM, Pegrum SM. The locomotion of fibroblasts in culture. III. Movements of particles on the dorsal surface of the leading lamella. *Exp Cell Res.* 1970;62(2–3):389–98.
67. Abraham VC, Krishnamurthi V, Lansing Taylor D, Lanni F. The actin-based nanomachine at the leading edge of migrating cells. *Biophys J* [Internet]. 1999;77(3):1721–32. Available from: [http://dx.doi.org/10.1016/S0006-3495\(99\)77018-9](http://dx.doi.org/10.1016/S0006-3495(99)77018-9)
68. Urban E, Jacob S, Nemethova M, Resch GP, Small JV. Electron tomography reveals unbranched networks of actin filaments in lamellipodia. *Nat Cell Biol* [Internet]. 2010;12(5):429–35. Available from: <http://dx.doi.org/10.1038/ncb2044>
69. Prévost C, Zhao H, Manzi J, Lemichez E, Lappalainen P, Callan-Jones A, et al. IRSp53 senses negative membrane curvature and phase separates along membrane tubules. *Nat Commun.* 2015;6.
70. Bement WM, Leda M, Moe AM, Kita AM, Larson ME, Golding AE, et al. Activator-inhibitor coupling between Rho signaling and actin assembly make the cell cortex an excitable medium. *Nat Cell Biol.* 2016;17(11):1471–83.
71. Loose M, Fischer-friedrich E, Ries J, Kruse K, Schwille P. Spatial Regulators for Bacterial Cell. *Science.* 2008;320(May):789–92.
72. Chen BC, Legant WR, Wang K, Shao L, Milkie DE, Davidson MW, et al. Lattice light-sheet microscopy: Imaging molecules to embryos at high spatiotemporal resolution. *Science* (80-). 2014;346(6208).
73. Cai E, Marchuk K, Beemiller P, Beppler C, Rubashkin MG, Weaver VM, et al. Visualizing dynamic microvillar search and stabilization during ligand detection by

- T cells. *Science* (80-). 2017;356(6338).
74. Goddard TD, Huang CC, Meng EC, Pettersen EF, Couch GS, Morris JH, et al. UCSF ChimeraX: Meeting modern challenges in visualization and analysis. *Protein Sci.* 2018;27(1):14–25.
 75. Buser C, Walther P. Freeze-substitution: The addition of water to polar solvents enhances the retention of structure and acts at temperatures around -60°C. *J Microsc.* 2008;230(2):268–77.
 76. Walther P, Ziegler A. Freeze substitution of high-pressure frozen samples: The visibility of biological membranes is improved when the substitution medium contains water. *J Microsc.* 2002;208(1):3–10.
 77. T S. A modified method for lead staining of thin sections. *J Electron Microsc.* 1968;7(17):158–9.
 78. Kremer JR, Mastronarde DN, McIntosh JR. Computer visualization of three-dimensional image data using IMOD. *J Struct Biol.* 1996;116(1):71–6.
 79. Mastronarde DN. Dual-axis tomography: An approach with alignment methods that preserve resolution. *J Struct Biol.* 1997;120(3):343–52.
 80. Arganda-Carreras I, Kaynig V, Rueden C, Eliceiri KW, Schindelin J, Cardona A, et al. Trainable Weka Segmentation: A machine learning tool for microscopy pixel classification. *Bioinformatics.* 2017;33(15):2424–6.
 81. Genuth MA, Allen CDC, Mikawa T, Weiner OD. Chick cranial neural crest cells use progressive polarity refinement, not contact inhibition of locomotion, to guide their migration. *Dev Biol.* 2018;444:S252–61.

FIGURE 3.1

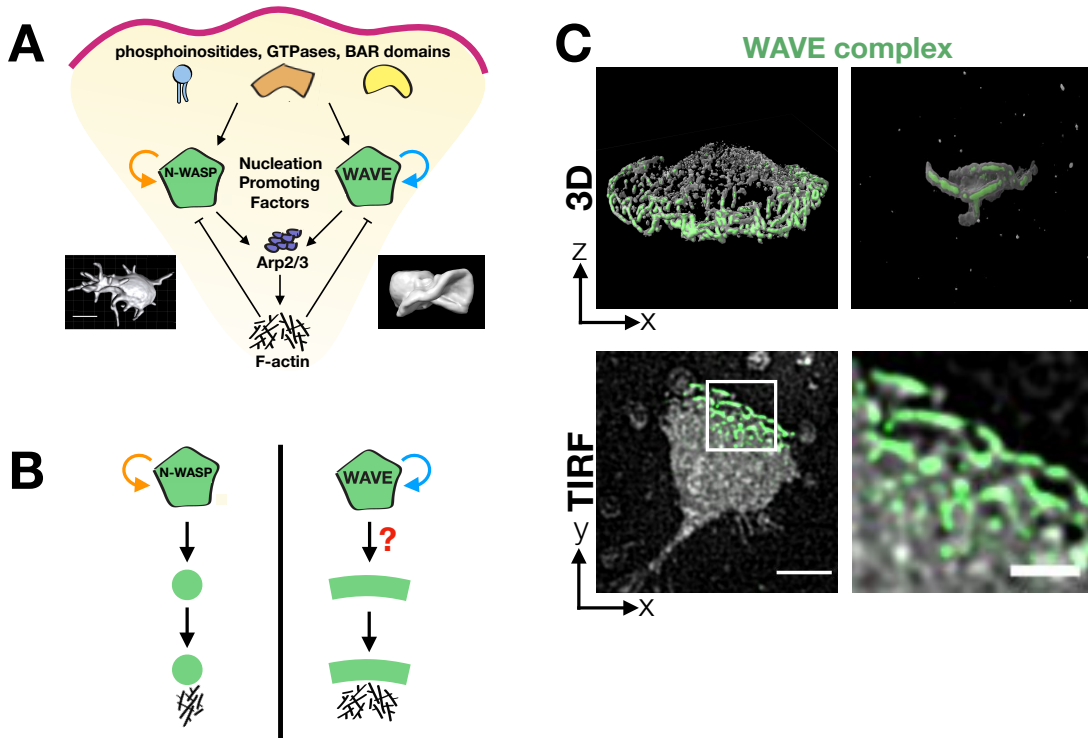


FIGURE 3.1. How does the WAVE complex achieve the linear spatial organization essential for lamellipodial generation?

(A) Similar actin nucleation-promoting factors (NPFs) organize different cell morphologies. Given that the homologous NPFs WAVE complex and N-WASP are embedded in similar signaling cascades, how do they spatially organize different cellular morphologies? N-WASP canonically associates with filopodia, invadopodia, and endocytosis whereas the WAVE complex associates with lamellipodia. Images: left, chick cranial neural crest cell with multiple filopodia from (81) and right, head-on view of a neutrophil-like dHL60 lamellipodium (ChimeraX rendering of a confocal z-stack).

(B) Schematic of how the NPF's spatial organization could instruct the resulting actin morphologies. N-WASP's positive feedback results in the focal organization expected for 1-dimensional finger-like actin structures. In order to build lamellipodia, does the WAVE complex's positive feedback result in a linear organization to template 2-dimensional sheet-like actin structures?

(C) Hem1-eGFP, a fluorescently tagged subunit of the WAVE complex, has a linear organization at tips of lamellipodia when dHL60 cells are stimulated with chemoattractant (10nM fMLP). Top: 3D imaging of the WAVE complex at tips of extending lamellipodia; left, widefield 3D reconstruction and right, lattice light sheet reconstruction of ruffles from a head-on view; see **S1 Video**. Bottom: WAVE complex's linear organization viewed from the basal plasma membrane; simultaneous TIRF imaging of Hem1-eGFP (green) and membrane CellMask DeepRed dye (gray); see **S2 Video**. Scale bars: 5 μ m (left) and 2 μ m (right).

FIGURE 3.2

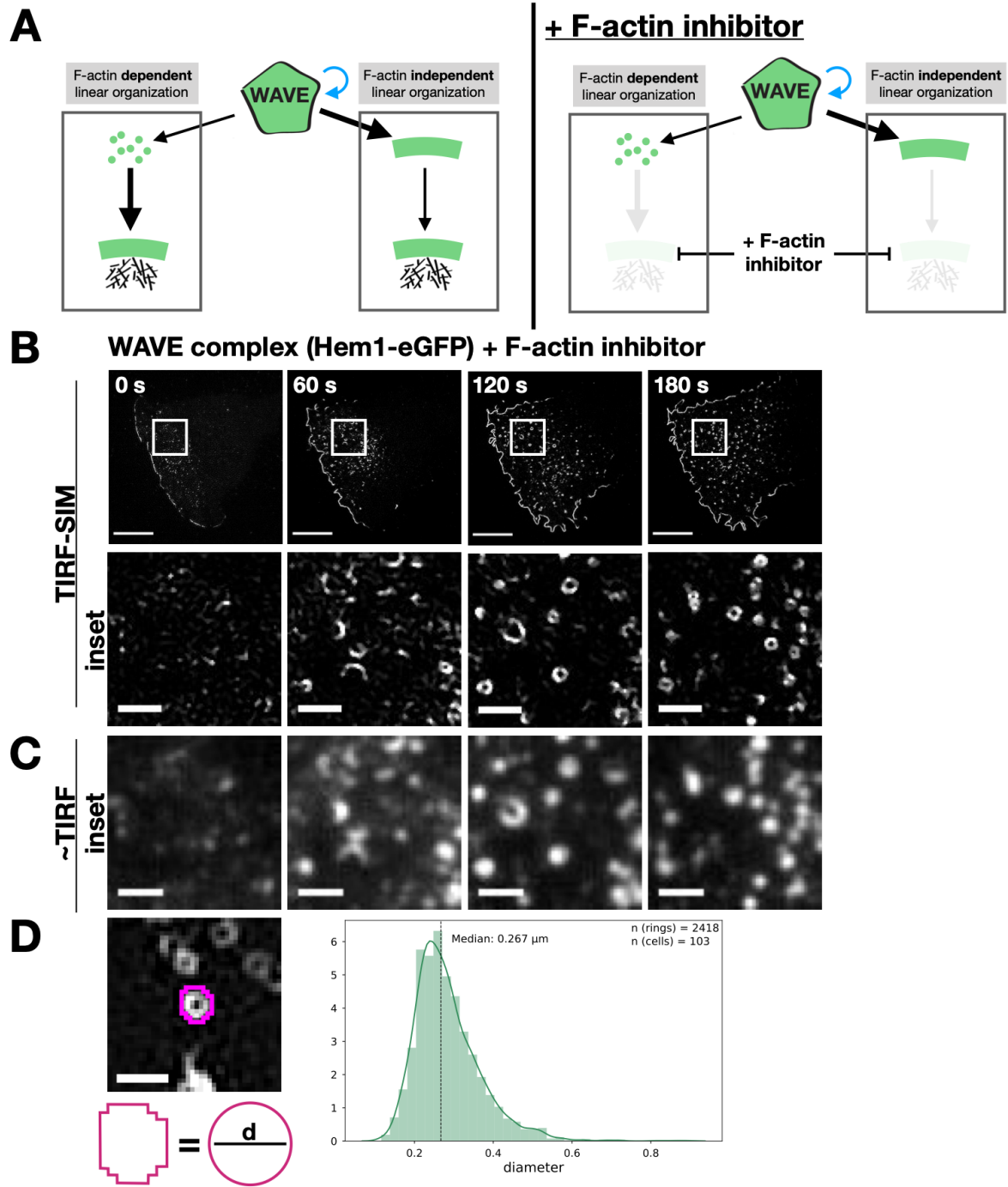


FIGURE 3.2. WAVE complex organizes as nanoscale rings in the absence of the actin cytoskeleton

(A) Models of the basis of the WAVE complex linear organization and the experimental design to distinguish the models. Left: the WAVE complex could achieve its linear organization at the lamellipodial edge in a manner that is dependent on its interactions with the actin cytoskeleton (left) or that is established independent of the actin cytoskeleton (right). Right: addition of a F-actin inhibitor can be used to distinguish these models.

(B) Super-resolution total internal reflection fluorescence structured illumination microscopy (TIRF-SIM) imaging reveals that the WAVE complex forms ring structures in the absence of actin polymers. dHL60 cells expressing Hem1-eGFP were acutely stimulated with latrunculin A (5 μ M final); see **S3 Video**. Bottom row are the white insets. Time in seconds; scale bars: 5 μ m (top) and 1 μ m (insets).

(C) Conventional TIRF resolution comparison highlights the need for super-resolution microscopy to resolve diffraction-limited WAVE complex puncta as rings. Conventional resolution TIRF images were created by sum-projecting the 9 images (3 phases * 3 angles) that construct TIRF-SIM images of **(B)**; see **S4 Video**. Scale bar: 1 μ m.

(D) The median diameter of the WAVE complex ring structures is 267 nanometers. Left, example measurement of fitting the ring's perimeter to a perfect circle and calculating the circle's diameter, d . Right, histogram of diameters of rings across a range of F-actin inhibiting drugs and concentrations of $n = 2418$ rings from 103 cells; see **S2 Fig**.

FIGURE 3.3

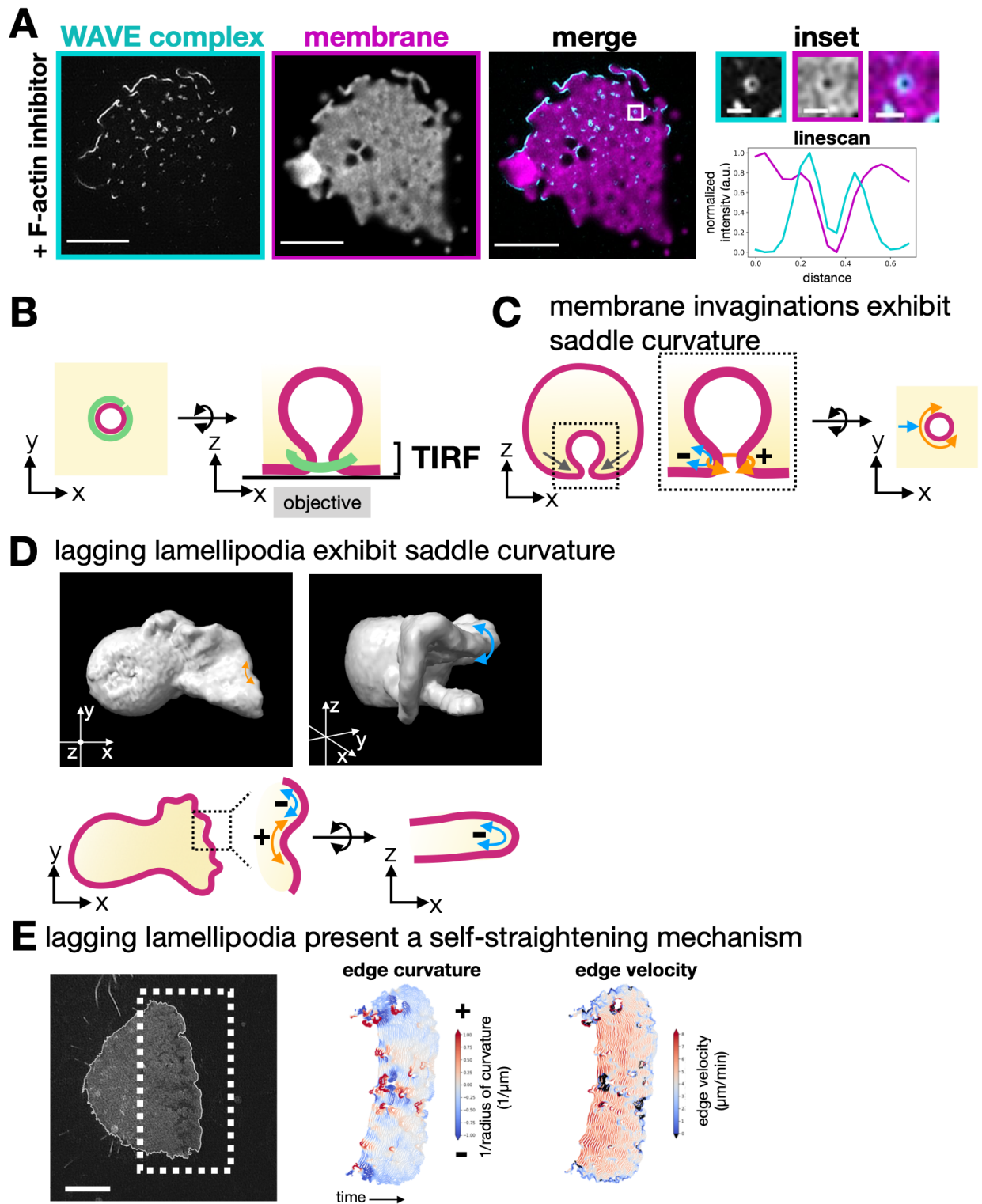


FIGURE 3.3. WAVE complex rings associate with membrane saddle points

(A) TIRF-SIM imaging of the WAVE complex (Hem1-eGFP; cyan) reveals rings localized at the boundary of where the plasma membrane (DiD-labeled membrane; magenta) exits the TIRF plane; see **S5 Video**. This membrane organization suggests enrichment to the necks of membrane invaginations. Right, graph of a linescan across a ring. Scale bars: 5 μ m and 500nm (inset).

(B) Schematic of proposed organization of the WAVE complex ring structure (green) around the neck of a membrane invagination (magenta) as seen from the top, XY plane (left), or the side, XZ plane (right).

(C) Schematic of a membrane invagination's saddle curvature. The necks of invaginations display saddle geometry of positive (orange; the curve around the invagination neck) and negative (blue; the curve perpendicular to the invagination neck) curvatures.

(D) Lagging portions of lamellipodia display saddle geometry. Top: ChimeraX rendering of a confocal z-stack membrane-bound marker in dHL60s. Top left: view of the top of the cell shows lagging portions of a lamellipodium extension. Top right: tilted orthogonal view highlights the negative curvature and sheet-like morphology of the lamellipodium. Bottom: schematic of curvatures of a lamellipodium.

(E) Lagging lamellipodia present a self-straightening mechanism. Left: TIRF-SIM image of membrane signal with its membrane edge outlined. Scale bar: 5 μ m. Middle: curvature analysis of the advancing front edge over time (1 frame every 2 seconds). Cool-warm scale indicates negative-positive curvature. Right: velocity analysis of the advancing front edge over time. Areas of positive curvature that become less positive, i.e. self-straighten, are associated with areas of increasing velocity.

FIGURE 3.4

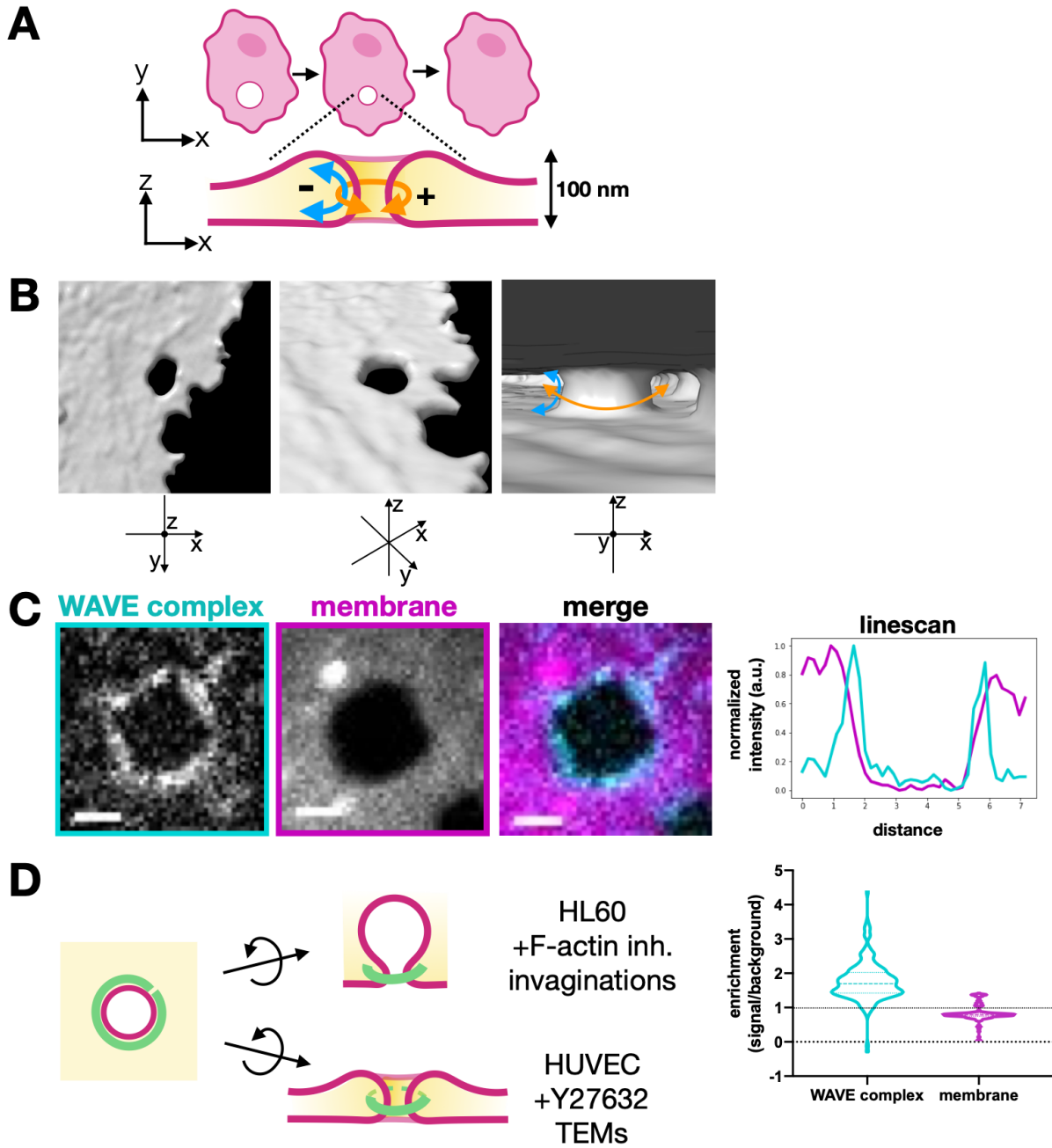


FIGURE 3.4. WAVE complex enriches to transendothelial cell macroaperture (TEM) tunnel saddle points

(A) Schematic of TEM closure and its saddle geometry.

(B) ChimeraX rendering of spinning disk confocal imaging of a fixed HUVEC cell treated with Y27632 (50 μ M) and labeled with a membrane dye (CellMask DeepRed). Middle: tilted view. Right: view from inside the cell facing a TEM and its saddle geometry. See **S6 Video**.

(C) HUVEC cells expressing eGFP-tagged Nap1, a WAVE complex subunit, and stained with membrane dye CellMask DeepRed show the WAVE complex localized at a TEM. Spinning disk confocal imaging, scale bar: 2 μ m. Top graph: linescan across the TEM; WAVE complex (cyan) and membrane dye (magenta). Bottom graph: violin plot of enrichment, which was measured as the ratio between the signal intensity per unit area at the TEMs compared to the background intensity per unit area. A value of 1 indicates no enrichment at the TEMs (dotted line), and a value above 1 indicates enrichment. Each time point throughout TEM closure was considered a single data point; WAVE complex and membrane both had n = 178 (from 6 TEMs) from at least 3 independent experiments per condition.

(D) Schematic showing the WAVE complex localization to saddle geometries of membrane invaginations in F-actin-inhibited dHL60s as well as TEMs in Y27632-treated HUVECs.

FIGURE 3.5

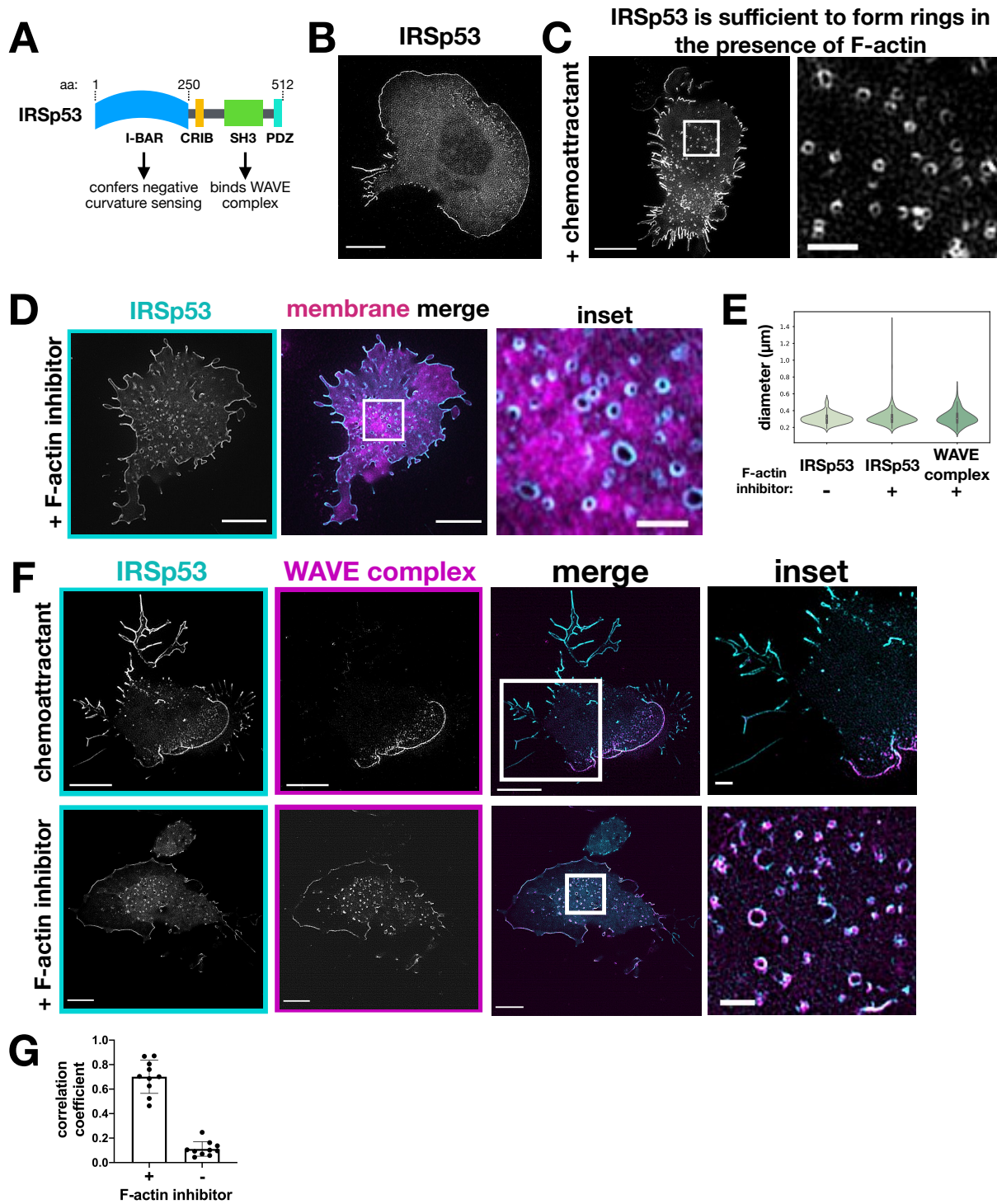


FIGURE 3.5. IRSp53 and the WAVE complex colocalize at lamellipodia and regions of saddle curvature but not at filopodia-like structures

(A) Domain structure of IRSp53. The I-BAR domain confers negative membrane curvature sensing and the SH3 domain enables binding to the WAVE complex.

(B) dHL60 cell expressing IRSp53-eGFP and stimulated with chemoattractant (10nM fMLP) show IRSp53 localization to both lamellipodia and filopodia-like structures. TIRF-SIM imaging, scale bar: 5 μ m.

(C) dHL60 cell with high expression of IRSp53-eGFP stimulated with chemoattractant (10nM fMLP) shows that IRSp53 is sufficient to form ring structures even in the presence of an intact actin cytoskeleton; see **S8 Video**. TIRF-SIM imaging, scale bars: 5 μ m (left) and 1 μ m (inset).

(D) dHL60 cell treated with F-actin inhibitor (500nM latrunculin B) shows IRSp53-eGFP (cyan) forms ring structures. Right, membrane merge (CellMask DeepRed; magenta). TIRF-SIM imaging, scale bars: 5 μ m (left) and 1 μ m (inset).

(E) Graph comparing the diameters of the WAVE complex rings with F-actin inhibition and IRSp53 rings with (+) or without (-) F-actin inhibition (500nM latrunculin B). Diameters measured in the same fashion shown in **Fig 2D**. Violin plot of rings; IRSp53 without F-actin inhibition n = 157 from 10 cells, IRSp53 with F-actin inhibition n = 483 from 10 cells, the WAVE complex n = 202 from 13 cells; cells pooled from at least 3 independent experiments per condition; Kruskal-Wallis test, nonsignificant P value > 0.05.

(F) IRSp53 and the WAVE complex colocalize at lamellipodia (top) and ring structures following actin depolymerization (bottom). IRSp53 also localizes to filopodia-like structures whereas the WAVE complex is excluded from those regions (top). Cells expressing both IRSp53-eGFP and Hem1-mCherry were treated with chemoattractant (10nM fMLP, top; see **S9 Video**) or F-actin inhibitor (500nM latrunculin B, bottom). TIRF-SIM imaging; scale bars: 5 μ m and 1 μ m (inset).

(G) Graph measuring colocalization between IRSp53-eGFP and Hem1-mCherry in conditions with or without F-actin inhibition. Barplot shows mean +/- standard deviation of Manders M1 correlation coefficient (fraction of IRSp53 in compartments containing Hem1); (+) F-actin inhibition, mean = 0.70 +/- 0.14, n = 10 cells, (-) F-actin inhibition, mean = 0.11 +/- 0.06, n = 10 cells; cells pooled from at least 3 independent experiments of TIRF-SIM imaging.

FIGURE 3.6

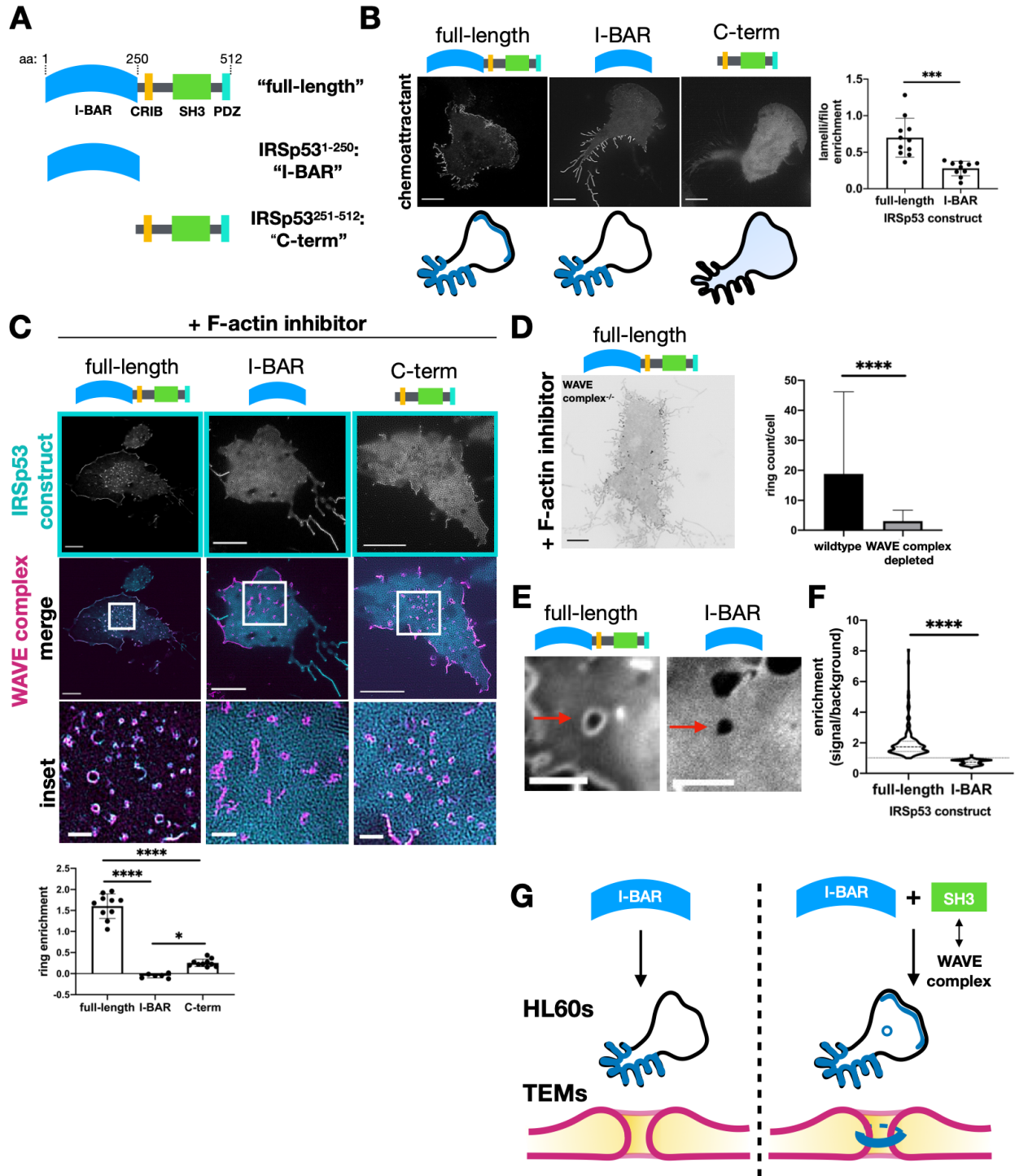


FIGURE 3.6. IRSp53 requires both its I-BAR domain and its interactions with the WAVE complex to localize to lamellipodia and regions of saddle curvature

(A) Schematic of IRSp53 structure-function constructs.

(B) Chemoattractant stimulated dHL60s expressing the eGFP-tagged IRSp53 constructs. Full-length IRSp53 enriches to lamellipodia and filopodia-like structures; I-BAR enriches to filopodia-like structures but not to lamellipodia; and C-term is cytosolic. Summary of the IRSp53 construct localization below. TIRF-SIM imaging; scale bar: 5 μ m. Right, graph of IRSp53 enrichment ratio of signal at lamellipodia per unit area vs signal at filopodia per unit area for full-length and I-BAR IRSp53 constructs. Graph shows mean \pm standard deviation; full-length mean = .70 \pm 0.27, n = 11 cells; I-BAR mean = 0.28 \pm 0.10, n = 10 cells; cells pooled from at least 3 independent experiments per condition; unpaired t-test two-tailed ***P value <0.001.

(C) F-actin inhibited dHL60s expressing IRSp53 and the WAVE complex. Middle row shows IRSp53-eGFP construct (cyan) overlay with Hem1-mCherry (magenta) rings. The I-BAR and C-term constructs fail to enrich robustly as ring structures. TIRF-SIM imaging; scale bars: 5 μ m and 1 μ m (inset). Graph comparing the signal enrichment of IRSp53 constructs' signal per unit area of rings (defined by Hem1-mCherry) over the background per unit area. Graph displays the mean \pm standard deviation where all rings within a cell were aggregated; full-length mean = 1.6 \pm 0.29, n = 10 cells from 3 independent experiments, I-BAR mean = -.05 \pm 0.05, n = 6 cells from 2 independent experiments, C-term mean = 0.25 \pm 0.09, n = 10 cells from 2 independent experiments; one-way ANOVA with two-tailed P value <0.0001 with Tukey's multiple comparisons follow-up tests, P values **** <0.0001, * <0.05.

(D) Full-length IRSp53 fails to enrich as ring structures in the absence of the WAVE complex. Inverted display of IRSp53-eGFP expressed in a WAVE complex depleted cell treated with latrunculin B (500nM). TIRF-SIM imaging; scale bar: 5 μ m. Graph comparing the mean \pm standard deviation number of rings per cell in wildtype and WAVE complex-null cells; wildtype mean = 18.8 \pm 27.4, n = 37 cells, WAVE complex-null mean = 3.09 \pm 3.65, n = 66 cells; cells pooled from the same 3 independent experiments; unpaired t-test two-tailed ****P value <0.0001.

(E) Images of HUVECs expressing full-length IRSp53 (left; see **S10 Video**) or I-BAR only domain (right; see **S11 Video**) at Y27632-induced TEMs. Scale bar: 5 μ m.

(F) Quantification of the enrichment of full-length IRSp53 and I-BAR domain at TEMs. Violin plot of enrichment, which was measured as described in **Fig 4C**. Each time point across TEM closure was considered as a single data point: full-length n = 186 and I-BAR n = 291, both from 4 TEMs from at least 3 independent experiments per condition; Mann-Whitney test of significance two-tailed ****P value <0.0001.

(G) Schematic summary of IRSp53 structure-function findings. Though IRSp53's I-BAR domain is sufficient to localize to filopodia-like structures, the I-BAR domain along with its

interactions with the WAVE complex are required for IRSp53 to enrich to lamellipodia, rings, and TEMs.

FIGURE 3.7

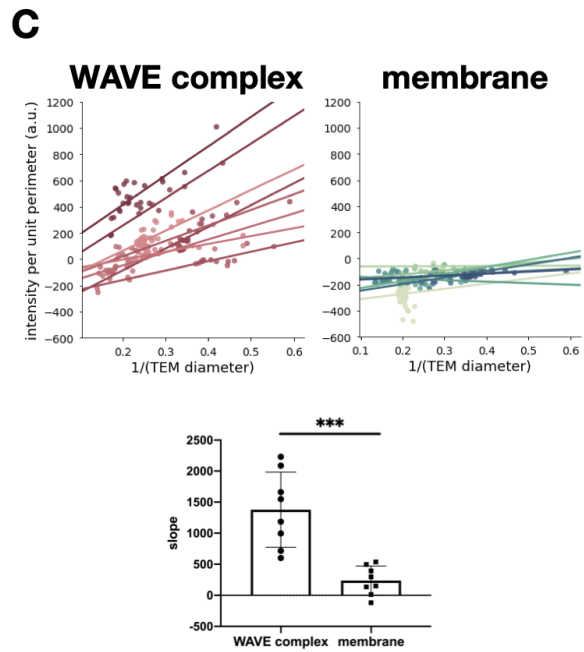
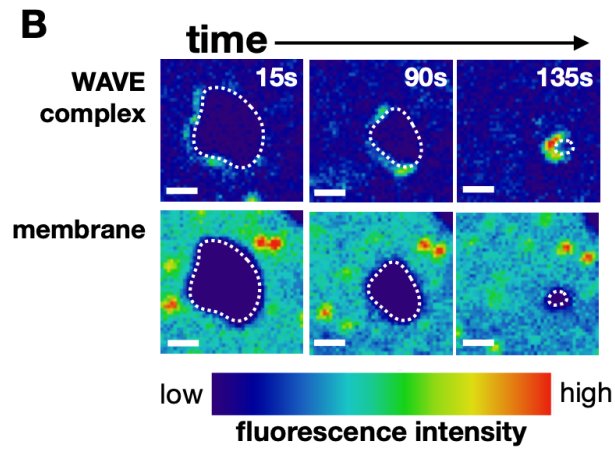
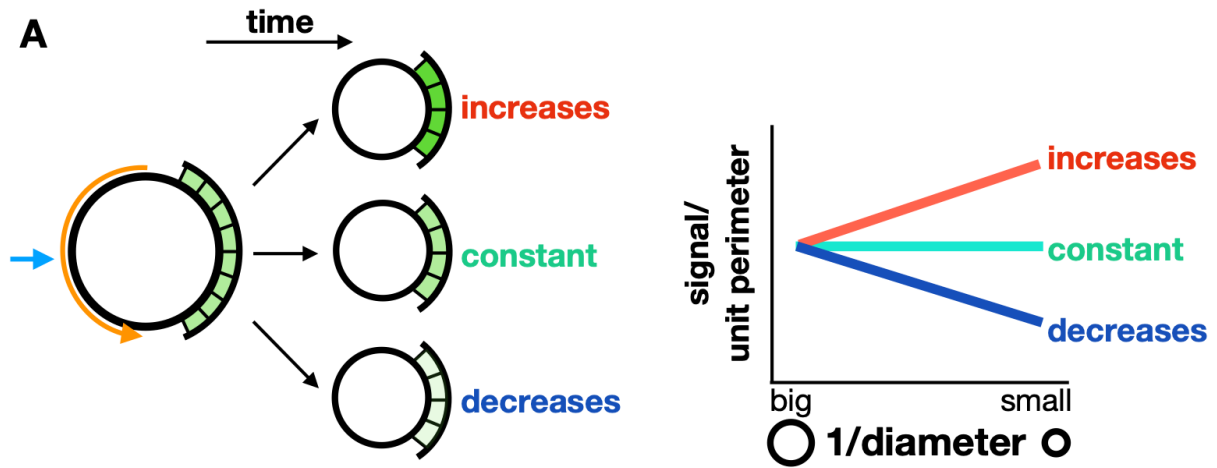


FIGURE 3.7. WAVE complex enriches to closing TEMs

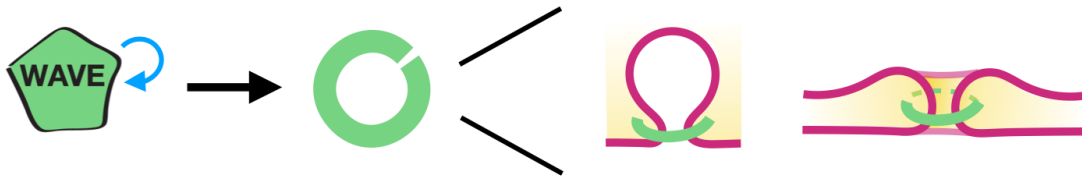
(A) Schematic of different molecular behaviors during TEM closure. As TEMs close, the local concentration (signal per unit length) could increase, remain constant, or decrease. A saddle geometry sensor would increase its local concentration until the TEM closure reaches the sensor's preferred radius of curvature.

(B) Time-lapse images of the WAVE complex (top) and the membrane (bottom) as a TEM closes. Images in each set have the same intensity scale in a LUT that eases the visualization of signal enrichment. The dotted line outlines the TEM membrane mask. Spinning disk confocal imaging; time in seconds; scale bar: 2 μ m. See **S12 Video**.

(C) Graph of the WAVE complex (top left) and membrane (top right) signal per unit perimeter as a TEM closes. Each line represents a linear regression for a single TEM over time. The WAVE complex shows higher enrichment at smaller (more positively curved) TEMs, suggesting a preference for membrane saddles with high positive curvature. Bottom: bar graph of mean \pm standard deviation of the slopes; the WAVE complex and membrane each had $n = 8$ TEMs from at least 3 independent experiments; unpaired t-test two-tailed ***P value <0.0002 .

FIGURE 3.8.

WAVE complex self-organizes as nanoscale rings at saddle geometries



Coupling of saddle curvature preference with F-actin polymerization could organize the growth of a lamellipodium and closure of TEMs

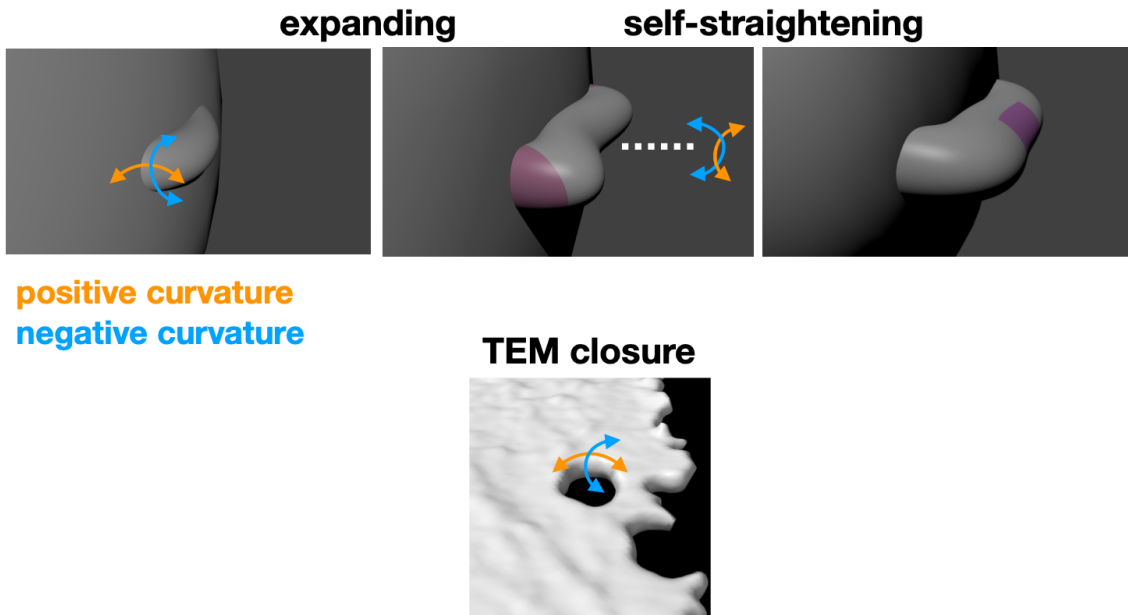


FIGURE 3.8. Summary and model

(A) The WAVE complex self-organizes as linear, oligomeric structures at saddle membrane geometries.

(B) The coupling of saddle curvature enrichment with F-actin polymerization could organize the growth of a lamellipodium and closure of TEMs. At the initiation of a lamellipodium, the lateral edges exhibit saddle curvature. WAVE complex association would lead to the growth of the extension (middle panel highlights extended membrane). Portions that “lag” behind also exhibit saddle curvature. WAVE complex association would result in self-straightening behavior (right panel highlights straightened membrane). Furthermore, WAVE complex association at the saddle geometry of TEMs would lead to TEM closure (bottom panel).

FIGURE S3.1

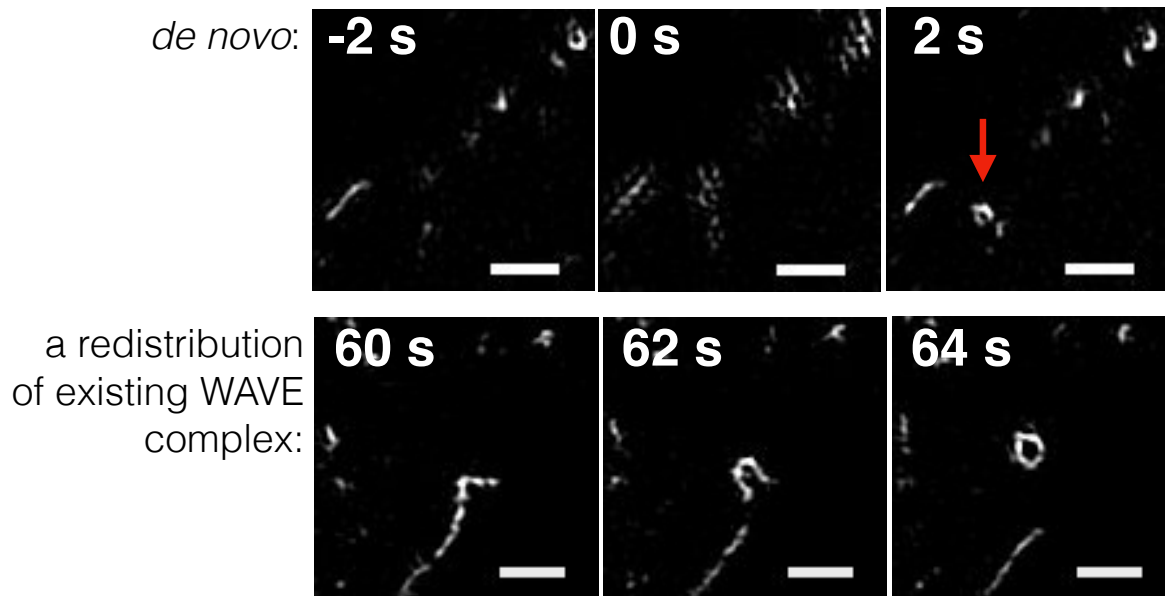


FIGURE S3.1. Different modes of the WAVE complex ring formation

WAVE complex (Hem1-eGFP) rings form either: *de novo* by the recruitment of new WAVE complex to the plasma membrane upon additional chemoattractant stimulation (100nM fMLP) in latrunculin B-treated cells (top) or a redistribution of existing membrane-bound WAVE complex that locally “collapses” into rings (bottom). Time T = 0 refers either to acute stimulation of either chemoattractant to latrunculin B-treated cells (top) or latrunculin B (bottom). Scale bar: 500nm.

FIGURE S3.2

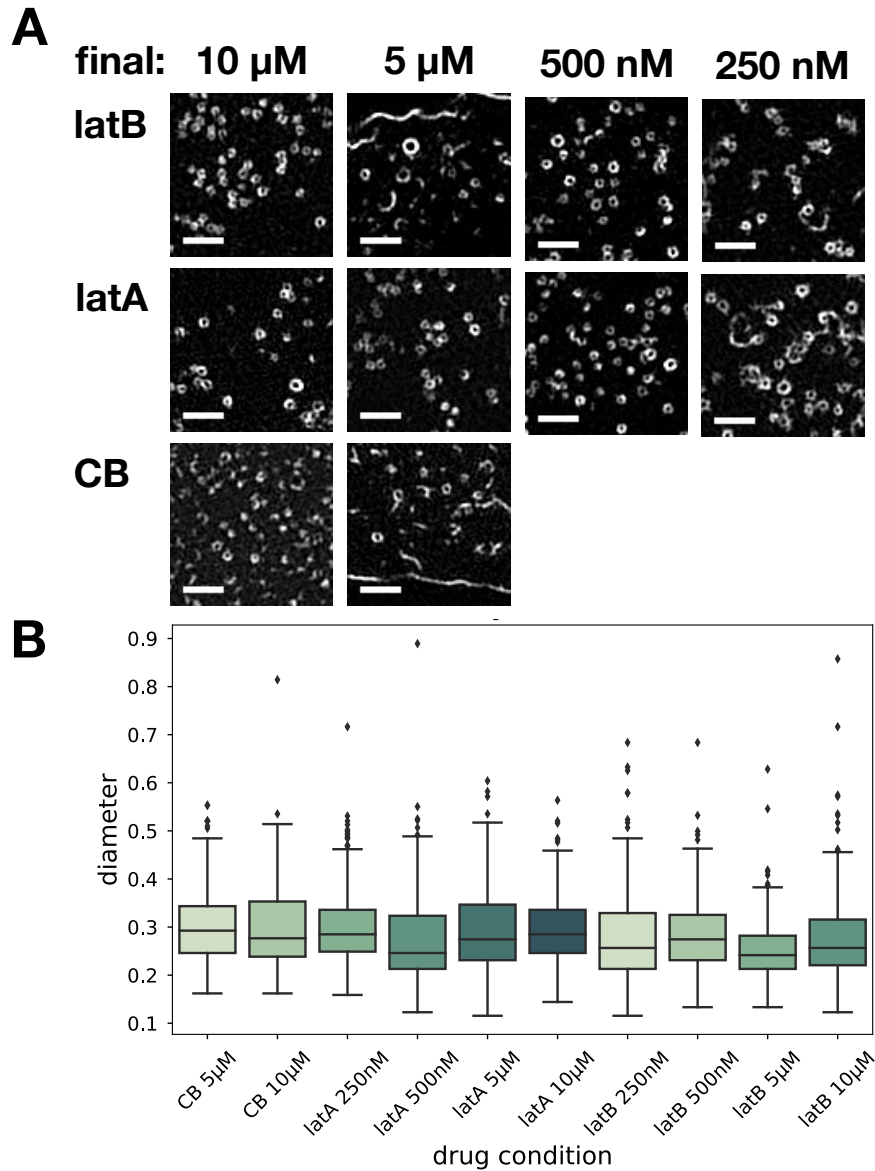


FIGURE S3.2. WAVE complex forms invariant ring structures across different F-actin inhibitors and concentrations

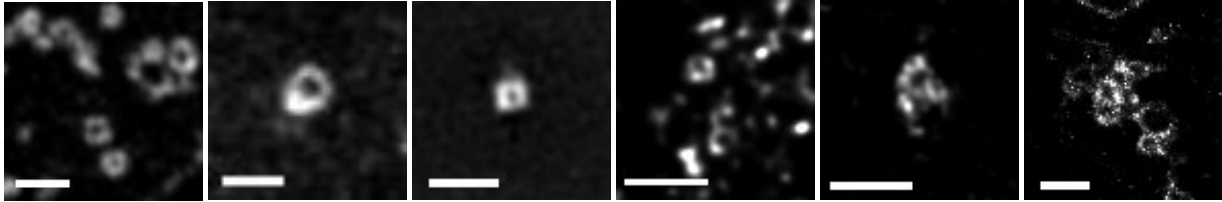
(A) Zoomed-in TIRF-SIM images of Hem1-eGFP rings across different drug conditions: 250nM, 500nM, 5 μM , 10 μM (final) of latrunculin B (latB), latrunculin A (latA), and cytochalasin B (CB). Scale bar: 1 μm .

(B) Boxplots (of interquartile range) of ring diameters across drug conditions as measured in **Fig 2D**. Each condition has at least 10 cells from at least 3 independent experiments per condition; ensemble histogram in **Fig 2D**.

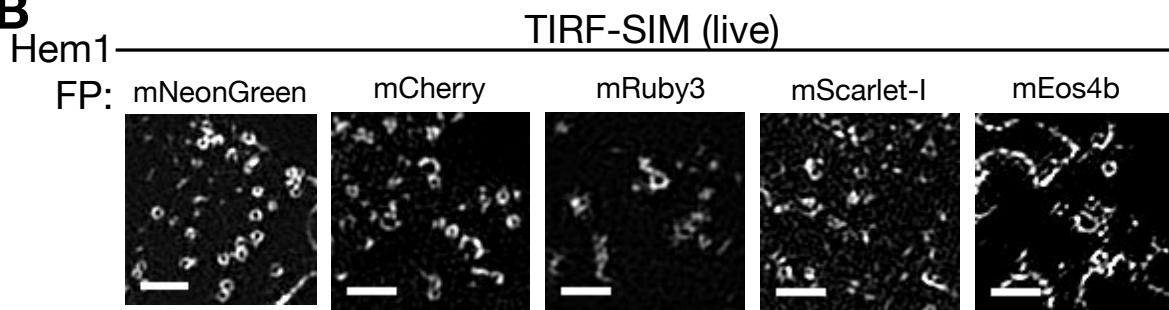
FIGURE S3.3

A

Airyscan 800 live eGFP Airyscan 880 fixed eGFP N-SIM fixed eGFP STED live mNG STED fixed mNG PALM fixed mEos4b



B



C

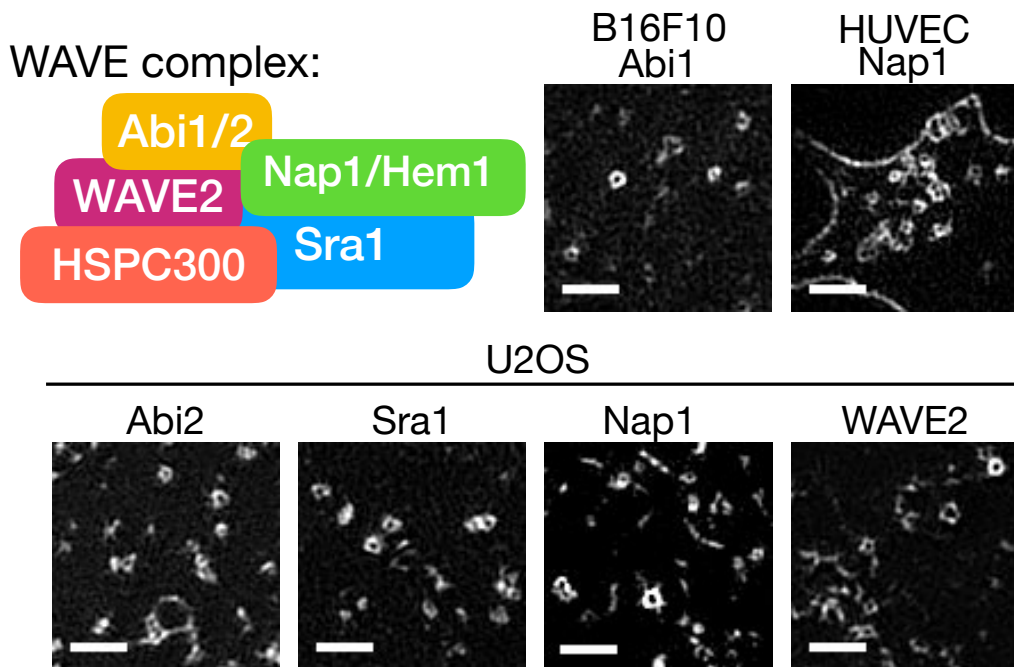


FIGURE S3.3. WAVE complex ring structures are observed independent of super-resolution modality, tagged fluorophore, cell type, and specific subunit

(A) Multiple super-resolution techniques in live or fixed cell conditions of Hem1 tagged with different fluorescent proteins all show ring structures. Microscopes and techniques used: Airyscan 800 (Zeiss), Airyscan 880 (Zeiss), Nikon-SIM (N-SIM), STimulated Emission Depletion (STED) on Leica SP8 with mNeonGreen [mNG], and photoactivated localization microscopy (PALM) on B Huang lab (UCSF) microscope. All cells treated with latrunculin B (500nM). Scale bar: 1 μ m.

(B) Hem1 tagged with different fluorescent proteins show ring structures. All imaged with TIRF-SIM and treated with latrunculin B (500nM). Scale bar: 1 μ m.

(C) Different WAVE complex subunits in other cell lines show ring structures. Top left, cartoon of the WAVE complex subunits. Different eGFP tagged WAVE complex subunits in B16F10 (*Mus musculus* skin melanoma cells), HUVECs (human umbilical vein endothelial cells), and U2OS (*Homo sapiens* bone osteosarcoma) cell lines. All cells treated with latrunculin B (500nM). Scale bar: 1 μ m.

FIGURE S3.4

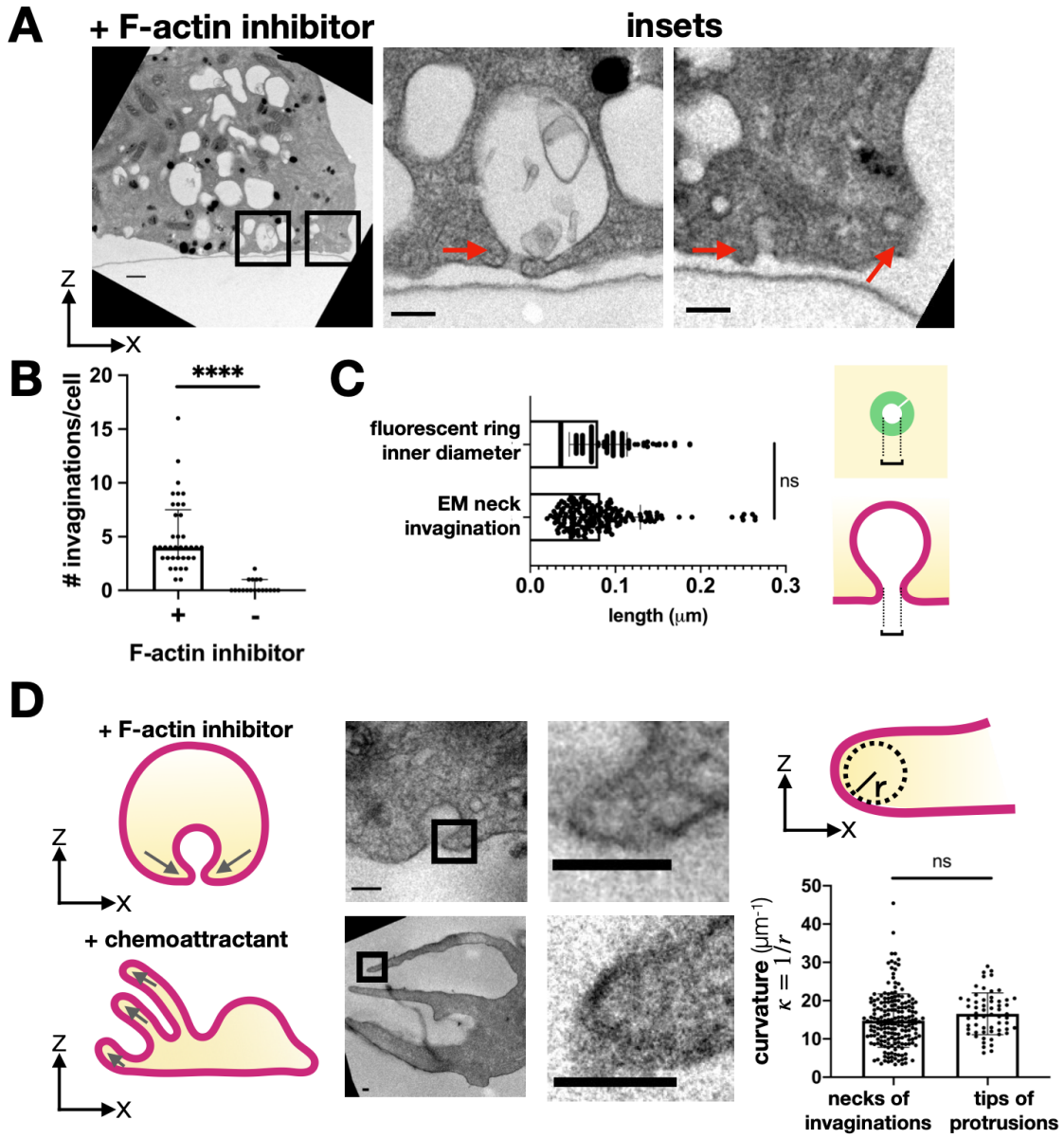


FIGURE S3.4. Membrane invaginations are observed by electron microscopy (EM)

(A) Transmission electron micrographs of a cross-section of dHL60s treated with latrunculin B (500nM). Center and right micrographs are insets (black boxes on left micrograph). Red arrows point to membrane invaginations. Scale bars: 500nm (left) and 200nm (inset).

(B) Graph comparing the number of membrane invaginations per serial section of cells treated with or without F-actin inhibitor (500nM latrunculin B). Graph shows median with interquartile range; (+) F-actin inhibitor n = 38 cells, (-) F-actin inhibitor n = 18 cells; Mann-Whitney test with two-tailed ****P value <0.0001.

(C) Graph comparing the length across the neck of invaginations by EM to the inner diameter of the fluorescent Hem1 rings of dHL60s treated with latrunculin B (500nM). Schematic represents where measurements were made. Graph shows median with interquartile range; EM of neck invaginations n = 190 (from 38 cells), fluorescent ring inner diameter n = 222 (from 4 cells); Mann-Whitney test with two-tailed P value ~0.3881. This finding supports the possibility that the WAVE complex enriches around the necks of membrane invaginations. Note that the invaginations have various sizes (**A**), yet the length across the neck is consistently ~71nm.

(D) Curvature comparison of the necks of invaginations and tips of protrusions. Electron micrographs of dHL60s treated with F-actin inhibitor (top; 500nM latrunculin B) and dHL60s treated with chemoattractant (bottom; 100nM fMLP) show that the curvature at the necks of invaginations and the tips of protrusions are similar. Graph shows mean +/- standard deviation; invagination mean = $14.68 \pm 6.97 \mu\text{m}^{-1}$, n = 190 (from 28 cells), protrusions mean = $16.56 \pm 5.44 \mu\text{m}^{-1}$, n = 59 (from 19 cells); unpaired t-test two-tailed ns P value > 0.05. Curvature, κ , defined as $1/r$ where r is the radius. Scale bar: 100nm.

FIGURE S3.5

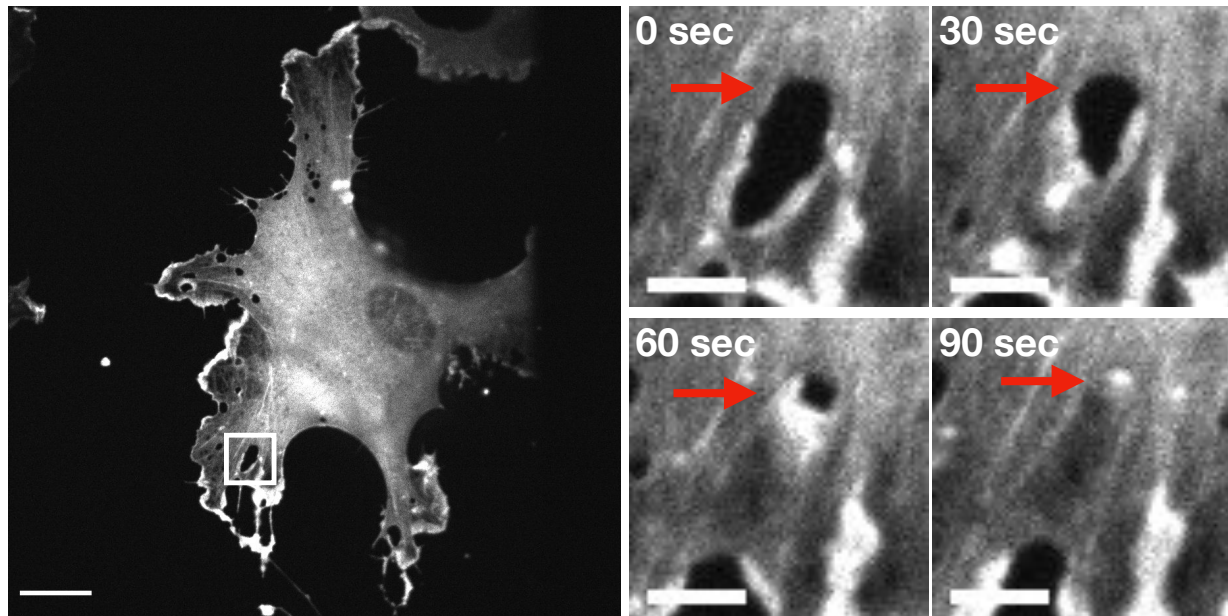


FIGURE S3.5. Actin localization at TEMs

HUVEC cell expressing actin-eGFP and treated with ROCK inhibitor Y27632 (50 μ M). Right insets: TEM closure over time; red arrows point to a TEM. Spinning disk confocal imaging; time in seconds; scale bars: 20 μ m (left) and 5 μ m (insets). See **S7 Video**.

FIGURE S3.6

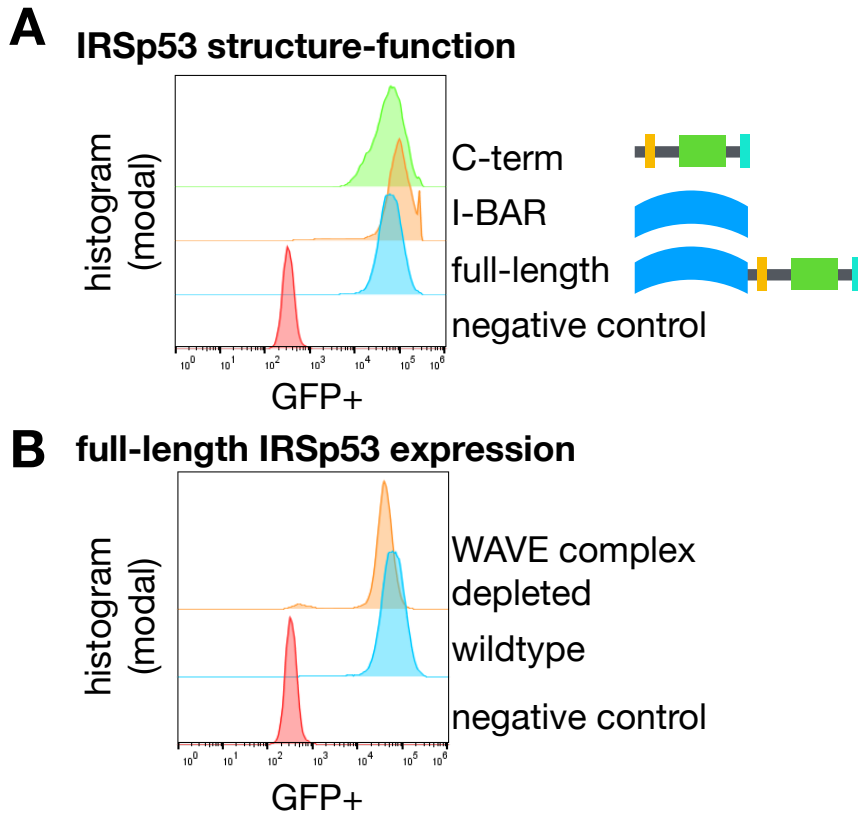


FIGURE S3.6. IRSp53 expression levels are comparable across conditions

(A) IRSp53 structure-function constructs have comparable expression levels in wildtype cells. Flow cytometry data graphed with FlowJo.

(B) Full-length IRSp53 has comparable expression levels in wildtype and WAVE complex-depleted HL60s. Flow cytometry data graphed with FlowJo.

CHAPTER FOUR

USING NANOTOPOGRAPHY TO ASSAY MOLECULAR CURVATURE SENSATION

“You have to fail in order to live;
otherwise you’re just doing the same thing over and over.”
- L Mahadevan

SUMMARY

How membrane geometry and signaling feed into one another remains a rich area of research. To probe this interaction, proper tools are essential. Here, I describe efforts toward using nanotopography to physically manipulate plasma membrane geometry to assay the role of curvature on intracellular signaling. Challenges remain to make this approach robust and high throughput, such as ensuring the cells are conforming to the structures, establishing proper controls, and managing the inherent challenges and tradeoffs with fabricating, visualizing and validating nanometer scale tools.

INTRODUCTION

In biology, shape and function are linked. For example, many physiological processes are coupled with active membrane shape changes: cells build broad, sheet-like protrusions to power motility and cells form inward buds that pinch off into the cell to regulate membrane proteins and import extracellular cargo. As cellular processes occur on the micrometer to nanometer scale, the tools used to probe physical cell properties, including membrane geometry, must be capable of making measurements and manipulations that span this range. Manipulating membranes with micro- and nanotopography has been shown to have a profound effect on stem cell differentiation, adhesion, and migration (1). For example, local asymmetries in micro/nanotopography have been shown to guide neutrophils to migrate unidirectionally (2).

Micro/nanotopography also functions as a tool to study the curvature sensitivity of molecules and curvature-sensitive processes. Recent work showed that by combining purified septins with lipid-coated beads, septins are maximally recruited to 1.0-3.0 μ m diameter beads (3). Using cells, other recent work showed that nanotopography-induced membrane curvature was sensed by clathrin-mediated endocytic proteins, which resulted in triggering and enhancing endocytosis (4). Micro/nanotopography presents an elegant way to test the role of curvature on proteins and biological processes.

Given that the WAVE complex associates with regions of curvature, in particular at edges of sheet-like lamellipodia and at sites of saddle curvature (Chapter 3), we sought to directly probe its curvature sensitivity via nanotopography.

RESULTS

To investigate the role of membrane curvature on the WAVE complex's enrichment, we aimed to image the WAVE complex in living cells that were conformed to nanopatterned substrates (**Figure 1**). If a cell is presented with a sine wave pattern, it would experience positive curvature at the crest and negative curvature at the trough of the sine wave. Saddle curvature describes geometries that exhibit positive curvature in one axis and negative curvature in the orthogonal axis. It is possible that molecular saddle sensors enrich to regions displaying either positive or negative curvature.

Nanotopography design

Since the WAVE complex associates with regions with $\sim 135\text{nm}$ radius of curvature in the positive axis (diameter of WAVE complex rings) and $\sim 65\text{nm}$ radius of curvature in the negative axis (thickness of lamellipodia), this requires nanopatterned substrates that span that range. Laser-cutting patterns is insufficient to produce these dimensions since lasers are diffraction limited. Thus, we collaborated with labs with expertise in focused ion beam nanofabrication (**Figure 2**). The first set of patterns were nano-ridges that spanned heights of 300 or 750nm, lengths of 1 mm, and thicknesses of 50, 100, 150, 200, 300, 500, or 1000nm spaced 2-3 μm apart. These patterns were etched into a silicon mold and stamped into a resin, which has a similar index of refraction of glass, and attached to coverglass. The second set of patterns were nano-Cs and nano-U's that were similar to those previously described (4,5). The nano-Cs and nano-U's were designed to have widths of 500nm, heights of 900nm, and inner diameters of 100, 200 or 500nm spaced 5 μm apart in a grid pattern. These patterns were etched into 0.2mm thick (i.e., $\sim\#2$ glass

for greater support). Given that these substrates were not #1.5 glass, this presented challenges with imaging objectives as well as compatibility with structured illumination super-resolution microscopy. Thus, the following experiments were performed with spinning disk confocal microscopy with correction collar corrected objectives.

Imaging the WAVE complex

Since the WAVE complex dynamics have not been fully reconstituted *in vitro* yet (6), I investigated whether membrane curvature biases the WAVE complex recruitment in living cells. We previously found that the WAVE complex forms nanometer-scaled ring structures that associate with saddle curvature in the absence of actin polymer (Chapter 3). Thus, I proposed to image cells on nanopatterns in an F-actin inhibited state in order to assay the effects of membrane morphology on the WAVE complex in an actin-independent manner.

We imaged the WAVE complex (via fluorescently-tagged hematopoietic protein 1 [Hem1], a subunit of the WAVE complex) in neutrophil-like HL60 cells. Though we found WAVE complex signal correlate with the nano-ridges, the z-resolution limit of confocal imaging made it difficult to distinguish where signal was enriched along the ridge (**Figure 3**). The curvature at the top of the ridge is positive whereas curvature along the bottom of the ridge is negative.

To assay curvature along the X-Y plane, we turned to the nano-Cs and nano-Us, which display negative curvature along the inner part of the letter and positive curvature along

the outer part of the letter. We were particularly interested in assaying negative curvature, which corresponds to localization at the edges of lamellipodia and along the inner part of the nano-C/U letter. When plating the cells onto these patterns, it was difficult to validate whether the membranes were adopting the negative curvature via fluorescence microscopy (**Figure 4**).

DISCUSSION

Though nanotopography is a powerful tool, it requires optimization, such as establishing robust controls, ensuring the cells are conforming to the structures, and balancing tradeoffs with visualizing and validating nanometer scale tools.

Control for negative curvature sensing

While there are published studies that use nanotopography to assay positive curvature sensing (4,7,8), to the best of our knowledge, that is not the case for negative curvature sensors. The canonical negative curvature sensors are the inverse Bin-amphiphysin-Rvs (I-BARs) domain containing proteins, which comprise of IRSp53, IRTKS, MIM, ABBA, and pinkbar (9,10). From elegant tether pulling experiments with giant unilamellar vesicles and purified proteins, IRSp53 has been characterized to have an intrinsic curvature of around 20nm in the negative axis and curvature sensing up to around 100nm (11). Though not all curvature sensors are the same, establishing a positive control for negative curvature sensing, such as IRSp53, for nanotopography with living cells will pave the way for assaying putative negative curvature sensors.

Forcing membrane adoption

It has been previously reported that cells do not conform and extend into the negative curvatures of nanopores and grooves (12). Furthermore, from electron micrographs of cells on various nanopatterned substrates, it is apparent that the membranes may not fully conform to the pattern. Thus, future work should focus on more robust technologies to zipper the membrane along the nanopatterns, either by manipulating the cell or with

surface chemistry. With any strategy, the method of forced adoption may introduce additional lengths and geometries that the cell may experience. If a “roof” is applied to compress cells, care must be taken to not crush the patterns. Furthermore, the compatibility of any method with reusing the nanopatterned substrate should be carefully considered.

Range of curvature and resolution limit

The nanometer scale poses not only challenges in fabrication, but also with visualization and validation. The nanofabrication challenge poses a potential supply issue as expertise and access to equipment may be limited. Furthermore, complex shapes, such as sine wave and saddles, may be nontrivial to fabricate. The visualization and validation challenges highlight limitations of current microscopy techniques. For example, various fluorescent super-resolution techniques require exactly #1.5 glass or require tradeoffs for high z-resolution and/or three-dimensional imaging whereas electron microscopy is limited to fixed cells and specific protein localization (i.e. APEX2) is not yet widespread.

The interdisciplinary nature of this experiment, which spans nano-engineering, cell biology, and high-resolution microscopy, highlights a combination of expertise that will undoubtedly unveil exciting insights.

MATERIALS AND METHODS

Nanotopography.

Two sets of nanopatterns were generated as described:

Nano-ridges were fabricated with the David Drubin lab at the University of California Berkeley and the Molecular Foundry at the Lawrence Berkeley National Laboratory. Briefly, nano-ridges were etched into a silicon wafer and used to stamp into OrmoComp resin (micro resist technology), which was then UV cured onto coverglass. For imaging, the patterned substrate was attached to a 35mm Attofluor Cell Chambers (ThermoFisher Scientific).

Nano-Cs and nano-U_s were designed and fabricated with the Wenting Zhao lab at Nanyang Technological University. The patterns were etched into silicon as previously described (5). To clean the patterns, cells were de-adhered with multiple rounds of trypsinization and washes. The substrate was incubated overnight with a dissolved tablet of Ultrazyme Enzymatic Cleaner (Advanced Medical Optics, Inc.) in contact lens solution. After drying, the substrate was plasma cleaned for 5min and exposed to UV for 15min.

Microscopy

Images were acquired on a Nikon Eclipse Ti microscope with a 60x/1.40NA Plan Apo or a 100x/1.49NA Apo TIRF objective (Nikon), Yokogawa CSU-X1 spinning disk confocal, and a Prime 95B CMOS camera (Photometrics). 405, 488, 561, 640nm laser lines (Agilent Technologies) and environmental control (37°C/5% CO₂; Okolab) was used. Software was controlled with Nikon Elements. To image the different substrates, the objective's

correction collar was calibrated prior to acquisition in order to adjust for the longer working distance. Z-stacks were acquired at steps for Nyquist sampling.

Cell culture

HL60 cells were cultured in RPMI-1640 with 25mM HEPES (Corning) with 10% (vol/vol) heat-inactivated fetal bovine serum (FBS; Gibco) and maintained at $0.2-1.0 \times 10^6$ cells/mL. Cells were differentiated with 1.5% DMSO (Sigma-Aldrich) in growth media for 4-5 days prior to experiments. All imaging presented was done with differentiated HL60s. Lentivirus was used to stably express the plasmid constructs of interest.

For imaging, differentiated cells were resuspended in imaging media (Leibovitz's L-15 [Gibco] with 0.5% FBS). Cells were either plated directly on patterns (incubated [$37^\circ\text{C}/5\% \text{CO}_2$] for at least 7 minutes before 2-3 washes with imaging media) or spun down onto the nanopatterns with a swinging bucket rotor centrifuge. If spun down, cells were first treated with latrunculin B (500 nM) in suspension. For chemoattractant stimulation, a 2x stock of 20nM fMLP (Sigma) was added. For additional chemoattractant stimulation, a 2x stock of 200nM fMLP was added. For F-actin inhibition, a 2x stock of $1\mu\text{M}$ latrunculin B (EMD Millipore and Sigma) with 200nM phorbol 12-myristate 13-acetate (PMA; Sigma; for persistent Hem1 activation) was used. All initial stocks were dissolved in 100% dry DMSO and freshly diluted in imaging media before experiments.

This project also used adherent cell types B16F10 and U2OS cells. Plasmids were transiently expressed with Lipofectamine 2000 or 3000 (Invitrogen) per manufacturer's

instructions. Positive control U2OS cells expressing dynamin and clathrin were a kind gift from the D Drubin lab (University of California Berkeley).

Membrane labeling

For membrane labeling, CellMask DeepRed (Invitrogen) was freshly diluted (0.5-1X) in imaging media. HL60s were labeled in suspension for 30sec at 37°C and washed 2-3 times with imaging media. Adherent cell lines were labeled for 5min at 37°C and washed 3-5 times with phosphate buffered saline (PBS).

Image analysis

All image analysis was performed in Fiji and/or Matlab. Images were background subtracted, sum projected, then processed with Matlab code that was modified from (4). Briefly, the individual structures were averaged, regions of interests were set (outer, inner, ends or edges/sides), and integrated intensities were measured and normalized.

ACKNOWLEDGEMENTS

I thank the Drubin lab: David Drubin, Jessica Marks, Charlotte Kaplan, and Bob Cail for their help and discussions over the years. I especially want to thank Bob for his help, which ranged from teaching me how to fabricate more patterns in the clean room to providing control cells. I also sincerely thank Wenting Zhao and Yongpeng Zeng for fabricating the nano-Cs and nano-Us and for answering my many questions. Their kindness and expertise have been instrumental. Thank you to the many people who have indulged me with numerous conversations concerning curvature sensation: members of the Weiner lab (especially Rachel Brunetti), Adam Frost, Nir Gov, Dimitri Stamou, Amy Gladfelter, and Patricia Bassereau. I also thank the Molecular Foundry at the Lawrence Berkeley National Laboratory for support.

REFERENCES

1. Lou HY, Zhao W, Zeng Y, Cui B. The Role of Membrane Curvature in Nanoscale Topography-Induced Intracellular Signaling. *Acc Chem Res.* 2018;51(5):1046–53.
2. Sun X, Driscoll MK, Guven C, Das S, Parent CA, Fourkas JT, et al. Asymmetric nanotopography biases cytoskeletal dynamics and promotes unidirectional cell guidance. *Proc Natl Acad Sci U S A.* 2015;112(41):12557–62.
3. Bridges AA, Jentzsch MS, Oakes PW, Occhipinti P, Gladfelter AS. Micron-scale plasma membrane curvature is recognized by the septin cytoskeleton. *J Cell Biol.* 2016;213(1):23–32.
4. Zhao W, Hanson L, Lou HY, Akamatsu M, Chowdary PD, Santoro F, et al. Nanoscale manipulation of membrane curvature for probing endocytosis in live cells. *Nat Nanotechnol.* 2017;12(8):750–6.
5. Li X, Matino L, Zhang W, Klausen L, McGuire AF, Lubrano C, et al. A nanostructure platform for live-cell manipulation of membrane curvature [Internet]. Vol. 14, *Nature Protocols.* Springer US; 2019. 1772–1802 p. Available from: <http://dx.doi.org/10.1038/s41596-019-0161-7>
6. Koronakis V, Hume PJ, Humphreys D, Liu T, Hørning O, Jensen ON, et al. WAVE regulatory complex activation by cooperating GTPases Arf and Rac1. *Proc Natl Acad Sci U S A.* 2011;108(35):14449–54.
7. Galic M, Jeong S, Tsai FC, Joubert LM, Wu YI, Hahn KM, et al. External push and internal pull forces recruit curvature-sensing N-BAR domain proteins to the plasma membrane. *Nat Cell Biol.* 2012;14(8):874–81.
8. Lou H-Y, Zhao W, Li X, Duan L, Powers A, Akamatsu M, et al. Membrane curvature

- underlies actin reorganization in response to nanoscale surface topography. *Proc Natl Acad Sci.* 2019;116(46):201910166.
9. Zhao H, Pykäläinen A, Lappalainen P. I-BAR domain proteins: Linking actin and plasma membrane dynamics. *Curr Opin Cell Biol.* 2011;23(1):14–21.
 10. Scita G, Confalonieri S, Lappalainen P, Suetsugu S. IRSp53: crossing the road of membrane and actin dynamics in the formation of membrane protrusions. *Trends Cell Biol.* 2008;18(2):52–60.
 11. Prévost C, Zhao H, Manzi J, Lemichez E, Lappalainen P, Callan-Jones A, et al. IRSp53 senses negative membrane curvature and phase separates along membrane tubules. *Nat Commun.* 2015;6.
 12. Santoro F, Zhao W, Joubert LM, Duan L, Schnitker J, Van De Burgt Y, et al. Revealing the Cell-Material Interface with Nanometer Resolution by Focused Ion Beam/Scanning Electron Microscopy. *ACS Nano.* 2017;11(8):8320–8.

FIGURE 4.1

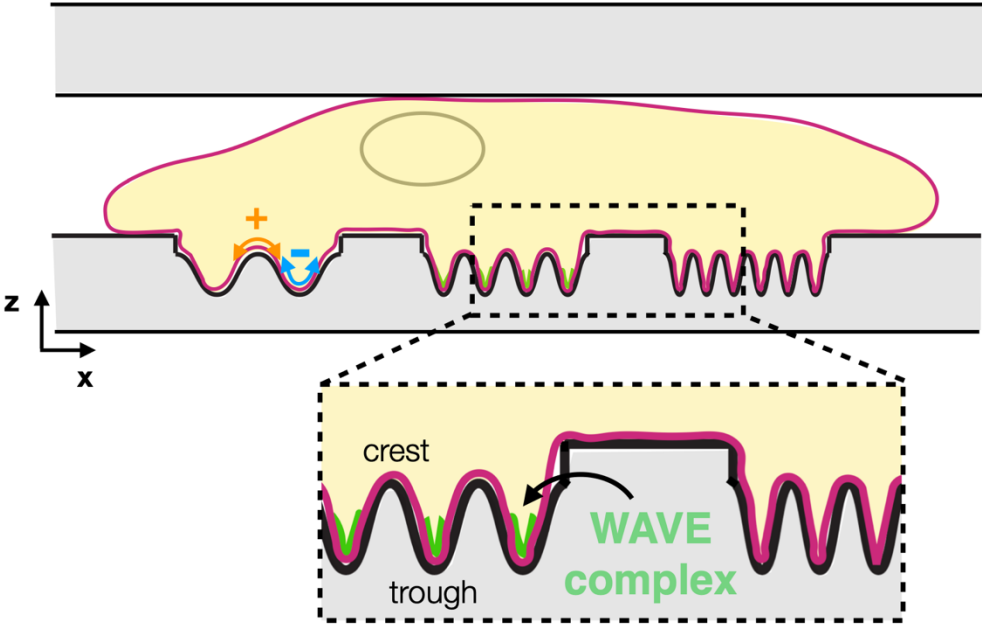


Figure 4.1. Using nanotopography to test WAVE complex curvature sensation

Schematic depicting the conceptual experimental setup. A cell is compressed in between two coverslips where one has a sine wave pattern, which displays positive curvature (orange arrow) at the crest and negative curvature (blue arrow) at the trough (top). If the WAVE complex associates with a specific range of negative curvature, it would enrich in the corresponding trough of a sine wave pattern (bottom).

FIGURE 4.2

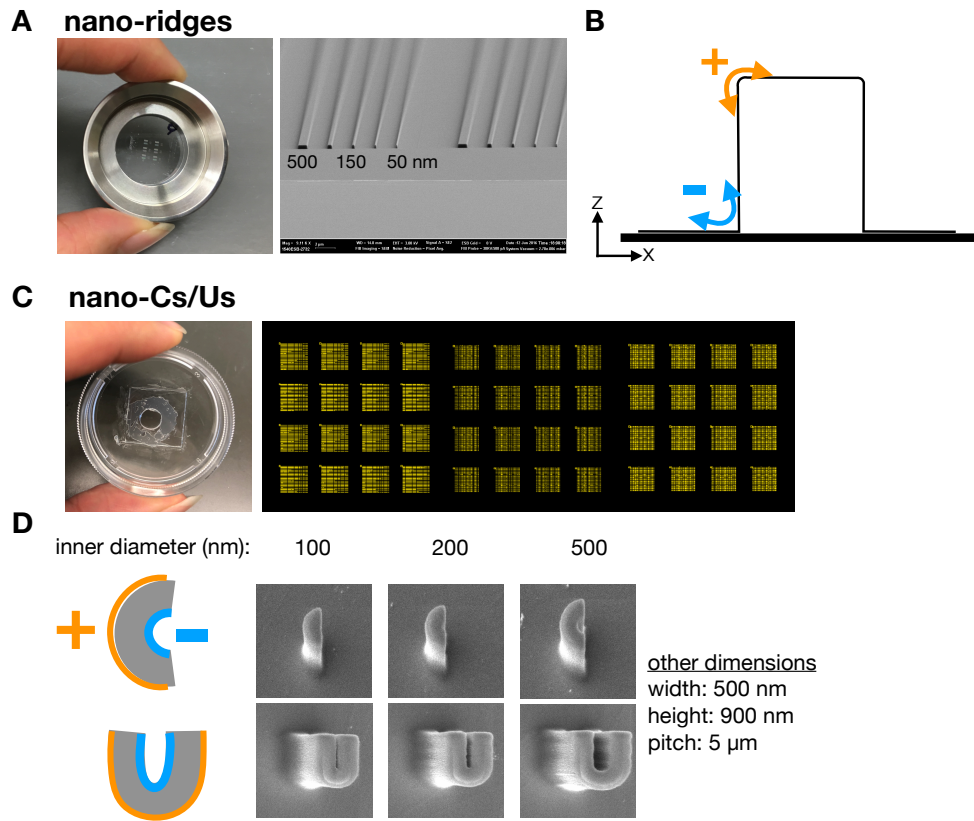


Figure 4.2. Nanopatterns design: nano-ridges and nano-Cs/Us

(A) Images of nano-ridges. Left: image of nanopatterned substrate in a 35mm chamber. Right: SEM micrograph of one set of nano-ridges (image from Drubin Lab). Some ridge thicknesses are indicated on the image.

(B) Schematic of positive and negative curvatures along nano-ridge. Note: curvature is in the axial, z-plane.

(C) Nano-Cs and nano-U design. Left: image of nanopatterned substrate attached to a 35mm well. Right: blueprint layout of patterns.

(D) Curvature and dimensions of nano-Cs and nano-U. Left: schematic of positive and negative curvatures of “C” and “U” letters. Note: the main curvature of interest is in the planar, X-Y plane. Right: SEM micrographs of nano-Cs and nano-U (images from Zhao Lab).

FIGURE 4.3

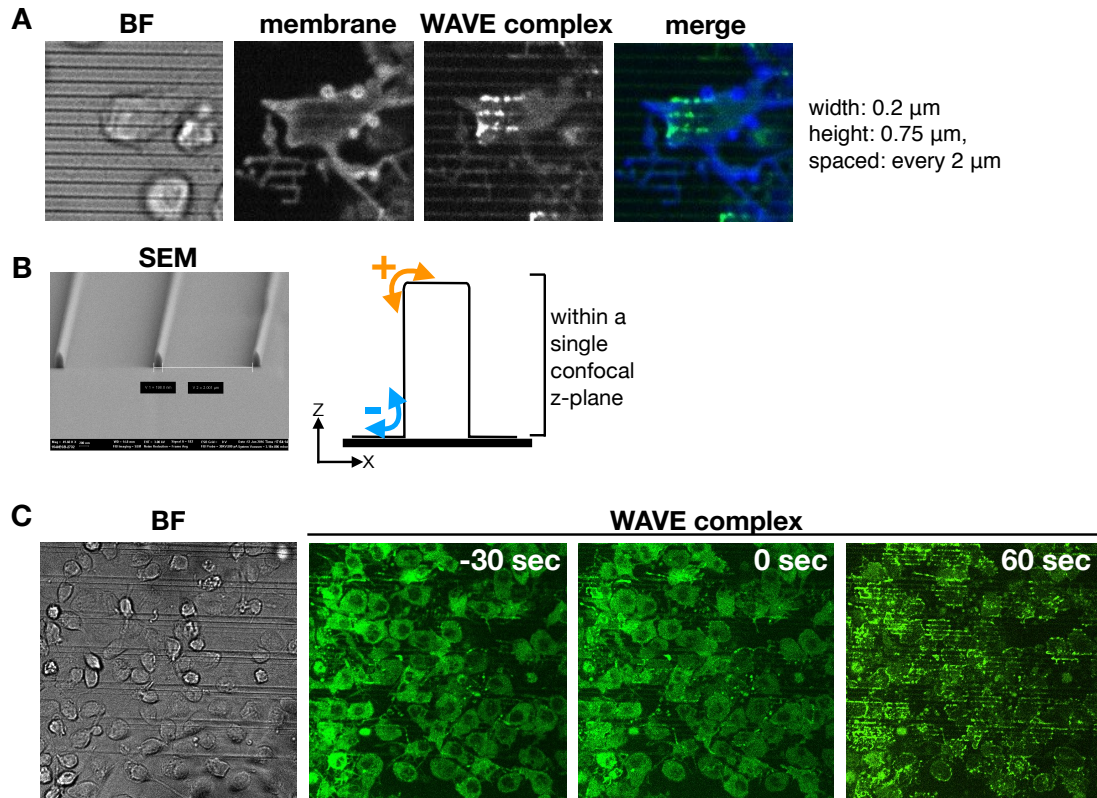


Figure 4.3. WAVE complex on nano-ridges

(A) Images of the WAVE complex along the nano-ridges. HL60 cells were treated with a F-actin inhibitor (500nM latrunculin B). Left to right: brightfield (BF), membrane marker (caax-tagBFP), WAVE complex (Hem1-eGFP) and the merged membrane-WAVE complex image.

(B) Views of the nano-ridges. Left: SEM micrograph (image from Drubin Lab) of the patterns in (A). Right: the cell would experience positive curvature at the top of the ridge and negative curvature at the bottom of the ridge. The ridge height exists within a confocal z-plane, which makes it difficult to localize where signal is enriched along the height of the ridge.

(C) Images of the WAVE complex recruiting to the nano-ridges. Cells that were treated with a F-actin inhibitor (500nM latrunculin B) were acutely stimulated with additional chemoattractant (100nM fMLP). Left to right: brightfield (BF), the WAVE complex at time = -30 sec before acute chemoattractant addition, time = 0 sec was when chemoattractant was acutely added, and time = 60 sec was post chemoattractant addition.

FIGURE 4.4

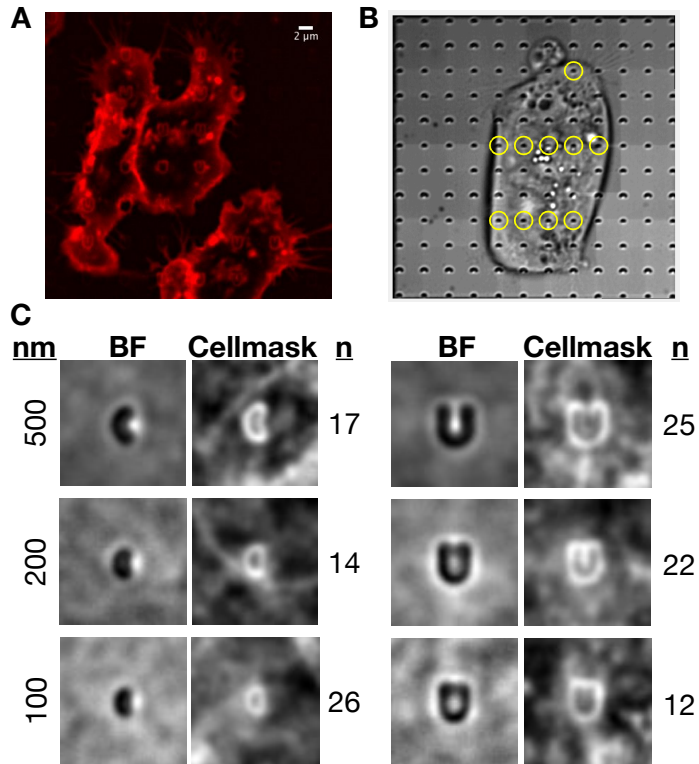


Figure 4.4 HL60s on nano-Cs and nano-U's

(A) Image of HL60s labeled with a membrane dye (CellMask DeepRed) on nanopatterns.

(B) Screenshot of the image analysis step of identifying nanopatterns in brightfield for averaging. Yellow circles highlight the detection of 100nm nano-Cs.

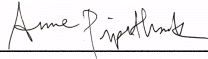
(C) Images of averaged brightfield (BF) and CellMask DeepRed labeling of HL60s on nanopatterns. The z-stack of each individual pattern was sum projected before the averaging. n lists the number of individual patterns that were averaged and nm is the size of the inner diameter of the nanopattern.

Publishing Agreement

It is the policy of the University to encourage the distribution of all theses, dissertations, and manuscripts. Copies of all UCSF theses, dissertations, and manuscripts will be routed to the library via the Graduate Division. The library will make all theses, dissertations, and manuscripts accessible to the public and will preserve these to the best of their abilities, in perpetuity.

Please sign the following statement:

I hereby grant permission to the Graduate Division of the University of California, San Francisco to release copies of my thesis, dissertation, or manuscript to the Campus Library to provide access and preservation, in whole or in part, in perpetuity.

DocuSigned by:

DEA3276016A24B8...

Author Signature

12/9/2019
Date